# Development of a soft sensor system for the property-controlled process design of freeform bending with moveable die

Von der Fakultät für Georessourcen und Materialtechnik der
Rheinisch-Westfälischen Technischen Hochschule Aachen

zur Erlangung des akademischen Grades einer

**Doktorin der Ingenieurwissenschaften**

genehmigte Dissertation

vorgelegt von

**Sophie Charlotte Stebner, M. Sc.**

**Berichtende:** **Univ.-Prof. Dr.-Ing. Sebastian Münstermann**
**Univ.-Prof. Dr.-Ing. Wolfram Volk**

Tag der mündlichen Prüfung: 24.09.2024

Diese Dissertation ist auf den Internetseiten der Universitätsbibliothek online verfügbar

# Vorwort

Diese vorgelegte Dissertation ist das Ergebnis meiner Forschungsarbeiten an der RWTH Aachen University im Rahmen des SPP-Projektes „Eigenschaftsgeregeltes Freiformbiegen“. Durch die interdisziplinäre Auslegung des Projektes habe ich in meinen letzten 4,5 Jahren viele Eindrücke sowohl in der Umformtechnik, der Regelungstechnik als auch natürlich in der Werkstofftechnik sammeln können, die allesamt Einfluss auf die Auslegung meiner Arbeiten geübt haben. Mit der nun vorliegenden Arbeit möchte ich mich nun bei den wichtigsten Menschen bedanken, die mir auf dem Weg bis zu diesem akademischen Meilenstein den Rücken gestärkt und teilweise unermüdliche Unterstützung gegeben haben.

Zunächst möchte ich meinem Doktorvater, Herrn Prof. Dr.-Ing. Sebastian Münstermann, danken. Neben der Betreuung meiner Arbeit und dem intensiven fachlichen Austausch macht mir die Arbeit mit Dir, Sebastian, einfach Freude – egal ob wissenschaftliches Arbeiten, strategische Entwicklungsarbeiten für die RWTH oder einfach nur eine kurze Plauderei zwischen Tür und Angel. Weiterhin bin ich meinem Zweitprüfer, Herrn Prof. Dr.-Ing. Wolfram Volk sehr dankbar für seine Zeit und den fachlichen Input zu dieser sowie allen anderen Arbeiten rund ums SPP. Zusätzlich gilt mein Dank meinen zahlreichen Arbeitskolleginnen und -kollegen. Besonders danke ich meinen Bürokollegen und meiner Bürokollegin in den letzten Jahren: Dr.-Ing. Yannik Sparrer, Dr.-Ing. David Lenz, Boyu Pan, Berk Tekkaya, Dongsong Li – Ihr macht den Institutsalltag am IBF immer bunt. Zudem möchte ich meinen ehemaligen und aktuellen Gruppenleitern Dr.-Ing. Michael Dölz und Manuel Henrich sowie meinen Projektpartnern Dr.-Ing. Daniel Maier und Ahmed Ismail für die fachlichen Diskussionen danken.

Meine Familie hat mich während meiner gesamten akademischen Laufbahn immer bedingungslos unterstützt. Besonders meiner Mutter, Dr.-Ing. Birgitta Jüde, und meinem Vater, Dr.-Ing. Guido Stebner, bin ich für die Unterstützung und den Zuspruch sehr dankbar – insbesondere da ich durch Euch erst zur Werkstofftechnik gefunden habe. Mama, wer hätte gedacht, dass Dich die Weiss’schen Bezirke so lange begleiten werden!

Außerdem danke ich meiner liebsten Schwester, Marie, die bei allen Anliegen immer ein offenes Ohr für mich hat und mir mit meiner Mutter zusammen eins der größten weiblichen Vorbilder ist. Deine und Mamas Stärke sowie eure Empathie faszinieren mich jeden Tag.

Zu guter Letzt danke ich Benedikt, meinem Fels in der Brandung. Du sprichst mir immer wieder Mut zu, wenn ich mal den Kopf hängen lasse und dein unermüdlicher Glaube an mich inspiriert mich dazu, alle Herausforderungen anzunehmen und zu meistern.

*Sophie Charlotte Stebner* *April 2024*

# Abstract

The freeform bending process with movable die is an innovative bending process that allows the manufacture of complex three-dimensional geometries without a change in the bending tool. Thus, it offers a high degree of design freedom and customization. The initial situation of this scientific work was the ability of bending complex geometries, however without any knowledge on relevant mechanical properties, that were set in the bent component. This led to high amounts of scrap material, time consuming adjustment procedures during the process as well as unknown reliability regarding the component's performance. Hence, there is a need to implement a closed-loop property-control into the freeform bending process, that can adjust the degrees of freedom on offer during the bending procedure according to the needed mechanical properties of the tube.

Mechanical properties that are especially of interest for bent round tubes are the strength, ductility as well as the residual stresses in axial and hoop direction, as they predominantly determine the components application. However, these mechanical properties are time-consuming or even impossible to determine during the bending process, where it is necessary to know them, in order to be able to manipulate the actuators according to the needed properties. Hence, there needs to be a fast, reliable and efficient solution for the derivation of the strength, ductility and residual stresses in the tubes.

Thus, the focus of this work lies on the conception of a so-called soft sensor based on state-space models that can quickly derive the relevant mechanical properties during the bending process. The soft sensor relies on Ultrasonic Contact Impedance hardness and Barkhausen Noise measurements that are susceptible to a change in macroscopical/microscopical properties in the investigated material and can, furthermore, be implemented into the bending machine. Strength, ductility, hoop, and residual axial stress measurements are taken partly experimentally as well as numerically and are correlated to the Ultrasonic Contact Impedance hardness and Barkhausen Noise respectively such that a fast and reliable derivation of the relevant mechanical properties is enabled.

Hence, this work lies the foundation for a closed-loop property-control of the bending process in introducing a methodology for the quick and reliable determination of immeasurable parameters in a component allowing a more resource and economically efficient design of the process.

# Kurzzusammenfassung

Der Freiformbiegeprozess mit bewegter Matrize ist ein innovativer Biegeprozess, der die Herstellung komplexer dreidimensionaler Geometrien ohne Wechsel des Biegewerkzeugs ermöglicht und somit ein hohes Maß an Gestaltungsfreiheit und Anpassung bietet. Die Ausgangssituation dieser wissenschaftlichen Arbeit war die Fähigkeit, komplexe Geometrien zu biegen, jedoch ohne Kenntnisse über relevante mechanische Eigenschaften, die im gebogenen Bauteil vorliegen. Dies jedoch führt zu einer hohen Anzahl an zu verschrottenden Rohrbögen, zeitaufwändigen Einstellverfahren während des Prozesses sowie unbekannter Leistungsfähigkeit der Bauteile. Daher besteht die Notwendigkeit, eine eigenschaftsbasierte Regelung in den Freiformbiegeprozess zu implementieren, die die Freiheitsgrade des Prozesses während des Biegens entsprechend den benötigten mechanischen Eigenschaften des Rohrs anpassen kann.

Mechanische Eigenschaften, die besonders interessant im gebogenen Rundrohr sind, sind die Festigkeit, Duktilität sowie die Eigenspannungen in Axial- und Umfangsrichtung, da sie überwiegend die Anwendung und Verarbeitbarkeit des Bauteils bestimmen. Diese mechanischen Eigenschaften sind jedoch zeitaufwändig oder sogar unmöglich während des Biegeprozesses zu bestimmen, wo es jedoch notwendig ist, sie zu kennen, um die Aktuatoren entsprechend der benötigten Eigenschaften einstellen zu können. Daher muss eine schnelle, zuverlässige und effiziente Lösung für die Ableitung der Festigkeit, Duktilität und Eigenspannungen in den Rohren wissenschaftlich erschlossen werden.

Folglich liegt der Schwerpunkt dieser Arbeit auf der Konzeption eines sogenannten Softsensors, basierend auf Zustandsraummodellen, der während des Biegeprozesses schnell die relevanten mechanischen Eigenschaften ableiten kann. Der Softsensor stützt sich dabei auf Ultrasonic Contact Impedance Härte- und Barkhausen-Rauschmessungen, die sensitiv auf Veränderungen in makroskopischen/mikroskopischen Eigenschaften im untersuchten Material reagieren und dabei in die Biegemaschine integriert werden können. Festigkeits-, Duktilitäts-, Umfangs- und Axialeigenspannungsmessungen werden teilweise experimentell sowie numerisch durchgeführt und jeweils mit der Ultrasonic Contact Impedance Härte und dem Barkhausen-Rauschen korreliert, so dass eine schnelle und zuverlässige Ableitung dieser relevanten mechanischen Eigenschaften ermöglicht wird.

Somit schafft diese Arbeit die Basis für eine eigenschaftsbasierte Regelung des Biegeprozesses und führt eine Methodik für die schnelle und zuverlässige Bestimmung nicht messbarer Parameter in einem Bauteil ein, was eine ressourcen- und kosteneffizientere Gestaltung des Prozesses ermöglicht.

# Inhaltsverzeichnis

# List of Figures

# List of Tables

# List of Abbreviations

| Abbreviation | Meaning |
|---|---|
| 3MA-II | Barkhausen noise sensor designed by Fraunhofer |
| bcc | Body centered cubic |
| BHN | Barkhausen noise |
| CAE | Computer aided engineering |
| DIN (EN) | Deutsches Institut für Normung (Europäische Norm) |
| DOF | Degree of Freedom |
| ECT | Eddy current testing |
| EKF | Extended Kalman Filter |
| fcc | Face centered cubic |
| FE, FEA, FEM | Finite Element, Finite Element Analysis, Finite Element Method |
| FFT | Fast Fourier Transformation |
| HAZ | Heat affected zone |
| HV | Vickers hardness |
| J2 | Von Mises plasticity theory |
| NARMAX | Nonlinear autoregressive moving average model with exogenous inputs |
| PEEQ | Equivalent plastic strain |
| RDB | Rotary Draw Bending |
| SD | Standard deviation |
| SF | Symmetry Factor |
| UCI | Ultrasonic Contact Impedance |
| VDI | Verein deutscher Ingenieure |
| XRD | X-Ray Diffraction |

# List of Symbols

**Chapter 2**

| Symbol | Unit | Meaning |
|---|---|---|
| $\sigma$ | MPa | Engineering stress |
| $F$ | N | Force |
| $A$ | $mm^2$ | Cross-section |
| $Ac_1$ | °C | Austenitization temperature |
| $\varepsilon$ | % | Engineering strain |
| $\Delta L$ | mm | Change in length related to initial length |
| $L_0$ | mm | Initial length |
| $E$ | GPa | Young's Modulus |
| $\sigma_T$ | MPa | True Stress |
| $\varepsilon_T, \varphi,$ | - | True Strain, degree of deformation |
| $\bar{\varepsilon}_p, \bar{\varepsilon}_p^n$ | - | Equivalent plastic strain |
| $\dot{\varepsilon}$ | 1/s | Strain rate |
| $\sigma_{ij}$ | MPa | Normal stresses; indexes referring to direction of surface normal and direction of stress component |
| $\tau_{ij}$ | MPa | Shear stresses; indexes referring to direction of surface normal and direction of stress component |
| $\delta_{ij}$ | - | Kronecker delta; indexes referring to direction of surface normal and direction of stress component |
| $\bar{\bar{\sigma}}$ | MPa | Stress tensor |
| $p$ | MPa | Hydrostatic stress tensor |
| $I$ | - | Unit tensor |

| | | |
|---|---|---|
| $s$ | MPa | Deviatoric stress tensor |
| $I_1 - I_3$ | - | Invariants of stress tensor |
| $J_1 - J_3$ | - | Invariants of deviatoric stress tensor |
| $\bar{\sigma}_e, \sigma_{e,M}, \sigma_{e,T}$ | MPa | Critical stress value, according to von Mises, according to Tresca |
| $\bar{\sigma}(\bar{\varepsilon}_p), \bar{\sigma}_{Alpha}(\bar{\varepsilon}_p)$ | MPa | Flow stress |
| $\alpha$ | - | Weighting parameter |
| $b, k_0$ | MPa | Yield strengths in Ludwik-Voce model |
| $A, Q, \beta$ | - | Fitting parameters |
| $n$ | - | Hardening exponent |
| $\sigma_1 - \sigma_3$ | MPa | Residual stresses type I – III |
| $\sigma_{Hoop}$ | MPa | Residual hoop stresses |
| $M$ | A/m | Magnetization |
| $M_s, M_R$ | A/m | Saturation magnetization, residual magnetization |
| $H$ | A/m | Magnetic field strength |
| $H_e$ | A/m | Internal magnetic field |
| $H_c$ | A/m | Coercive field strength |
| $\chi$ | - | Magnetic susceptibility |
| $C$ | - | Constant in curie law |
| $T$ | °C | Temperature |

| | | |
|---|---|---|
| $T_c$ | °C | Curie temperature |
| $\lambda$ | - | Temperature-dependent material constant |
| $t$ | s | Time |
| $A$ | - | State transition matrix describing the system's internal dynamics |
| $x_{k+1}$ | Dependent on system | State vector ahead at time $k+1$. |
| $x_k$ | Dependent on system | State vector representing the system's internal states at time $k$ |
| $B$ | - | Input matrix relating the inputs to the state variables |
| $u_k$ | Dependent on system | Input vector representing external inputs influencing the system |
| $y_k$ | Dependent on system | Output vectors, representing the system's observed outputs at time $k$ |
| $C$ | - | Output matrix relating the states to the outputs |
| $D$ | - | Matrix relating the inputs directly to the outputs |
| **Chapter 5** | | |
| $s$ | mm | thickness of the tube |
| $D_0$ | mm | outer diameter before splitting |
| $D_f$ | mm | diameter after splitting |
| $\vartheta$ | - | Poisson's ratio |
| **Chapter 6** | | |
| $\hat{x}_k^-, \hat{x}_k^+$ | Dependent on system | State estimates |
| $F, H$ | - | Jacobian matrices for linearization of system |
| $P, Q, R$ | Dependent on system | Error covariance matrices |

| | | |
|---|---|---|
| $\tilde{y}_k$ | Dependent on system | Measurement residual |
| $z_k$ | Dependent on system | Measurement |
| $K_k$ | - | Kalman gain |
| $h$ | Dependent on system | Measurement matrix |
| $g$ | Dependent on system | State matrix |
| $R^2$ | - | Coefficient of determination |
| **Chapter 7** | | |
| $n$ | - | Natural number of the diffraction order of the interference |
| $\lambda$ | m | Wavelength of the radiation |
| $d^{\{hkl\}}$ | m | Lattice plane spacing |
| $\theta^{\{hkl\}}$ | rad | Bragg angle |
| $S_1, S_2$ | - | Axes in the plane of the sample, $S_1$ is determined by the tester |
| $S_3$ | - | Axes perpendicular to the surface of the sample |
| $L_1 - L_3$ | - | Laboratory coordinate system where $L_3$ is the normal of the diffracting lattice plane $\{hkl\}$ and the angle bisector between the incoming and diffracted x-ray |
| $\varphi$ | ° | Angle between a fixed direction in the specimen's surface and the projection of the normal of the diffraction planes |
| $\Psi$ | ° | Angle between the normal of the sample surface and the normal of the diffraction planes |
| $S\phi$ | - | Direction within which the stresses $\sigma_\varphi$ and $\tau_\varphi$ are measured |
| $\varepsilon_{\varphi\Psi}^{\{hkl\}}$ | - | Strains in the direction defined by the angles $\varphi$ $and$ $\Psi$ for the lattice plane $\{hkl\}$ |

| | | |
|---|---|---|
| $S_1^{\{hkl\}}$ and $\frac{1}{2}S_2^{\{hkl\}}$ | MPa | Elasticity constants for the lattice plane $\{hkl\}$ |
| $\sigma_{11}, \sigma_{22}$ | MPa | Normal stresses in $S_1$ and $S_2$ directions |
| $\tau_{12}$, $\tau_{13}$, $\tau_{23}$ | MPa | Shear stresses in the planes determined by $S_1$, $S_2$ and $S_3$ |
| $U_{ind}$ | V | Induced voltage of the signal |
| $n$ | - | Number of coil turns |
| $S$ | $m^2$ | Area of the sample cross-section |
| $B$ | T | Magnetic flux density of the excitation field |
| $\mu$ | H/m | Permeability of the material |
| $\varepsilon$ | F/m | Electrical permittivity |
| $\sigma$ | S/m | Electrical conductivity |
| $z$ | m | Position where $B$ was measured |
| $\omega$ | rad/s | Wave frequency |
| $\delta$ | m | Penetration depth |
| $w_{k-1}$ | Dependent upon state | Process noise |
| $f$ | - | State transition function |
| $h$ | - | Observation function |
| $v_k$ | Dependent upon state | Observation noise |
| $\theta$ | - | Optimal coefficients vector |
| $F$ | - | Polynomial features |

*List is ordered regarding occurrence in text.

# List of Publications

Some of the results in this dissertation have been published in scientific journals and conference proceedings under my authorship. Chapter 6 is published in its entirety under DOI: 10.3390/ma14164549 (number II below). All publications are listed below:

I. D. Maier, S. Stebner, A. Ismail, M. Dölz, B. Lohmann, S. Münstermann, W. Volk, The influence of freeform bending process parameters on residual stresses for steel tubes, Advances in Industrial and Manufacturing Engineering 2, 100047 (2021); doi: 10.1016/j.aime.2021.100047.

II. S. C. Stebner, D. Maier, A. Ismail, S. Balyan, M. Dölz, B. Lohmann, W. Volk, S. Münstermann, A System Identification and Implementation of a Soft Sensor for Freeform Bending, Materials (Basel, Switzerland) 14 (2021); doi: 10.3390/ma14164549.

III. S. C. Stebner, D. Maier, A. Ismail, M. Dölz, B. Lohman, W. Volk, S. Münstermann, Extension of a Simulation Model of the Freeform Bending Process as Part of a Soft Sensor for a Property Control, Key Engineering Materials 926, 2137–2145 (2022); doi: 10.4028/p-d17700.

IV. S. C. Stebner, D. Maier, A. Ismail, M. Dölz, B. Lohman, W. Volk, S. Münstermann, Sensitivity Analysis of Barkhausen Noise Measurements for Residual Stress Correlation. In: SMSI 2023, 199–200.

V. S. C. Stebner, J. Martschin, B. Arian, S. Dietrich, M. Feistle, S. Hütter, R. Lafarge, R. Laue, X. Li, C. Schulte, D. Spies, F. Thein, F. Wendler, M. Wrobel, J. R. Vasquez, M. Dölz, S. Münstermann, Monitoring the evolution of dimensional accuracy and product properties in property-controlled forming processes, Advances in Industrial and Manufacturing Engineering 8, 100133 (2024); doi: 10.1016/j.aime.2023.100133.

# 1 Problem Definition and Objectives

The manufacturing of reliable, high-performing metallic components is of central importance in various industries. The production of such components more often than not involves metal forming, enabling the setting of the necessary product properties, such as shape and mechanical properties, of the component. While nearly all forming processes incorporate closed-loop control for the manufacturing process, the control of mechanical properties, specifically due to a process-microstructure-property evolution with entailing feedback on the process settings, remains predominantly open-loop during the forming process [1]. However, this presents several drawbacks. If forming processes do not regard the microstructure evolution of the material inevitably occurring during the process and thus entailing fluctuations in the component, extensive post-production of the component may become necessary or the component is scrapped entirely [2,3]. The design of closed-loop property-controls would, thus, enhance and optimize the processes regarding resource efficiency, energy efficiency as well as economic efficiency.

However, this pursuit raises several questions. Initially, it must be established what mechanical properties are of interest, hence which sensors and actuators in the process may be used to monitor and influence these characteristics. Furthermore, where can the sensors and actuators be positioned in the machine, so that the relevant microstructure evolution can be measured and optimally influenced. Oftentimes, actuators have a highly non-linear impact on the product properties of the component, making model definition difficult [3,4]. When it comes to sensor/measurement technique placement, measuring target values directly at the points of interest can be challenging, maybe even impossible. Which means that a spatial and time-dependent analysis of the product properties of interest must be conducted and implemented via mathematical models to get full information on all information needed regarding the relevant product properties [3]. Additionally, the sensors employed cannot be of destructive nature, as the components are to be employed after the processes.

To address these obstacles, a crucial initial step involves establishing a comprehensive understanding of how the mechanical properties and the geometry of the workpiece interact and are influenced by different degrees of freedom (DOF) during the process. Usually for forming processes, the bending of a set geometry automatically leads to a defined set of mechanical properties (without taking uncertainties and disturbances into account). However, to successfully implement closed-loop property control based on soft sensors, a systematic decoupling of the geometry evolution of the workpiece as well as the mechanical properties of interest must be established.

As the mechanical properties of the workpiece are dictated by the underlying microstructure evolution during the forming process, another central question lies in the identification of suitable sensors and/or measurement technique that can detect a change

in the microstructure evolution best case inline. As the workpieces need to be fully intact for application, the measurement technique must be of non-destructive nature or at least semi-destructive nature. Non-destructive testing techniques in this context refers to the components analysis regarding their fitness for service without impacting or degrading their properties [5,6]. Whereas semi-destructive testing refers to methods that may cause small cavities in the component after testing, however, having little to no impact on the properties [7,8].

Thus, dependent upon the characteristics/microstructure evolution, the material and positioning possibilities in the process, suitable measurement techniques need be established.

Furthermore, the detected microstructure evolution should be correlatable with macroscopic characteristics, meaning that dependent upon the characteristics of interest, the choice needs to be focused.

This entails that a method for the description of the correlation between the (now detectable) microstructure evolution and the product property to be monitored needs to be established. A promising method for this problem pose so-called soft sensors. The name is derived from “software” and “sensor” as they are usually made up of an arrangement of at least one sensor or measurand in combination with a software/mathematical modelling approach to estimate the relationship between the measured quantities and the sought variables [9–12]. Soft sensors find their application in all kinds of disciplines and keep gaining in relevance due to their remarkably quick nature of evaluation, which becomes increasingly important in the automization of processes and systems. Their application fields include but are not limited to medicine and pharmaceuticals [13–17], robotics [18–20], and various engineering disciplines, such as process design in the petrochemical industry [21], autonomous driving [22] or even in wastewater treatment processes [23]. When choosing soft sensors as a monitoring/estimation technique, adequate modelling techniques must be established. These are dependent especially upon (1) the monitored properties and (2) the industrial process, thus the resulting system.

The overall goal of this thesis is the implementation of a soft sensor, that reliably derives mechanical properties of interest in freeform bent tubes. This endeavour raises the following research questions: (1) Which DOF in the process design may be used, that will enable the influence of the mechanical properties of interest, preferably without simultaneously influencing the geometry evolution of the workpiece, (2) how could a soft sensor be used to derive mechanical properties of interest (namely strength, residual hoop stresses and induces plasticity) during the freeform bending process based upon UCI hardness measurements and (3) how could this soft sensor furthermore allow the derivation of residual axial stresses based on Barkhausen noise (BHN) measurements. These questions present the core of this theses and will be addressed in the following chapters.

# 2 Fundamentals

This section will address the fundamentals of materials theory. It will introduce how strength, ductility and residual stresses result due to plastic deformation. It will highlight underlying magnetic properties in materials. Furthermore, this section discusses bending processes and especially the set-up of the freeform bending with movable die process. Furthermore, the state of the art regarding measurement equipment for a monitoring of product properties and last but not least possibilities for soft sensor design are introduced.

## 2.1 Materials theory

Materials treated in technical forming processes will inevitably undergo changes in material characteristics. As a result of the externally applied forces, the material will go through so-called elastic and plastic deformation. When the forming limits of the material are exceeded, the loss of material cohesion occurs. Whenever a component is exposed to the external force, initially, elastic deformation occurs. Elastic deformation is reversible meaning, after the external force is removed, the body will return to its initial state. This is due to a distortion of the crystal lattice. When tensile stress is applied, attractive interatomic bonding forces become effective; when compressive stress is applied, repulsive bonding forces dominate. They cause the building blocks to return to their initial state, when load is removed. As the forces on the body increase, once a critical force is exceeded, irreversible changes, namely plastic deformation takes place [24–26].

Elastic and plastic materials properties may be best explained, especially in uniaxial stress states, by the so-called stress-strain curves that are generated using tensile tests. Generally speaking, one differentiates between engineering stress-strain curves as well as true stress-strain curves. A schematic depiction of named curves including all important information is seen below, Figure 2-1. The most important mechanical characteristics are briefly explained below.

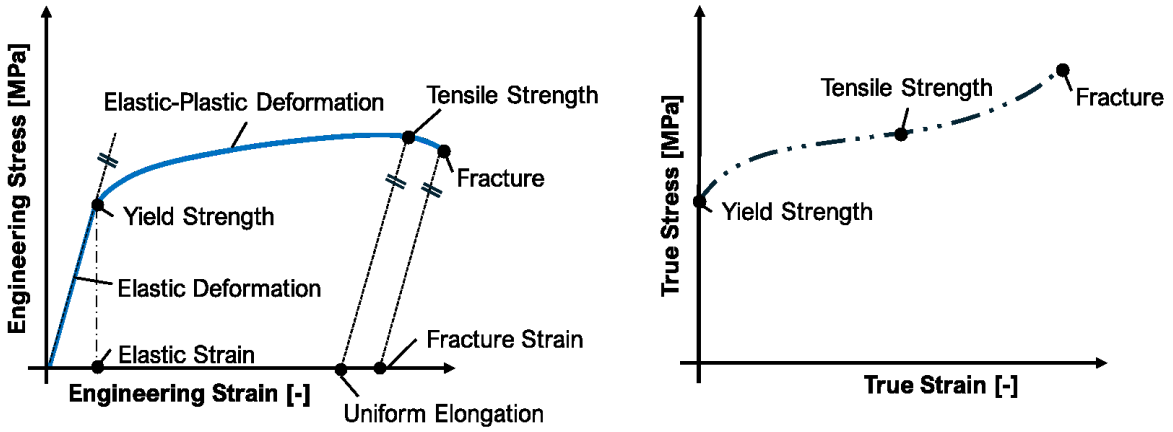


*Figure 2-1: Schematic depiction of engineering stress-strain curves and true stress-strain curves with indications of the most important parameters. Curvature to the left in true stress-strain curve is due to changes in cross-section after necking resulting in higher stresses.*

Stresses in this context refer to forces distributed within a component, acting upon an area.

Engineering stress can thus be defined as:

$$\sigma = \frac{F}{A} \qquad \textit{Formula 2-1}$$

Where $F$ the force applied usually in Newton [N] and $A$ the cross-section the force is acting upon.

The engineering strain in this scenario is closely related to the elongation of the material and is defined as:

$$\varepsilon = \frac{\Delta L}{L_0} \qquad \textit{Formula 2-2}$$

Meaning the change in length $\Delta L$ related to the initial length $L_0$.

In the engineering stress-strain diagram, this deformation is initially characterized by a linear increase up to the yield strength, a characteristic strength of a material where the material starts to so-called flow. This elastic behavior especially for uniaxial stress state may be described by Hooke's Law:

$$\sigma = E * \varepsilon \qquad \textit{Formula 2-3}$$

Where $E$ is the young's modulus, a material specific characteristic that describes the materials resistance towards elastic deformation [24–27].

Once the yield strength is reached and thus the elastic limit exceeded, the elastic deformation is superimposed by the plastic deformation. In the stress-strain curve this is indicated by a deviation from the linear trend. With further plastic deformation, a continuous increase in dislocation density can be observed. Dislocation interactions increasingly occur, which lead to the hardening of the material, reflected in the further increase of the curve. Parallel to the physical hardening of the material, the so-called geometric softening must be taken into account. Due to the volume constancy, the

cross-section of the material decreases with the plastic elongation of the specimen. In the range until uniform elongation, the hardening is greater than the geometric softening, which results in the increase in the stress-strain curve. Macroscopically speaking, a homogeneous deformation is observed in the range of uniform elongation [26,28].
If the material continues to be deformed, both elastic and plastic strain components are present under load. Hence, the total strain therefore includes both reversible as irreversible deformation components. If the material is now alleviated of its load, the reversible, elastic strain component (according to the linear-elastic theory) jumps back with the same gradient as in the area of mere elastic loading. After the material has been completely relieved of its load, the remaining strain reflects the true plastic strain [26,28].
As the deformation further increases, the hardening of the material decreases. At maximum force, the hardening reaches zero; this is a state in which so-called necking starts accompanied by a decrease in force again. The force at maximum load related to the cross-section is referred to as tensile strength. It indicates the maximum load the test sample can withstand. The corresponding elongation is called uniform elongation [26,28]. After necking occurs, the hardening is smaller than the geometric softening. Necking begins to increase, when loading is still ongoing and will eventually lead to the fracture of the material. As essentially only the area of necking continues to deform, the deformation conditions are now macroscopically inhomogenous and stress state is no longer uni- but multiaxial [26,28].
In the technical stress-strain diagram, the nominal stress is plotted, i.e. the force related to the initial cross-section. With increasing strain on the material, however, there is a significant reduction in the cross-section. Particularly in the area of necking, the reduction in cross-section is so significant that the true stress is considerably higher than the nominal stress. The true stress-strain diagram is therefore used to assess the true hardening behavior of a material. To obtain true stress and strain, the force is not related to the initial values of cross-section and length, but to the instantaneous values. In the area of uniform elongation, the volume constancy must be considered when calculating the true stress [26,28]. Hence, the true stress up to the force maximum is defined by:

$$\sigma_T = \sigma\,(1 + \varepsilon) \qquad \textit{Formula 2-4}$$

After necking occurs, a correction factor must be considered, which includes geometric changes under increasing loading.
The true strain (also called degree of deformation) may be defined as:

$$\varepsilon_T = \varphi = ln\,(1 + \varepsilon) \qquad \textit{Formula 2-5}$$

### 2.1.1 Strain hardening and ductility

Forming processes and hardening processes are intricately linked. During the forming process, changes within the microstructure always occur. Nowadays, during forming processes, the objective is usually to find a good balance between the changes in microstructure and shapes as to achieve a desired set of properties in the workpiece [29].

As previously addressed, when materials are formed, the material starts to harden, predominantly due to so-called strain hardening. This occurs primarily because of the increase in dislocation density in the material. Forming parameters, such as the degree of deformation ($\varphi$) and the strain rate ($\dot{\varepsilon}$), are factors that primarily influence the strain hardening behavior of materials. Particularly, $\varphi$ influences the density and arrangement of dislocations, but also grain morphology, and phase distribution in the material. Cold forming, which occurs below the material's recrystallization temperature, results in increased dislocation density with rising $\varphi$, leading to material strain hardening and reduced elongation capacity [25,29].

The strain rate $\dot{\varepsilon}$, however, only has a notable impact on body-centered cubic materials, where it mainly influences the yield and tensile stress of the material. For high strain rates $\dot{\varepsilon} > 10^{-2} 1/s$ the heat transfer between the workpiece and its surroundings becomes insufficient. Consequently, the component heats up, resulting in a subsequent decrease in yield and tensile strength of the workpiece [26,28,29].

Ductility, in materials science, refers to the ability of a material to undergo (significant) plastic deformation before fracture [26]. One can anticipate the ductility of a material from the stress-strain diagram, Figure 2-1, by observing the strain on the x-axis. Usually, a high strength of a material always comes at the expense of its ductility. High strengths combined with high ductility is therefore difficult to achieve. However, materials with low ductility have low formability, as they tend to fail at low degrees of deformation [26].

Therefore, from a materials engineering perspective, a good compromise between the due to strain hardening occurring changes in strength and ductility must be found, without risking failure of the workpiece during its application.

### 2.1.2 Basics of continuum mechanics

In the age of digitization and the simultaneous advancements in computational power, the continuum mechanical description of materials and components takes on a defining role. As previously explained, stresses can be defined as forces that act upon an area, however, real components are, when in use, not only stressed in one direction. Rather, they must absorb forces from different directions. The resulting stress state can be described by three perpendicular stress vectors, that also compose the Cauchy stress tensor – a unique representation of every stress state at any defined point in the workpiece.

$$\bar{\bar{\sigma}} = \begin{pmatrix} \sigma_{11} & \tau_{12} & \tau_{13} \\ \tau_{21} & \sigma_{22} & \tau_{23} \\ \tau_{31} & \tau_{32} & \sigma_{33} \end{pmatrix} \qquad \textit{Formula 2-6}$$

Stresses in the stress tensor can be divided into two types, normal stresses ($\sigma_{ij}$) as well as shear stresses ($\tau_{ij}$), whereas index denoted $i$ refers to the direction of the surface normal, and $j$ the direction of the stress component [30].

In principle, the components of the stress tensor are direction dependent. However, the coordinate system of the stress tensor may be rotated to achieve a principal axis transformation. In this form, the shear stresses become zero and only normal stresses, then called principal stresses; $\sigma_1$, $\sigma_2$, and $\sigma_3$ remain. The transformation of the Cauchy stress tensor into principal axes form is done using the Kronecker delta, $\delta_{ij}$ [31]:

$$\left|\sigma_{ij} - \delta_{ij}\,\sigma\right| = 0, \text{ with } \delta_{ij} = 1 \text{ for } i = j,\ \delta_{ij} = 0 \text{ for } i \neq j \qquad \textit{Formula 2-7}$$

The resulting equation may be described based on the three invariants, $I_1, I_2$ and $I_3$ of the stress tensor.

$$\sigma^3 - I_1\sigma^2 + I_2\sigma + I_3 = 0 \qquad \textit{Formula 2-8}$$

By solving this equation, the three principal normal stresses $\sigma_1$, $\sigma_2$, and $\sigma_3$ can be determined. The invariants are described by the following relationships:

$$\begin{aligned} I_1 &= tr\,\sigma \\ I_2 &= \frac{1}{2}[(tr\,\sigma)^2 - tr(\sigma^2)] \\ I_3 &= \det\sigma \end{aligned} \qquad \textit{Formula 2-9}$$

Hence, the stress tensor then results to:

$$\bar{\bar{\sigma}} = \begin{pmatrix} \sigma_1 & 0 & 0 \\ 0 & \sigma_2 & 0 \\ 0 & 0 & \sigma_3 \end{pmatrix} \qquad \textit{Formula 2-10}$$

Furthermore, the stress tensor can be separated into two parts: a deviatoric and a hydrostatic part. Here, $p$ is the hydrostatic part of the tensor, $I$ is the unit tensor and $s$ the deviatoric part of the tensor.

$$\sigma = s + I\,p \qquad \textit{Formula 2-11}$$

The hydrostatic tensor is defined as:

$$p = -\frac{1}{3}tr\,(\sigma) \qquad \textit{Formula 2-12}$$

Analogously, to the invariants of the stress tensor, the three invariants of the deviatoric stress tensor may be defined [30,31]:

$$J_1 = 0$$
$$J_2 = \frac{1}{2} tr(\sigma^2) \qquad \textit{Formula 2-13}$$
$$J_3 = \det \sigma$$

### 2.1.3 Basics of plasticity

As previously described, after surpassing the yield point of a specific ductile material, the material will begin to deform plastically. In continuum mechanics, this phenomenon goes in hand with the assumption that the occurring stresses, $\sigma$, in the material, due to the applied external forces, reaches a material and deformation characteristic critical stress value, $\sigma_e$. In literature, the description for $\sigma_e$ is manifold. However, the most predominant approaches are those of von Mises and Tresca [31].

$$\sigma_{e,M} = \frac{1}{\sqrt{2}} \sqrt{(\sigma_1 - \sigma_2)^2 + (\sigma_1 - \sigma_3)^2 + (\sigma_2 - \sigma_3)^2} \qquad \textit{Formula 2-14}$$

$$\sigma_{e,T} = \sigma_1 - \sigma_3 = 2\tau_{Max} \qquad \textit{Formula 2-15}$$

As there are several influencing factors the affect the flow behavior of metallic materials, these approaches are continuously refined [32–36]. Researchers have designed flow criteria that take factors such as anisotropy [33–35], strain rate and temperature dependencies [32] or the stress state [36] into account. As this work uses von Mises plasticity, a strain rate and temperature-independent as well as isotropic consideration is sufficient.

Mathematically speaking, the material starts to flow as soon as the flow potential, $\phi$, reaches or goes below zero [37].

$$\phi\,(J_2) = \bar{\sigma}_e - \bar{\sigma}\left(\bar{\varepsilon}_p\right) \leq 0 \qquad \textit{Formula 2-16}$$

Where $\bar{\sigma}\left(\bar{\varepsilon}_p\right)$ may be described using different approaches such as Hollomon, Ludwik or Voce. This work uses a combination of the approaches of Ludwik and Voce [38].

$$\bar{\sigma}_{Alpha}\left(\bar{\varepsilon}_p\right) = \alpha * \left(b + A\,\bar{\varepsilon}_p^{n}\right) + (1-\alpha)\left[k_0 + Q(1 - \exp\left(-\beta\bar{\varepsilon}_p\right))\right] \qquad \textit{Formula 2-17}$$

The parameters $b$ and $k_0$ the yield strength in the respective model, $n$ denotes the respective hardening exponent of the material, parameters $A, Q$ and $\beta$ are fitting parameters. Parameter $\alpha$ is a weighting parameter for each mathematical law and ranges between 0 and1.

### 2.1.4 Residual Stresses

Residual stresses are defined as statically effective multiaxial stresses in mechanical equilibrium that exist in a closed system without any external forces or moments [39]. They occur in all kinds of materials such as metals, ceramics or plastics just to name

a few, while the severity of the residual stresses depends not only on the material, but also its microstructure or the thermal treatment thereof [40].
Residual stresses are commonly categorized regarding their range, namely residual stresses of type I, II and III [40]. A visualization of the different types of residual stresses can be taken from the following Figure 2-2.

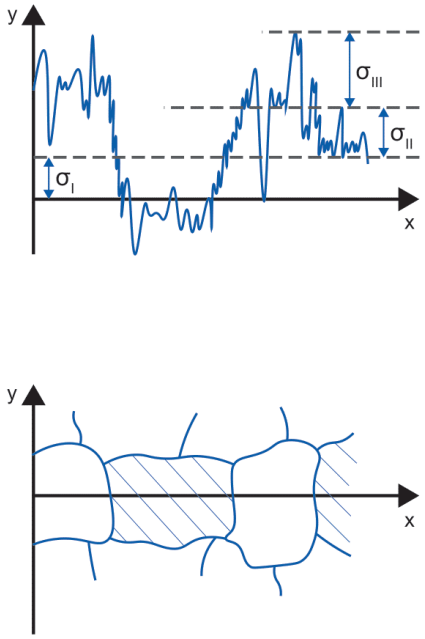


*Figure 2-2: Classification of residual stresses according to Macherau et al. [40]*

Type I residual stresses, oftentimes also referred to as macroscopical residual stresses, are homogenous across larger material ranges (several grains) and are most pronounced close to the surface of a workpiece. Whenever the equilibrium is disturbed, residual stresses of type I always lead to macroscopical dimensional changes [41,42].
Type II residual stresses are largely homogenous across smaller regions such as single grains or grain regions, and are thus oftentimes referred to as microscopical residual stresses. Whenever an equilibrium across several grains is disturbed, residual stresses of type II can also cause macroscopical shape changes or cracks in the workpiece [39].
Type III residual stresses are distributed inhomogenously across smallest areas such as atomic distances. These types of residual stresses are on an atomic level and when disturbed do not lead to a shape change macroscopically [43].
All types of residual stresses are influenced by nearly all manufacturing processes and can occur due to, e.g. mechanical stresses, thermal conditions, or chemical differences. Habschied et al. [41] explains, that mechanical stresses can cause locally varying levels of plastic deformation in the workpiece causing residual stresses. Thermally induced residual stresses occur when areas in a component cannot fully thermally expand leading to a local plastic deformation. Furthermore, chemically speaking diffusion

processes can lead to a distortion of the crystal lattice (due to nitriding of a component's surface, for example), causing residual stresses [41].
Most of the time, residual stresses in a workpiece can be neglected. However, in some cases, the residual stress state dictates further processing steps as well as the service application of the workpiece. They can be of both compressive and tensile nature and of different orientation, namely axial, radial and hoop direction, within the workpiece. While compressive residual stresses may improve the component performance, tensile residual stresses in a workpiece under load can lead to an overlapping of stresses and render the component useless. If neglected then, the residual stress state can lead to failure of the workpiece, in form of e.g. distortion, crack formation or even detrimental failure [41].

### 2.1.5 Magnetism

Solids exhibit three main forms of magnetism. These forms are namely, diamagnetism, paramagnetism and ferromagnetism, which are closely related to the underlying details of their band structures [44–46].
When an external magnetic field is applied to a diamagnetic material, the magnetic field $H$ causes a current within the electron shell of the atom, whose own magnetic field $M$ is opposite to the external field. The induced magnetic moment thus tries to weaken the external magnetic field, the magnetic susceptibility $\chi$ is hence negative. The following formulaic relationship holds true, where $M$ is the magnetization, and $H$ the magnetic field strength and $\chi$ the magnetic susceptibility [45,46]:

$$M = \chi H \qquad \textit{Formula 2-18}$$

Paramagnetic substances are those whose atomic shells do exhibit a magnetic moment, which is always the case if the electron shell is not filled. However, as the magnetic moment can point into all spatial directions, the magnetization of a paramagnetic material is zero on average. When an external magnetic field is applied to a paramagnet, the magnetic moments align themselves as they precess around the orientation of the external field. Magnetic moments that are opposite the external field have a higher energy, such that they tend to rotate into field direction. In this manner, the solid attains a magnetization that is proportional to the external field at small field strengths. Formula 2-18 still holds true however, $\chi > 0$. Whenever large field strengths are applied, all magnetic moments will eventually align in field direction ultimately leading to magnetic saturation. Thermal activation, however, counteracts the alignment, so that $\chi$ decreases with increasing temperatures. Curie's law of paramagnetism applies, where C is a constant:

$$\chi = \frac{C}{T} \qquad \textit{Formula 2-19}$$

The third type of magnetism in solids to be discussed is so-called ferromagnetism. Compared to paramagnetic materials, ferromagnets possess a spontaneous magnetic

moment, meaning a magnetic moment without the presence of an external magnetic field. The spontaneous magnetization results from electrons having their spins in the substance align in the same direction. For this to occur, an internal magnetic field, $H_e$ must exist. This internal magnetic field originates from the interaction of the spins among each other and is called exchange field. The magnetization of the ferromagnet is proportional to the exchange field:

$$H_e = \lambda M \qquad \textit{Formula 2-20}$$

where $\lambda$ is a temperature-dependent material constant. When all spins are aligned, maximum magnetization, i.e. saturation magnetization is reached. The internal magnetic field, $H_e$, is so large that it aligns essentially all spins. However, this alignment is counteracted by increasing temperatures. Hence, the saturation magnetization decreases with increasing temperature and becomes zero at a critical temperature, $T_c$, called the Curie-temperature. Here, the spontaneous magnetization disappears and the material behavior is paramagnetic [46]. The Curie-Weiss law now applies:

$$\chi = \frac{C}{T - T_c} \qquad \textit{Formula 2-21}$$

In ferromagnetic materials, oftentimes a magnetization well below the saturation magnetization is measured, which is due to the magnetic microstructure of the ferromagnetic solid. It is made up of so-called domains where electron spins are uniformly aligned, but the alignment in the separate domains varies. The interfaces between these magnetic domains are called Bloch walls, that shift around whenever an external magnetic field is applied. This shift occurs in such a way that the domains that are oriented along the magnetic field grow at the cost of the remaining domains, see Figure 2-3.

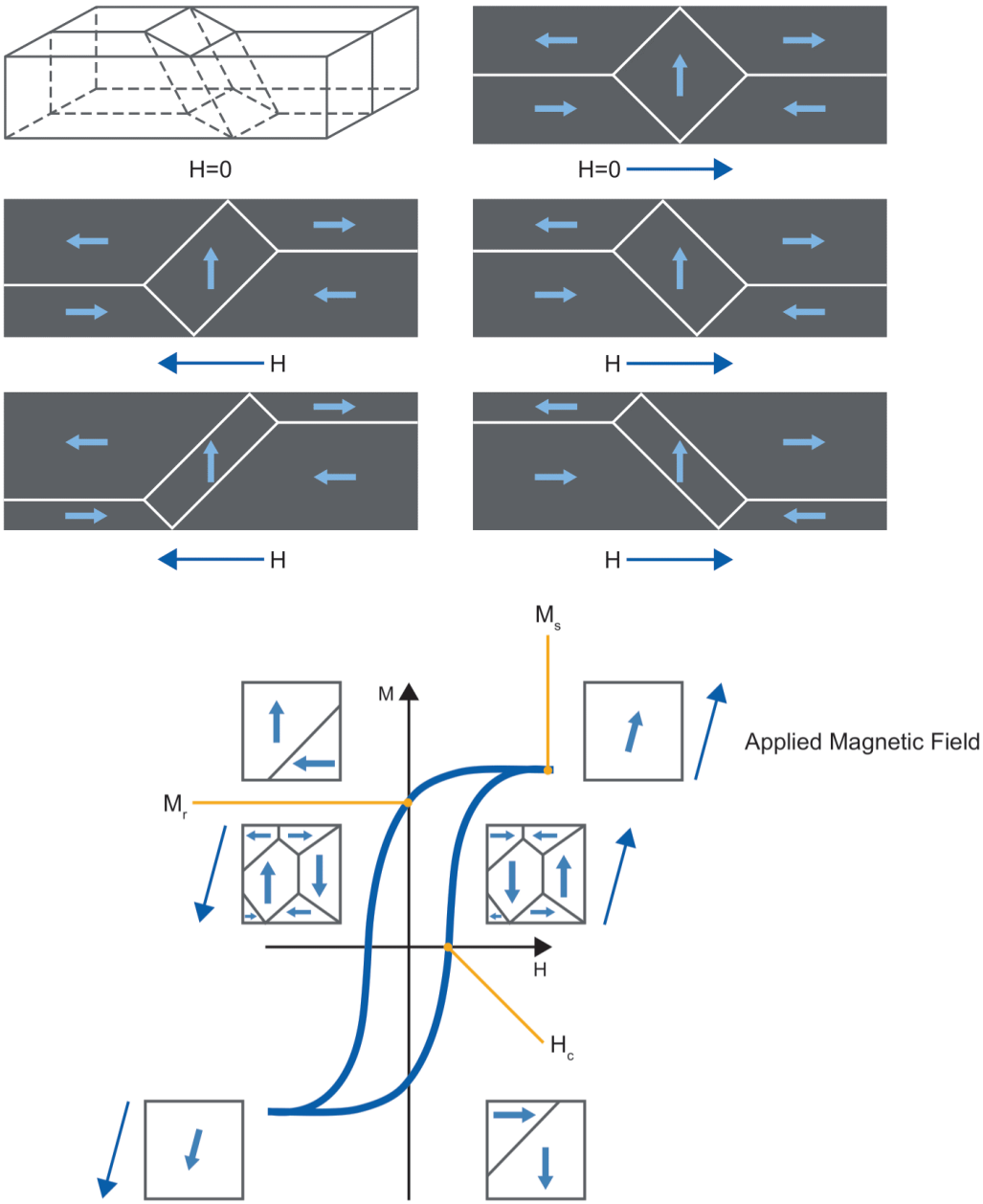


*Figure 2-3: Bloch wall movement during magnetization – the domains in direction of the applied magnetic field grow at the expense of the others; change in the domain structure while traversing the hysteresis curve.*

As the magnetization increases, magnetic saturation is reached, once the sample consists of one single domain and the spins all lie within the magnetic field direction. If the magnetic field is turned off, a residual magnetization remains that can only be dissipated when an field strength opposite to the direction of the residual magnetization. The magnetization of a ferromagnetic solid as a function of the field strength of an externally applied magnetic field is known as the so-called hysteresis loop [46]. It characterizes the non-linear, history-dependent course of the magnetization as a function of the field strength [47]. The hysteresis is obtained through the measurement of the resulting magnetization within the sample and allows general statements about the course of the remagnetization process. The variables $M_S$ (saturation magnetization)

$M_R$ (residual magnetization) and $H_c$ (coercive field strength) define the hysteresis curve, see Figure 2-3. When saturation magnetization is reached at low field strengths, the material is referred to as soft magnetic and the hysteresis loop is narrow. Hard magnetic materials have a high saturation field strength and therefore a broad hysteresis loop. A schematic depiction of a soft and a hard magnetic material can be seen in the following Figure 2-4.

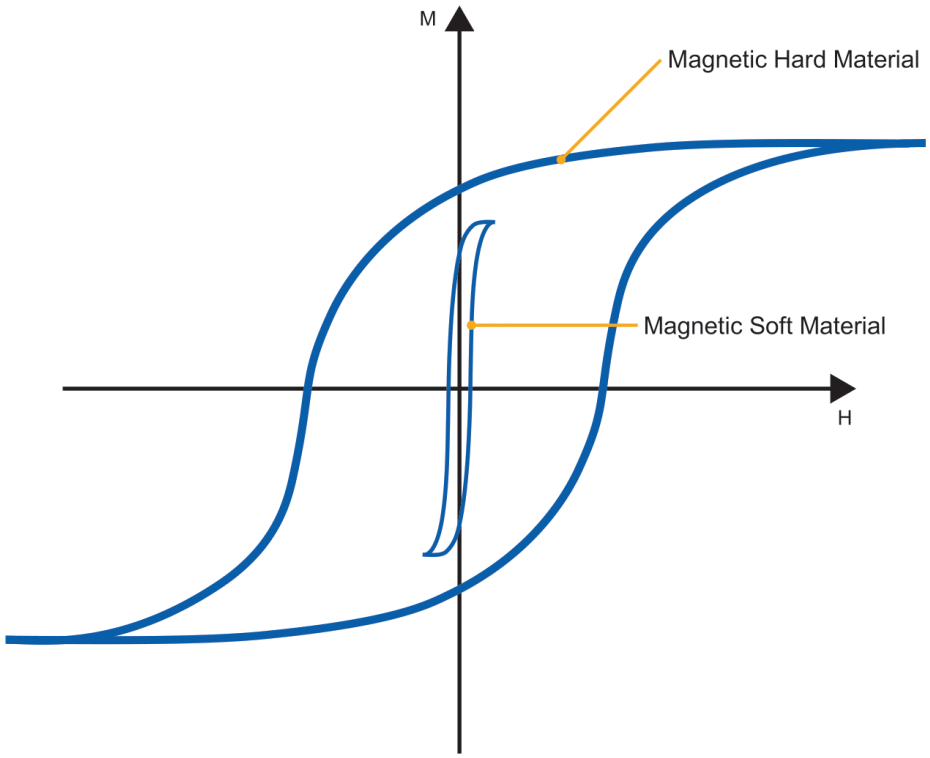


*Figure 2-4: Schematic depiction of a hard magnetic and soft magnetic material adapted from [46].*

## 2.2 Forming Technology

The beginnings of forming technology are linked to the realization that certain materials can be formed in a desired shape under the influence of specific external forces. According to DIN 8580, forming is manufacturing in changing the shape of a solid body in (plastic) manner while retaining both the mass and the material composition [48]. Thus, they belong to the chipless manufacturing processes. Forming processes are defined within DIN 8582 to 8587 and are classified into five groups according to the main differences in effective stresses or loads: (1) pressure forming, (2) tensile-compressive forming, (3) tensile forming, (4) bending and (5) shear forming. As the main focus of this work lies on the process of freeform bending with movable die, the following section will highlight most important advances in bending processes. It gives a

closer insight into freeform bending with movable die and lastly will highlight the numerical modelling thereof.

### 2.2.1 Bending processes

Bending is standardized in DIN 8580, where it is defined as a manufacturing process in forming technologies as well as in DIN 8586, where it is defined as the forming of solid bodies, whereby the plastic state is induced through a bending action [48,49]. The classification of the individual processes is based on the tool movement. It is differentiated between linear and rotary movements of the bending tool and the bending with active energy. According to standard VDI 3430 some examples of bending processes with rotary and linear tool movements are given below, Figure 2-5 [50].

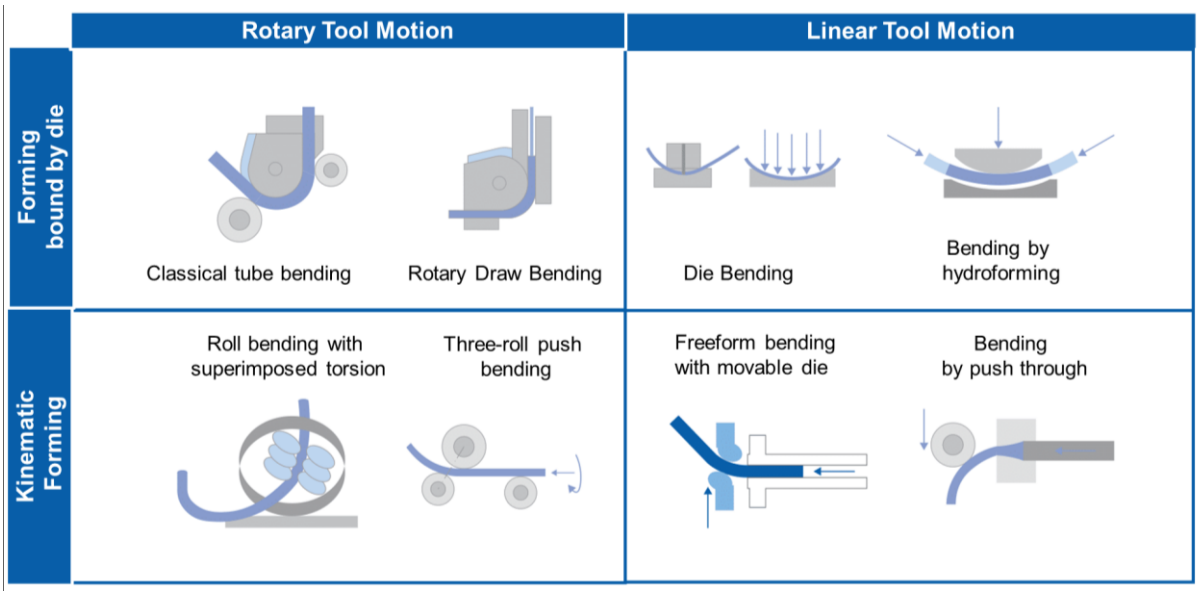


*Figure 2-5: Exemplary classification of bending processes based on VDI guideline 3430.*

The most widely used bending process in the industrial sector is the rotary draw bending (RDB) process, which is categorized above in the section rotary tool movement and bound by die contour. Here the cavity within which the semi-finished product is guided is equivalent to the outer dimensions of the semi-finished products cross-section [50,51].

During RDB, according to VDI 3430 and Hinkel [52], a bending moment which is superposed by a force in longitudinal direction needs to be induced to form the semi-finished product. Additionally, to round tubes of various dimensions, especially with regard to wall thickness and outer diameters, the most common semi-finished products for RDB include various solid and hollow profiles. The process finds its application particularly for bending tasks with tight radii and thin-walled tubes [53]. According to Hoffmann et al. [25] even radii well below the diameter of the tube are bendable, although this is an exception. A major disadvantage of this process is that a separate bending mold is required for each bending radius and a separate set of bending tools

for each chosen bending geometry [51]. In the following figure, a schematic depiction of the RDB process is given. All relevant parameters are marked accordingly, see Figure 2-6.

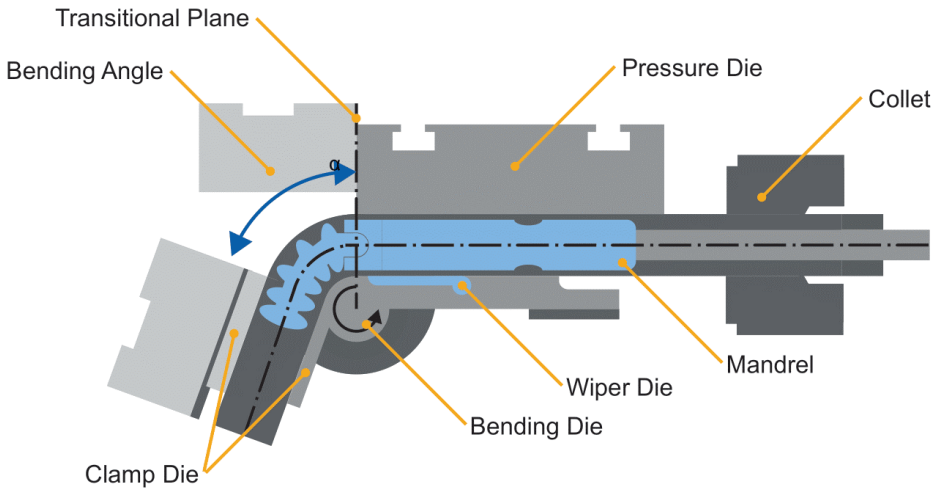


*Figure 2-6: Schematic depiction of the RDB process according to [54].*

As the process begins, the semi-finished product is fixed in the chuck towards the end and is clamped between two clamping dies at the front. As the forming starts, the bending die and the clamping dies begin to rotate and the clamped semi-finished product is bent along the cavity of the bending die [50]. To avoid buckling or wrinkling as far as possible in complicated bending tasks, bending mandrels adapted to the specific use case are employed. Furthermore, the component is supported from the outside by a wiper die during the bending.

RDB is widely used in the industry, mainly due to the high quality of the bent components, the precise execution of various bending tasks, the good reliability and the advanced level of development. However, RDB also shows significant limitations as the process is form-bound. A major limitation lies in the need for a straight segment lying between two bend segments, that can only be avoided with a considerable additional effort in tool production. Additionally, new tools need to be manufactured for each new bending geometry, which makes the process cost-intensive and also significantly restricts freedom in design [55,56].

Unlike the conventional form-bound bending processes, kinematic bending processes offer the decisive advantage of flexibility and provide almost complete freedom of design for the bent component (whilst staying within the limits of the process). In kinematic bending processes, the bending line is generated by the relative movement of the bending tools with regard to each other as well as the semi-finished product that is being bent. Additionally, the bending tools are designed according to the contour of the semi-finished product, thus, they may be used even if the bending line is adjusted. This

entails that various bending geometries may be produced on the same bending machine whilst using the same set of bending tools. Compared to their conventional, form-bound counterparts, kinematic bending processes offer a significantly higher design flexibility, and a wider range of parts may be produced. Furthermore, the costs of the tools are substantially lower [57].

However, kinematic processes are very susceptible to semi-finished product, process, or tool-related disturbances [58]. Various studies additionally have shown that fluctuations in geometric as well as mechanical properties of the semi-finished product have a major influence on the quality of the bent components in kinematic bending [56,59,60]. Even though, kinematic bending processes have a wide range of DOF that may counteract these disturbances, according to Hoffmann et al. [25] it is precisely these DOF and their interdependencies which is the reason for the low degree of automation of the processes. The complexity with the accompanying lack of process knowledge entails that kinematic bending processes are typically still empirically configurated and adjusted by experts [57].

The two most industrially relevant representatives of kinematic bending processes are freeform bending with movable die as well as 3-roll bending or its extension, the 3-roll push bending. As freeform bending with movable die represents the within this work researched process, it is considered in detail in Chapter 2.2.2. Hence, this section will shed light on the 3-roll push bending process, which also allows the bending of freeform contours. Generally speaking, 3-roll push bending may be utilized for different cross-sections and is usually employed for series production of medium to large quantities [25,58]. According to Groth [57], it allows the production of large bending radii in components with continuously varying curvatures [57]. Figure 2-7 shows a schematic depiction of said process and highlights all relevant tool components.

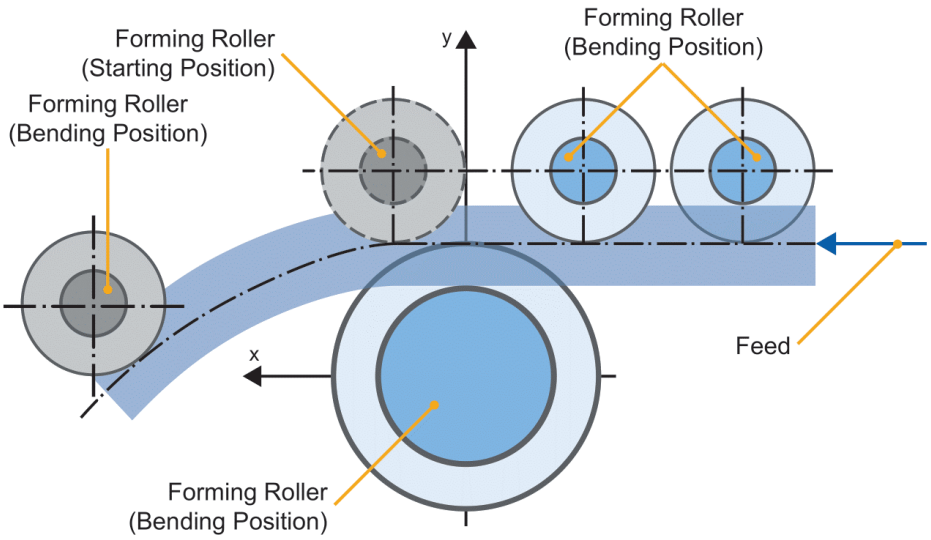


*Figure 2-7: Schematic depiction of 3-roll push bending adapted from [61].*

At the beginning of the process, the semi-finished product is inserted between rollers and is clamped in the feed unit toward the rear end. To simplify loading of the semi-finished component, the pressure and forming rollers may be moved away from the bending roller. The feed unit can push the component as well as rotate it along its longitudinal axis, enabling the bending of three-dimensional bending geometries. To increase guiding capabilities as well as to ensure greater dimensional accuracy, at least two pressure rollers are installed in the process, see Figure 2-7.

After loading the machine, the pressure rollers and forming rollers move back toward the bending roll, to fasten the component/tube. The forming roller then moves towards the set bending position, which in turn defines the curvature of the bent component. The position of the forming roller may be chosen as desired and needed in terms of final bending geometry, while staying within the physical limits of the tools and process. As the forming roller is moving into position, the feed unit moves the component. Dependent upon the distance travelled by the feed unit the bending angle can be set. If, on the other hand, free-form geometries are to be bent, the position of the forming roller and the rotation of the tube must be adjusted to the desired curvature of the bending line during the ongoing process. After the bending process has been completed, the bent tube is either taken out of the machine manually or with a robot-assisted handling system for further processing [57].

Another example of a process that allows the bending of three-dimensional components is the so-called Hexabend process, which is characterized especially by its six hydraulically, length-adjustable supports. As in most bending processes, the component is moved continuously, longitudinally using a feed unit. During feeding the component is pushed through the guide unit and a movable die. The forming itself is carried out because of the movement of the bending die due to the hydraulic supports [62,63].

### 2.2.2 Freeform bending process with movable die

As this work proposes a soft sensor for freeform bending with movable die, the following section will shed light on the process, its advantages, and disadvantages as well as its current state of the art.

Freeform bending with movable die is characterized by the semi-finished product that is bent by a relative moment of the bending die to a fixed guide, while the component is continuously fed through the machine. The classical set up of the process consists of a movable die, a statically positioned guider as well as a feed unit. For most bending operations, a mandrel within the component is utilized for further support during the process as well as to enhance quality of the workpiece. The following picture shows a schematic overview of the process, highlighting all relevant tools, Figure 2-8 [56,64].

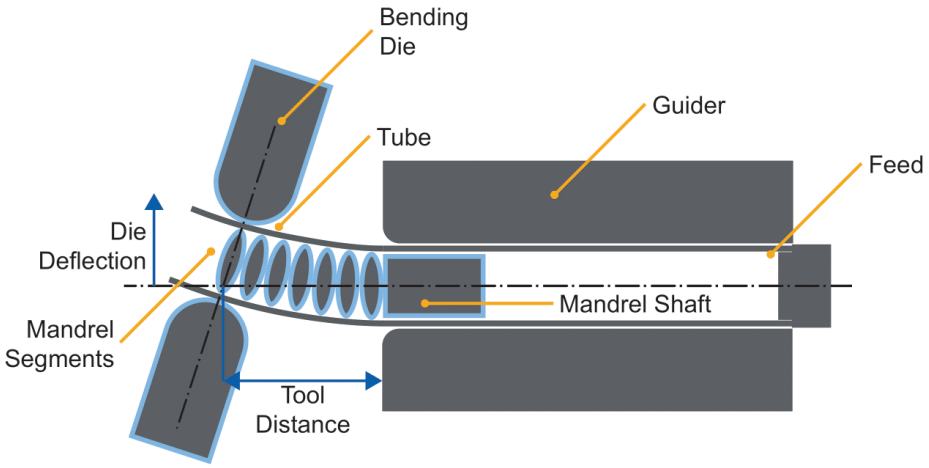


*Figure 2-8: Schematical depiction of the freeform bending process with movable die.*

During freeform bending with movable die, the position of the bending die is controlled by servomotors for each individual axis, whereby both the translation and the rotation of the die can be adjusted [57,64]. Freeform bending processes may have different amounts of DOF. Currently, the market offers freeform bending machines that have either three, five or six DOF. One DOF always lies in the feed unit, that moves the component along the tube axis at a constant feed rate. For machines with three available DOF, the bending die may be moved translationally on the xy-plane. If the machine at hand also allows the guided rotation around the x- and y-axis, a machine with five DOF is used. Any rotations of the bending die are controlled by a movable bearing within the bending head. Freeform bending machines with six DOF may be considered the latest advancements for this type of process. Additionally, to the previously described DOF, this type of process allows the rotation of the entire bending head around the axis of the feed. This offers further freedom of design when bending round tubes and is particularly advantageous whenever components with symmetrical and asymmetrical cross-sections are bent as torsion may be superimposed on the components. Newest research shows that torsion may have both positive as well as negative effects

on spring back behavior of oval 304 stainless steel profiles [65]. Despite their differences, all forms of freeform bending enable a flexible bending of the most complex geometries, while the needed tools are kept to a minimum [57].
In freeform bending with movable die, the kinematics of the machine can be categorized into three stages: (1) deflection, (2) bending in constant range and (3) back deflection [64]. During the deflection, the bending die rotates and translates through the servomotors into the set position, while the component is continually pushed forward at constant feed rate. Once the point of maximum deflection and rotation is met, this position is maintained until the desired bending angle is attained. At the end of the tube bend, the bending die moves either back into its original position or directly into the next bending position [64].
Due to spring back effects, that are highly individual regarding the semi-finished product properties, such as initial geometry and mechanical properties, usually the desired geometry and the attained geometry are not identical. This means, that a correction factor that is determined empirically must be established for the chosen semi-finished product. This usually entails a time and cost intensive trial and error procedure for each new material as well as semi-finished component geometry. Hence, there is a strong need, for a closed-loop control that considers product properties and may influence the DOF of the freeform bending machine at hand such that the desired geometry and mechanical properties are met. Maier [64] describes in his work, how actuators in a six DOF freeform bending process may be set, such that a closed-loop control can be established for geometric parameters, yet only taking mechanical properties qualitatively into account. This work, additionally, introduces a concept that derives relevant mechanical properties during the freeform bending process such that a closed-loop control not only corrects geometry but also the desired mechanical properties in the tube.

### 2.2.3 Numerical Modelling using FEM

As just established, the problem in kinematic bending processes lies in the intensive trial-and-error procedure to establish parameters for production such that the final component lies within the desired tolerances. A remedy for this time-consuming, resource-inefficient trial-and-error process is the numerical modelling of such a process. Several works before have taken on the task of a numerical modelling of the freeform bending process (using varying DOF) within the past few years. This section gives a short overview of the most important results.
First FEA models by means of LS-Dyna of the freeform bending process with three and five DOF were introduced by Gantner et al. [60,66]. Here, the process is modeled with fully integrated quad shell elements with five integration points along the thickness of the tubes, while the bending tools are defined as rigid bodies. Friction between the tools and the component is derived by Coulomb's law with a friction coefficient of 0.04. To describe the flow behavior of the material, databases were used. Their introduced

model shows good agreeability with physically measured bending angles and radii; however, a validation of the mechanical properties is neglected.
Beulich et al. also introduces a FE Model in LS-Dyna of the freeform bending process [67]. They introduce a model that considers six DOF for hydroforming process simulations; it models a mandrel made up of spherical segments, that are defined as rigid bodies. Furthermore, the simulated tube is modeled using Belytschko-Tsay shell elements with seven integration points. Beulich further introduces extensions of this initial simulation model: (1) by incorporating the manufacturing process of the tubes into the virtual model [68]; (2) by performing a sensitivity analysis regarding influencing parameters during the bending process and lastly [69] (3) in modelling a weld seam and its protrusion [56].
Another approach of modelling the freeform bending process (with five DOF) was introduced by Guo et al [70,71]. They present an Abaqus/explicit simulation model for tubes made out of brass. They model the tools, except for the bending die, using R3D4 elements; the bending die is modelled using CRD8R solid elements. The brass tubes are modelled using S4R shell elements. The overall goal is to obtain detailed insight into the process mechanisms for even small bending factors. Further studies by the team, show that a filling of the brass tubes with different substances influence the formability during the bending process. Different kinds of fillers (steel balls, rubber and a solid rod) were conducted and compared to the physical counterparts. Their results showed good agreement as well as the insight that the highest deformation is achieved by solid fillings, due to the strong support effect from within the tubes [72].
Werner et al. [73] adapt the six DOF model of Beulich et al. in their works, to derive a relationship between steel tubes and the kinematic movement of the bending die, without needing to conduct a plethora of physical, trial-and-error experiments. Their results show, that the model indeed is sufficient to anticipate good geometrical results within a defined process window [69,73]. Latest developments regarding the establishment of a virtual laboratory to minimize large efforts in trial-error-runs, lays the work of Maier [64]. His approach models process tools again as rigid bodies, whereas the tube is modelled using explicit, deformable shell elements, modelling the materials parameters based on tensile tests. His works validate the bending process and further introduce so-called non-tangential bending [64]. Non-tangential bending will be further thematized in Chapter 5.
Yet, these studies all lay their focus on the accurate modelling of the dimensions of the components. Some regard the mechanical properties, yet largely in qualitative nature. Thus, this work, will thematize the modelling of the mechanical properties within the tubes.

## 2.3 Metrology

To determine whether components are fit for service, their properties need to be characterized. In materials engineering, there is a manifold of measurement procedures that can qualitatively and quantitatively assess material/component characteristics, while giving detrimental information on how a component might be used and how it withstands everyday operation. Measurement procedures may be categorized into destructive, semi-destructive and non-destructive testing. All procedures yield information on the material properties, however, dependent upon the use-case one certain procedures might be more advantageous than others. The following sections will explain the differences in the testing procedures, their uses as well as some examples thereof.

### 2.3.1 Destructive testing

Destructive testing is usually a type of dynamic or static mechanical test that destroys the test object while the process is ongoing. During destructive testing, characteristic mechanical properties can be determined in a precise fashion that applies to the one tested specimen. Examples of destructive testing include, but are not limited to the tensile test, bending test and Charpy tests. Major advantages of these testing procedures are amongst others a reliable, accurate and quantitative data acquisition. The data determined is useful for design purposes and estimates regarding the lifetime of a material can be made within various conditions (be it different temperatures or gaseous/liquid environments). Yet, the major disadvantage of destructive testing is the destruction of the specimen during the process, which leads to the objects not being fit for service after testing, furthermore, the results are specimen specific [74,75].

### 2.3.2 Semi-Destructive testing

Semi-destructive tests are still categorized into the destructive tests, as they still bring about a breach in properties of the specimen, however, insignificant with regard to further application of the specimen. Hardness tests, especially, micro-hardness tests, leave an insignificantly small indent on the specimen's surface, so that further application is feasible. These testing methods usually also lead directly to a quantitative measurement of a certain characteristic of interest and can be used for a fast evaluation thereof, which is incidentally one of their major advantages [7,8,74,76].

### 2.3.3 Non-Destructive testing

Non-destructive testing is a test, evaluation, or examination of a test object without the testing procedure altering any kind of properties of the object. The goal of non-destructive testing is the determination of the state of the objects or disruptions thereof, that may affect the usability or service life of the object [74]. Non-destructive testing includes a diverse array of measurement and analysis methods employed to assess the present state of structural materials or components. This approach is usually swift and

efficient, offering the primary advantage of inspecting materials neither inducing harm nor changing the composition and form of the examined workpiece [74,75,77,78].
Dependent upon the use case, they find a variety of applications, such as quality control of bridge components [79], determining the fiber content in steel fiber reinforced concrete [80], strength measurement of float glass after indentation [81] or in the medicinal sector for mammography scans [82]. Advantages of non-destructive testing equipment are primarily the ability to make further use of the investigated specimen, oftentimes non-destructive testing is fast and cost efficient (except for radiographic analyses) and they give a quick estimate on concise changes in material, where measurements may even be performed on the entire workpiece [74]. However, usually measurements given by non-destructive testing equipment are of qualitative nature which is a major disadvantage compared to their destructive counterparts [74].
Especially, in the context of non-destructive testing of metals and their subsequent microstructure/microstructure evolution, two electromagnetic non-destructive testing techniques proven themselves useful over the past few years: Magnetic BHN [83,84] and Eddy current testing (ECT) [85,86]. Still, these two testing methods usually lead to qualitative estimates of the component's characteristics as they only detect changes in the underlying microstructure, and thus the entailing macroscopical material properties. Yet, this is oftentimes not enough for a quantitative process or component optimization, as materials characteristics such as strength, hardness, induced plasticity or residual stress state are properties that are of detrimental importance for the designing engineer.
However, BHN and ECT both have a high potential for quantitative estimation on materials properties such as stress state and hardness through correlation, as especially stress state, strength, hardness and plasticity are closely related to the strain hardening behavior respectively general changes in the microstructure. Thus, the following two sections will shed light on the working principles of magnetic BHN and ECT.

#### *2.3.3.1 Magnetic Barkhausen noise*

In first proximity, the hysteresis curve, see Figure 2-3 and Figure 2-4, appears as a continuous curve, however, Barkhausen discovered that the remagnetization really occurs in the form of small jumps, see Figure 2-9 [47,87].

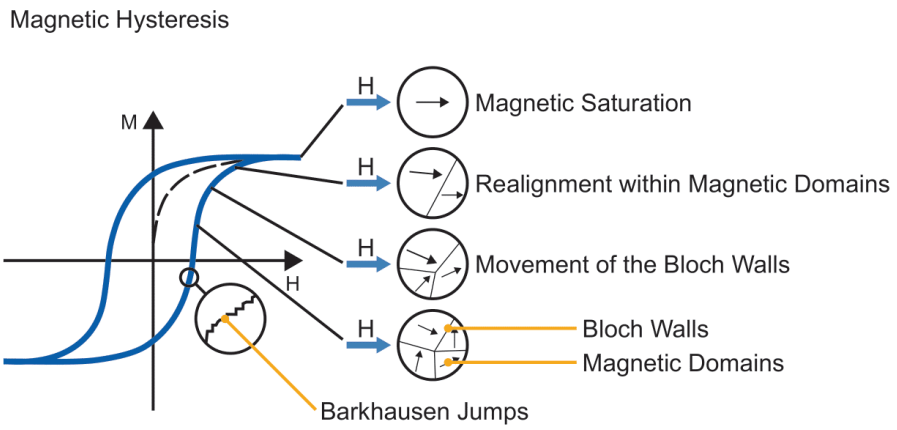


*Figure 2-9: Magnetic hysteresis curve characterized by occurring magnetic phenomena adapted from [88].*

The jumps occur due to the displacement of so-called domain walls, as they interact with microstructural defects leading to a discontinuous change of the magnetization. Steels with a cubic crystalline structure display three axes. These three axes are called easy axes within which the magnetic moments of the atoms are most probable to orient themselves along. When no magnetic field is applied, the domains align themselves along one of the three easy axes, so that the magnetic flux in the material closes, thus minimizing the magnetostatic energy. Domain walls can be separated into categories according to their orientation with respect to their neighbors. There are 180 °, which are usually located in the center of the material's crystals and 90 ° domains, that are mostly located towards the grain boundaries. However, this structure changes when a magnetic field is applied [87].

Whenever a magnetic field is applied, the domains close to the direction of the applied field grow at the expense of those directed differently than the field. This growth of the domains is due to the displacement of the domain walls. It must be noted, that BHN only occurs when a sudden variation in magnetization occurs. This sudden variation happens due to the hindering interaction of the domain walls with so-called pinning sites. Pinning sites in this context are mostly lattice defects, such as dislocations, vacancies, or inclusions [47,87,89].

As polycrystalline ferromagnetic materials such as steels still make up one of the most important materials in industrial products and their mechanical properties such as residual stresses are dictated by their microstructure, the non-destructive materials characterization through BHN analysis is close at hand. Especially as literature suggests that BHN is especially suitable for residual stress determination, which are among the most important mechanical properties in tubes [90–92]. Major advantages of BHN as a measurement equipment include its sensitivity to a manifold of microstructure occurrences, quick and easy handling during measurement, and its suitability for in-line inspection. However, this is countered by disadvantages such as extensive calibration

requirements and its application being limited to ferromagnetic materials. Currently used BHN measurement equipment include, but are not limited to the Rollscan-BHN measurement equipment from Stresstech [93], 3MA-II sensor technology developed at Fraunhofer Institute for Nondestructive Testing [94] as well as the QASS µmagnetic equipment developed by QASS [95], where this work uses the latter.

#### *2.3.3.2 Eddy Current*

Another commonly used non-destructive measurement technique that is very susceptible to a change in microstructure is so-called ECT.

During ECT, a coil generates a fluctuating magnetic field. When a conductive material is exposed to this magnetic field, eddy currents are induced within the material, circulating in closed loops. These eddy currents create a secondary electromagnetic field that opposes the primary electromagnetic field produced by the coil, resulting in detectable alterations in the coil's electromagnetic field. If the material being tested contains structural irregularities at the microscale, these disruptions affect the flow of eddy currents, consequently impacting the coil's electromagnetic field [74,77,78,96,97].

ECT works on any kind of conducting material (predominantly done on metals however), which gives an advantage compared to BHN analysis which is limited to ferromagnetic materials. It finds its application in detection of inhomogeneities close to the specimen’s surface. Especially in quality control of metal structures with regard to defects, such as cracks, corrosion, scratcher or heat affected zones and metal sorting [97]. A major drawback of this type of test is that in ferromagnetic materials, but also in non-ferromagnetic materials, the analyses can only be carried out close to the surface. As a general rule penetration depth of the measurement is no deeper than increments of an inch. Additionally, one of the major advantages of ECT, the susception to a variety of microstructural phenomena is also its largest disadvantage, which makes the monitoring of one parameter of interest rather difficult [74,77,78,96,98].

## 2.4 Soft sensors

Physical sensors are defined as devices that respond to a physical occurrence and thus resulting stimulation in converting it into a signal, often times of electrical nature [99].

A soft sensor, however, is a sensor that does not measure anything physically but rather relies on physical, sensor measurements in combination with mathematical modelling of processes and parameters of interest that then allows the estimation of variables of interest. As in mechanical and industrial engineering the production tolerances become ever so strict and production increasingly automatized, soft sensors have been gaining in relevance due to their great design and placement freedom [100]. They find their application in all kinds of disciplines, in quality control [101,102], the energy sector for district heating systems [103], even wastewater treatment [23,104] but also in metal forming processes [105,106].

Generally speaking, soft sensor modelling can be separated into model-driven and data-driven techniques. Model-driven soft sensors, also known as white box models, typically rely on the inherent physical and/or chemical framework of the process, indicating a comprehensive understanding of the process. A model-driven soft sensor is e.g. estimating the solidification behavior during casting based on heat transfer and solidification models [9–11]. However, in scenarios where the prior knowledge of the process or system is insufficient, or the modelling is overly complex, data-driven soft sensors, also referred to as black box models, may be more suitable, as they rely solely on empirical observations of the system. An example for a data-driven soft sensor poses battery health estimation in electric vehicles based on voltage, current and temperature data. Between these two extremes, various combinations can be chosen to leverage their respective advantages.

Usually, the design of soft sensors encompasses three main stages: (1) gathering data and information, (2) designing the sensor, and (3) implementing it [9–11].

Thus, it is imperative to establish the quality of the data, ensuring that sensor and actuator placement minimizes the impact of missing data or outliers. Subsequently, the appropriate model type must be determined, considering factors such as the system's nature, including parameters like linearity, dynamics, and the intelligence level of the model. Finally, the chosen model must be put into practice.

A soft sensor for freeform bending has already been introduced. Wu et al. [107] introduce an Extended Kalman Filter (EKF) for the trajectory prediction of three-dimensional forming of tubes. They, hence, introduce a soft sensor focusing on the geometry of the bent tubes, however, also neglecting mechanical properties such as strength and residual stress state [107].

As the introduced soft sensor in this thesis relies on state space modelling commonly used in control engineering, the following section introduces methodologies for system description posing the heart of a soft sensor.

### 2.4.1 System Description

An essential part for soft sensor design lies in detecting how the quantities of interest are actually related to the measurands that may be taken while the system is running as well as the modelling thereof. A system in this context refers to the machine at hand, including all sensors and actuators that can influence the properties of interest. As this thesis relies on a soft sensor based on state-space modelling (which is a modelling approach often used in control engineering), a quick introduction into basics of control engineering regarding system description and modelling is given in this chapter.

System natures are usually characterized with regard to three categories – whether their behavior is dynamic or static; linear or non-linear and whether they are time-variant or time-invariant [108].

Dynamic behavior describes the progression of the system output over time given the system input variable, while static behavior describes the dependence of the resulting

static end values of the system output variable on stationary values of the input variable (most systems occurring in nature are of dynamic character). Dynamic behavior can be either modelled for continuous-time, meaning the variables (state, input and output) evolve continuously with respect to time, or discrete-time systems, meaning the variables evolve in discrete time steps or intervals of time. Whether a system is linear or non-linear is closely tied to the law of superposition; meaning that if the systems output cannot be described by a linear operator applied to the input, non-linearity is given (non-linearity is also the common nature of occurring systems). Furthermore, if the system parameters are not constant, but change as a function of time, the system is called time variant (time variant and time invariant systems occur equally often) [108,109].

Dependent upon the underlying systems nature, the system can be described by all kinds of models that are largely reliant on the formulation of differential equations that model the development of parameters of interest. The choice of model depends on factors such as the complexity of the system, the available data, the parameters to be controlled as well as the analysis and design techniques to be employed. As the freeform bending process with movable die depicts a dynamic system, this section will introduce modelling tools that are commonly used in control engineering for dynamic systems. They include but are not limited to transfer function models, differential equations, empirical models or state-space models [110–114].

Transfer function models are widely used, especially in classical control theory. They represent the relationship between input and output of a system in the frequency domain, which is especially lucrative to understand system stability, transient response as well as frequency response characteristics. They provide a concise representation of the relationship between the input and output of a linear time-invariant system. Their simplicity and effectiveness in representing time-invariant systems make them a common choice in many engineering applications [110,111].

Differential equations directly describe the dynamics of a system in terms of derivatives of the system’s variables with respect to time. Depending on the complexity of the inspected system, these equations may range from simple first-order linear differential equations to high-order nonlinear equations. They are used to model mechanical systems, electrical circuits or chemical processes, just to name a few. While differential equations offer a powerful tool for modelling and analyzing dynamic systems, they also present challenges with regard to complexity, parameter sensitivity, numerical stability as well as computational cost [113,114].

Empirical models are particularly useful when the investigated system is especially complex or the underlying dynamics unknown. They usually rely on data-driven techniques such as machine learning to approximate system’s behavior without requiring explicit knowledge of the underlying physical principles. They provide flexibility and

adaptability, however, can be prone to overfitting and limited interpretability (as no underlying physical mechanism explaining system's behavior is given) [112].
State-space models compared to, i.e., transfer functions allow a more comprehensive representation of system's internal dynamics, as they allow the modelling of complex systems with multiple inputs, outputs as well as internal states. They can model nonlinear, time-varying, and multivariable systems allowing high flexibility as well as efficiency in modelling, which makes them a very commonly used approach. The state of a dynamic system in this context is the minimum necessary set of physical variables, referred to as state variables, so that, assuming comprehensive knowledge of these variables at time $t = t_0$, together with the knowledge of the input variable for $t \geq t_0$, the dynamic behavior of this system may be determined for any time $t \geq t_0$. State variables are thus the minimum necessary set of physical variables to determine the dynamic state of a physical system [110,115].
A characteristic feature of state-space modelling is the utilization of two key formulas: Formula 2-22 a first order differential equation called state equation and Formula 2-23 an output equation relating the output to its states [115]. The following formulation is for time-discrete systems, as all introduced models within this work are time-discrete.

$$x_{k+1} = A\ x_k + B\ u_k \qquad \textit{Formula 2-22}$$

Where:
$x_k$ is the state vector representing the system's internal states at time $k$.
$x_{k+1}$ is the the state vector ahead at time $k + 1$.
$A$ is the state transition matrix describing the system's internal dynamics.
$B$ is the input matrix relating the inputs to the state variables.
$u_k$ is the input vector representing external inputs influencing the system (actuators).

$$y_k = C\ x_k + D\ u_k \qquad \textit{Formula 2-23}$$

Where:
$y_k$ is the output vectors, representing the system's observed outputs at time k.
$C$ is the output matrix relating the states to the outputs.
$D$ is a matrix relation the inputs directly to the outputs.

# 3 Methodological Approach

Nowadays, freeform bending with movable die offers a process that allows the bending of complex geometries, without changing the bending tool, making it cost as well as time efficient. However, whenever customers communicate, they require a component of special geometry bent via freeform bending, (1) the DOF at hand for the said dimensions need to be established empirically usually resulting in extensive trial-error process and (2) the set mechanical properties in the component (oftentimes tubes) are neglected entirely. However, especially in bent steel tubes the mechanical properties already fluctuate significantly across the tubes cross-section. If then a bending operation is conducted on those tubes, the fluctuation just enhances further. Varying mechanical properties such as the residual stress state can render the entire component unusable, if distributed unfavorably.

Hence, the superordinate goal of this thesis is to establish a soft sensor for the freeform bending process with movable die that estimates relevant mechanical properties within the steel tubes. This soft sensor in turn is to serve as a basis for a closed-loop property control of the process, that may manipulate the actuators/DOF at hand such that the desired mechanical properties may be set while simultaneously meeting the required dimensions. Relevant mechanical properties within steel tubes in this context are especially strength, ductility as well as axial and hoop residual stresses, as they determine not only the application of the workpiece but also significantly influence postprocessing. Yet, these mechanical properties cannot be measured directly during the process, but rather need to be derived or determined in downstream, extensive and oftentimes destructive analyses, that render the component unusable, which in turn defies the purpose of the process.

The following Chapters 5, 6 and 7, thus, explain how such a soft sensor that may derive mechanical processes of interest may be established. Chapter 6 is a previously published, peer-reviewed article that may also be found under DOI: 10.3390/ma14164549. Figure 3-1 shows depicts the methodology derived in this work that enables the implementation of a soft sensor for freeform bending with movable die.

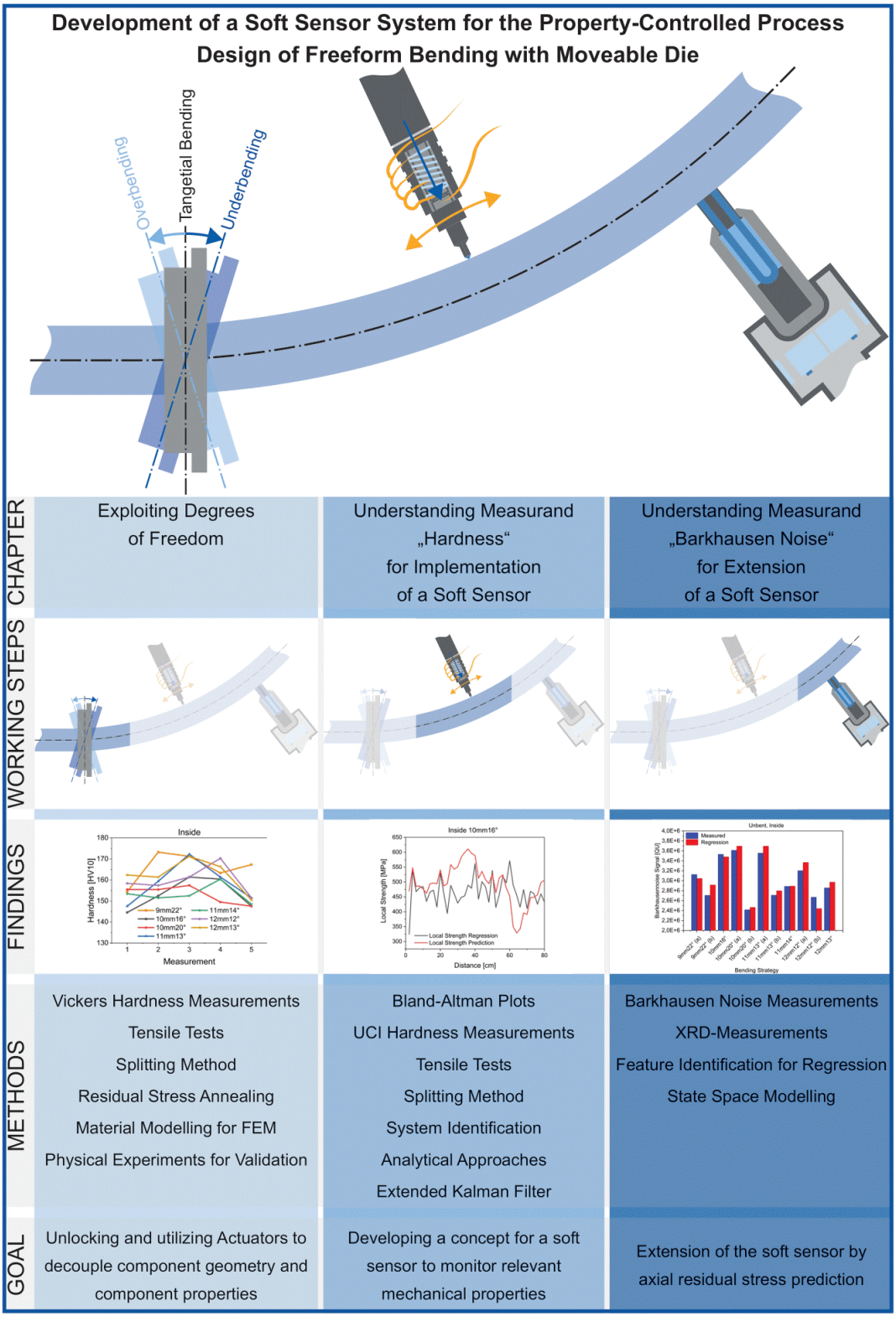


*Figure 3-1: Depiction of the Methodological Approach regarding the development of a soft sensor for freeform bending with movable die.*

**Decoupling of Dimensional Accuracy and Mechanical Properties.** The ultimate desire, regarding the freeform bending process with movable die, is to communicate a concrete geometry of a component with a defined set of mechanical properties that need to be met. However, in most forming processes, freeform bending included, to

set a certain geometry an empirically derived set of DOF will be used to set the desired geometry; whereby the mechanical properties are a concomitant characteristic and are furthermore firmly bound to one geometry. Thus, an initial step is to decouple the evolution of dimensional accuracy/geometry evolution of the component from the set mechanical properties within the steel tubes at hand. Hence, Chapter 5 will closely investigate DOF that the freeform bending with movable die provides as well as their influence on the evolution of geometry and mechanical properties by means of physical experiments. Different DOF are established that can be used to bend a defined, set geometry while also influencing the mechanical properties with varying degrees. By and large, this chapter establishes that the superposition of stresses is the most efficient methodology for freeform bending with movable die and so-called over- and underbending is brought into existence.

Furthermore, the entire tube is modelled numerically within this chapter, meaning that both the base material and the weld seam are modelled in the Computer-Aided Engineering (CAE) model of the bending process, which may be used to derive a larger data set for the soft sensor ultimately.

Additionally, it proposes the relationship between hardness and residual hoop stresses in examining residual stress annealing with regard to hardness developments. Based on these results, further analyses regarding the resulting mechanical properties can be performed to lay the foundation for the proposed soft sensor.

**A System Identification and Implementation of a Soft Sensor for Freeform Bending.** After successfully establishing the superposition of induced stresses within the bent steel tubes via over- and underbending, this chapter proposes a soft sensor. To do so, a suitable means of measurement needs to be identified based on which a soft sensor may be reliant. Thus, UCI hardness measurement equipment is investigated regarding its measurement suitability for measuring hardness on the over- and underbent tubes. Furthermore, the relationship between hardness and the mechanical characteristics of interest namely local strength, induced plasticity and residual hoop stresses is analyzed. To establish the relationship between local strength, induced plasticity and hardness, tensile tests are conducted based upon which, a simulation model is derived to determine the local strength at hand. Additionally, a correlation between residual hoop stresses and hardness is investigated based on the previously conducted residual stress annealing and hardness mappings. These results are then used to implement a so-called EKF, that allows the inline determination of strength, induced plasticity and residual hoop stresses based on UCI hardness measurements.

**Extension of Soft Sensor by Residual Stress predictions based on Barkhausen noise measurement.** In bent steel tubes, especially the residual axial stresses are of interest as an unfavorable distribution thereof, can lead to the complex bent geometry being distorted again in downstream welding or cutting processes. Thus, again rendering the workpiece unfit for service and application. Literature proposes that a form of

metrology that is susceptible to a redistribution in residual stress state is so-called BHN analysis [90–92]. However, as BHN analysis is extraordinarily susceptible to all kinds of microstructural phenomena, a mere investigation of the signal intensity is insufficient for a qualitatively high correlation to residual axial stresses. Yet, literature also suggests that the magnetic hysteresis loop that is passed through during the magnetization is reshaped by residual stresses, which in turn may be observed in the measured signal [90].

Hence, this Chapter introduces a novel methodology to evaluate BHN analysis signal regarding its symmetry. Residual axial stress measurements based on X-ray diffraction (XRD) are conducted to determine the residual axial stresses in the over- and underbent tubes. These are then correlated to the BHN measurements, which can be taken during the running process, and implemented into state space model, such that inline estimation and prediction of the residual axial stresses can be performed.

All in all, this thesis introduces DOF within the freeform bending machine that may be used to influence the mechanical properties of the steel tubes decoupled from the dimensions of the workpiece. Based on this insight, a softsensor based on UCI hardness and BHN measurements is proposed that now allows the inline derivation of local strength, induced plasticity, axial as well as hoop residual stresses. Thus, laying the basis for a closed-loop property control of the process which reduces resources, is significantly more time efficient and may avoid unnecessary scrap metal production.

# 4 Material Selection

The investigated material within this work is a P235 TR1. It is a low-alloyed, ferromagnetic steel grade, that according to production standards, is designed for pressure purposes and does not have a defined aluminum alloying limit or minimum requirement for impact energy [116,117]. The chemical composition in weight percent of the material determined by optical emission spectroscopy can be taken from Table 4-1.

*Table 4-1: Chemical composition in weight percent of P235 TR1 determined through optical emission spectroscopy.*

| Element | C | Mn | Al | Si | Cr | P | S | Ni | Mo | Cu |
|---|---|---|---|---|---|---|---|---|---|---|
| P235 TR1 | 0,037 | 0,11 | 0,025 | 0,027 | 0,041 | 0,0048 | 0,0016 | 0,081 | 0,011 | 0,244 |

As seen in Figure 4-1 (1) and (2), the base material as well as the heat affected zone (HAZ) is ferritic with some perlite towards the grain boundaries. The HAZ yet exhibits a coarser grain size. The weld metal in Figure 4-1 (3) shows a bainitic microstructure. The material itself is investigated in the form of circular steel tubes that are produced according to [116,117]. The dimensions of the circular tubes are as follows: outer diameter of the tubes is 42.4 ± 0.5 mm, thickness is 2.6 ± 0.3 mm and length is 800 ± 2 mm. The circular tubes are welded longitudinally with an even finish both on the inner and outer surfaces of the tubes, as is required for freeform bending with movable die.

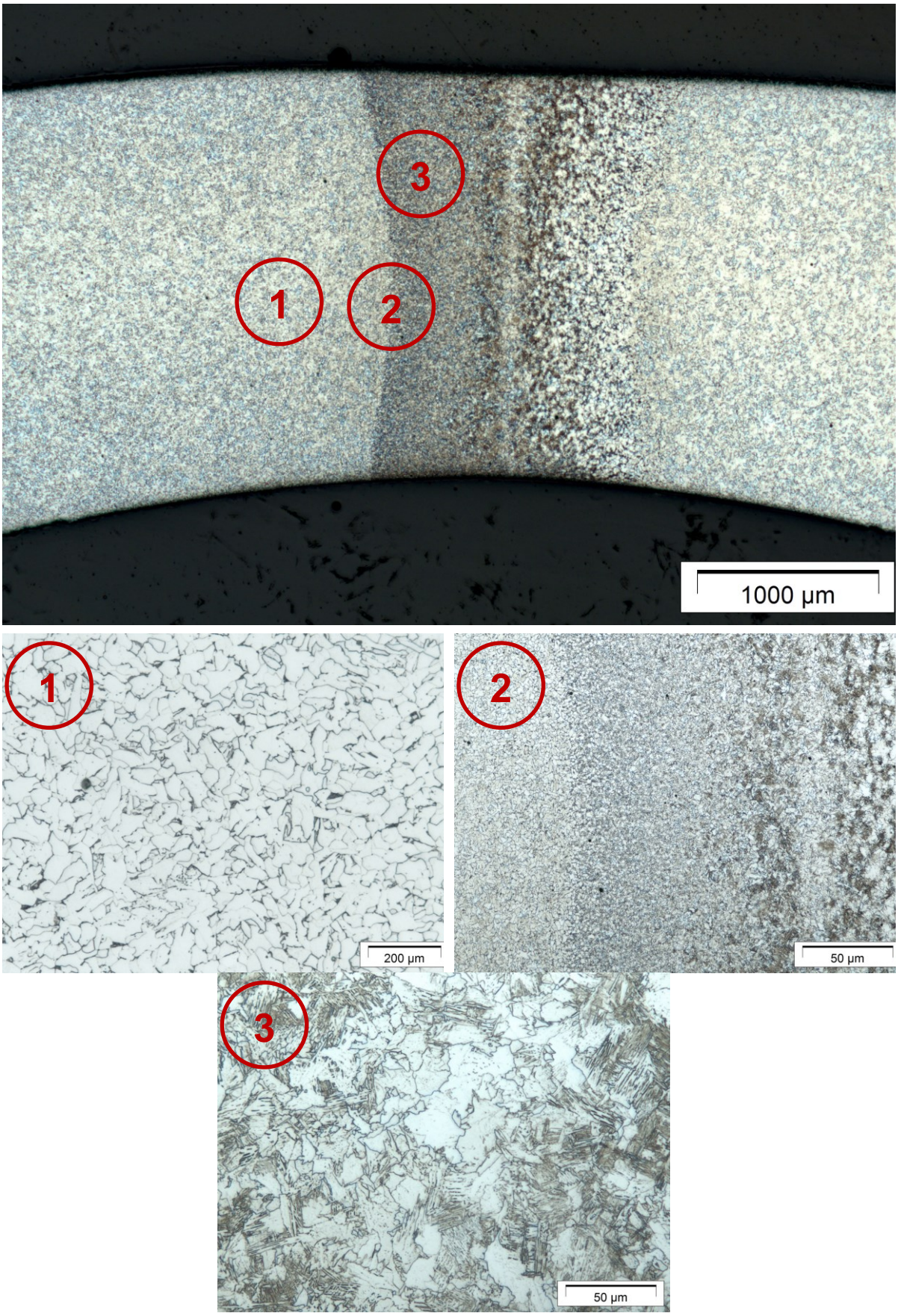


*Figure 4-1: Light-microscopical image of the P235 TR1 microstructure; Cross-section P235TR1 Magnification 25x; (1) Base material (500x); (2) HAZ (500x) and (3) Weld metal (500x).*

# 5 Decoupling of Dimensional Accuracy and Mechanical Properties

Within the last few years, the efforts on monitoring metal forming processes has increased significantly [118–122]. This is due to the fact, that in the context of sustainability as well as resource efficiency, product tolerances as well as production standards get increasingly stricter. This entails that nowadays oftentimes open-loop controlled forming processes rather need to be closed-loop controlled [118,123]. Forming processes nowadays already incorporate closed-loop controls for the inline adjustment of the process, however, the control of components product properties are largely reliant upon open-loop controls [1]. This particularly means, that the microstructure evolution, meaning for example texture or dislocation density, that dictates the product properties such as strength or residual stresses of the component is disregarded entirely.
However, this causes various impairments. A forming process neglecting property fluctuations within the components, will ultimately lead to time intensive and costly post-production of the workpiece that arise due to the required mechanical properties not being met; sometimes even to scrapping of the component altogether [2,3]. Thus, implementing closed-loop controls into the process that incorporate feedback on the microstructure evolution/mechanical properties, will make process design to be more efficient with regard to resources, time as well as costs and will ultimately lead to a more sustainable technology.
Albeit this venture harbors several challenges. First and foremost, actuators in the processes at hand need to be examined and studied regarding their influence on the mechanical properties. Hence, a systematic understanding regarding the interplay of mechanical properties and geometrical evolution of the workpiece must be established. This is especially challenging, as a defined geometry of a workpiece is usually closely tied to a specific set of mechanical properties. Thus, this chapter investigates if and how the evolution of the mechanical properties may be decoupled from the evolution of geometry of the bent steel tubes during freeform bending with movable die. For this purpose, different DOF in the machine, namely the mandrel position, feed rate as well as non-tangential bending, are considered and assessed regarding their influence on the mechanical property hardness.
Furthermore, this chapter introduces a numerical model for the material characteristics of base material and weld seam to create a larger database and to be able to simulatively assess critical variables for the closed-loop control.
Last but not least, initial investigations regarding the relationship between residual stresses and UCI hardness are conducted for further use in Chapter 6.

## 5.1 Degrees of Freedom for Decoupling

Mechanical properties of a component determine its performance during application. Thus, it is detrimental to know the mechanical properties profile within the workpiece

at hand, as furthermore, to be able to influence them according to the required profile. During freeform bending with movable die, the semi-finished product undergoes plastic deformation, leading to a change in shape and mechanical characteristics. To fully understand the evolution of mechanical properties during the process, the microstructure evolution needs to be understood as it determined the final mechanical properties [29]. This is especially relevant for strain hardening (as addressed in Chapter 2.1.1), which occurs mainly due to the increasing in dislocation density. Microstructure parameters such as the density and distribution of dislocations, grain shapes and their orientation, damage in the material and phase distribution all account for the final mechanical properties such as the strength, stress distribution, hardness and so on. Hence, to pinpointedly influence said mechanical properties, the underlying, occurring microstructure evolution must be manipulated. As addressed in Chapter 2.1.1, parameters that can influence the microstructure evolution are namely, the temperature, strain rate as well as the state of stress.

The forming temperatures primary influence is in the yield strength of the to be formed material. As a general rule, it can be said, that with an increase in forming temperature, the yield strength decreases. For materials with a body centered cubic (bcc) structure, the forming temperature does not have significant influence on the strain hardening behavior. However, in face centered cubic (fcc) structures, the strain hardening behavior is influenced by the forming temperature as the dislocation movement is impeded by a decreasing temperature [26,29]. However, investigations [64] have shown that the forming temperature should not be implemented as a DOF in the freeform bending process with movable die. A heating coil would need to be positioned in front of the guider of the tube. Whereas this entails significant heat loss until the bending occurs, and an accurate setting of the forming temperature is not feasible. The works of Maier [64] investigated a partial heating system within the machine, however, due to the one sided heating of the tubes, substantial distortion is caused. Equally as for the heating coil, the partial heating system cannot be placed in such a way, that the heating occurs during the bending, again causing significant heat dissipation. Thus, the DOF temperature is excluded from further investigations.

Generally speaking, with an increase in strain rate, both the tensile and yield strength of a material increases, whereas the uniform elongation decreases. This relationship applies up to strain rates ≈ $10^{-2}$ 1/s. Whenever this critical value is surpassed, the heat exchange between the component and the surrounding is insufficient, which in turn leads to a heating of the component causing the yield and tensile strength to decrease [26,29].

In addition, when the material undergoes forming, the material's state of stress changes. Hydrostatic stresses especially influence damage evolution while plasticity is unaffected. However, they do lead to an expansion of the crystal lattice, thus, favoring diffusion [124].

This demonstrates that macroscopic properties are defined by the microscopic occurrences that are in turn strongly associated with external factors. Hence, the interplay of process, the concomitant DOF and resulting microstructure, thus product properties need to be fully understood to ultimately implement closed-loop property-controls of the processes.

Recent literatures' focus lay on the systematic understanding of microstructure evolution during processes. Just to name a few, Reimann et al. [125] use machine learning algorithms to numerically model the mechanical response of varying microstructures with regard to their loading based on representative volume elements and crystal plasticity modelling. The authors in [126] analyze the microstructure evolution of a QP980 steel during the Quenching and Partitioning process. Yang et al. [127] introduce a model allowing the simulation of the microstructure evolution during induction heating for austenitization of steels based on cellular automata and Vajragupta et al. [128] introduce a micromechanical model for the mechanical behavior of steel grade DP600 while undergoing sheet metal forming.

Yet, studies that use such approaches to systematically influence the interaction between macroscopic product properties, namely geometrical evolution and mechanical properties for implementation of closed-loop property-control of the processes, are scarce to non-existent. Hence, this chapter lays the basis for closed-loop property control of the freeform bending process, in conducting investigations regarding the DOF in the machine, namely mandrel position, feed rate as well as the superposition of stresses. HV 10 Vickers hardness measurement serve as a measurement method to investigate whether the mechanical properties can be successfully decoupled from the geometrical evolution of the steel tubes.

### 5.1.1 Mandrel position

One DOF that could have the potential for decoupling the tubes geometrical evolution from the mechanical properties poses the position of the mandrel during the bending. Results from [69] show that the mandrel position has a high influence on the geometry of components made from aluminum. Hence, the influences of the mandrel position were investigated regarding influence on the hardness on the tubes, while keeping the geometry constant.

The chosen mandrel positions varied from -10 mm to +15 mm in distances of 5 mm from the origin position. At the origin position, the end of the mandrel is at the same height as the center of rotation of the bending die. 0 mm, the origin position, was not investigated separately as this is the default position in general bending.

The HV 10 hardness measurements were taken on the polished tube surfaces along the inside, meaning where compression of the tube occurs, and outside, where the tube is elongated, of the tubes, along the guidelines of DIN EN 6507-1. During Vickers hardness tests, an equilateral diamond pyramid with an opening angle (between the

side faces of the pyramids) of 136° is pressed into the workpiece under a defined testing force. This leaves an indentation on the materials surface, where the length of the indentation diagonals is then measured under a microscope. The ratio of the test force in Newton with regard to the indentation surface multiplied by the factor 0.1891 gives the Vickers hardness. As the measurements are taken on round tubes, the measurements are corrected according to DIN EN 6507-1 [129].

All measurements were taken in the section of fully deflected bending die, where the induced plasticity is largest. Consideration of these sections is sufficient as the most critical mechanical properties are also associated with a high degree of deformation, $\varphi$. The measurements were taken in 2 cm distances. The results of the hardness measurements can be seen in Figure 5-1.

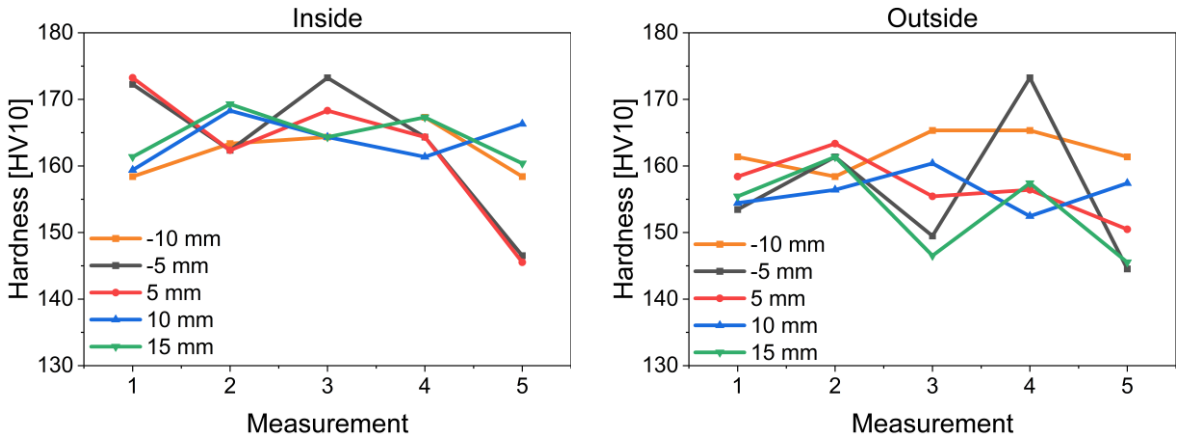


*Figure 5-1: HV 10 hardness measurements on the inside (left) and outside (right) of the tubes with varying mandrel positions. Measurements taken in area of fully deflected die.*

It can be seen that the hardness development of regardless the position of the mandrel does not vary significantly. Especially, the development of hardness on the inside of the tubes is very consistent. Hardness on the outside of the tubes scatters a bit more than on the inside.

These results, however, indicate that the mandrel position is not a suitable DOF to influence the mechanical properties detached from the geometry for the material steel. This DOF is thus excluded as an influencing actuator.

### 5.1.2 Feed rate

Another possible DOF for decoupling the geometrical development from the mechanical property development during freeform bending poses the feed rate within the process. This is because the feed rate, thus strain rate, can have a significant influence on both yield and tensile strength in bcc-materials, as is the case for P235 TR1. Possible feed rates for the machine at hand lie between 1 mm/s and 200 mm/s. For this investigation feed rates from 75 mm/s-200 mm/s increased in increments of 25 mm/s

were studied. Again, Vickers hardness measurements (HV 10) were taken on the surface of the tubes. The methodology is analogous to the previous Chapter 5.1.1. The hardness development along the tube surface can be seen in the following Figure 5-2.

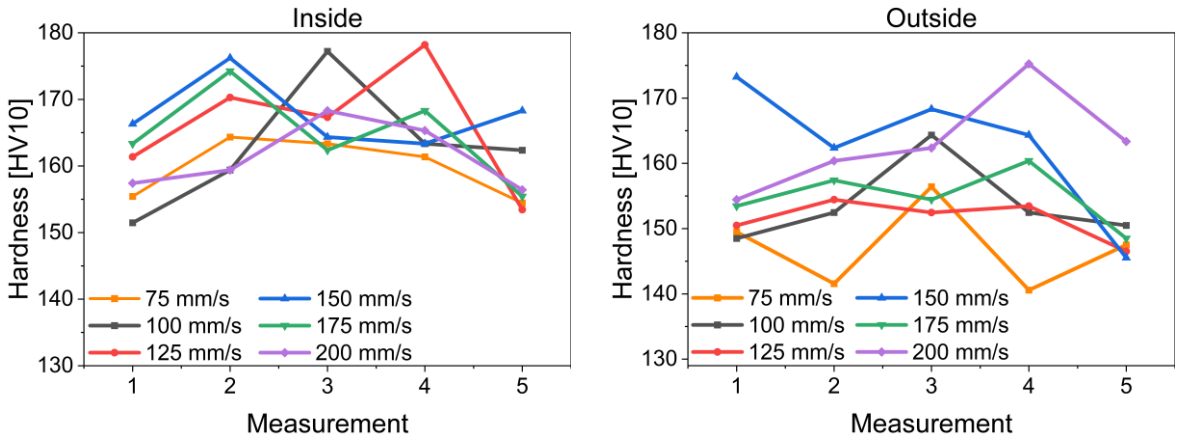


*Figure 5-2: HV 10 hardness development on the inside (left) and outside (right) of the tubes for varying feed rates. Measurements taken in area of fully deflected die.*

Again, for the feed rate the hardness does not scatter significantly among the various rates. Yet again, especially the hardness on the insight of the tubes develops very consistently. The outside values do scatter more pronounced than before. However, these results still suggest that the feed rate is again not an actuator suited to decouple the development of mechanical properties from the geometrical development. It must be noted that the maximum feed rate of 200 mm/s is not a rate high enough to heat the component such that influences on yield or tensile strength are to be expected.

### 5.1.3 Superposition of stresses

A last, promising DOF that can lead to a decoupling of the evolution of the geometry and mechanical properties within the investigated steel tubes poses the superposition of stresses through non-tangential bending. Non-tangential bending in this context means that during the bending process, the bending dies' positioning is not tangential during maximum deflection. A schematic depiction of the non-tangential bending process can be seen in Figure 6-1. This means, instead of the usual tangential bending position of the bending die, the die is set to a certain rotation and deflection, leading to an over- or underbending of the steel tube. This over- and underbending is thus accompanied by a superposition of bending stress. Positions with higher rotations than in the tangential position are referred to as overbending, while smaller rotations are referred to as underbending. In utilizing different combinations in deflection or rotation of the bending die, the bending geometry in the end is the same, even though different DOF are used. The extent to which these DOF are enabled in the kinematics of the process is detailed in the works of Maier [64]. Based on this newly enabled over- and underbending of steel tubes, seven bending strategies are established that all lead to

the same radius/curvature of the final bending geometry. These are namely the bending strategies 9mm22°, 10mm16°, 10mm20°, 11mm13°, 11mm14°, 12mm12° and 12mm13°, whereby the denotation means, e.g. 9mm deflection and 22° rotation of the bending in the area of full deflection. The bending strategies 9mm22°, 10mm16° and 10mm20° are overbent, the remaining ones underbent. Again, in the manner of the previous two sections, HV 10 hardness measurements along the fully deflected area were taken to determine whether a superposition of stresses leads to varying mechanical properties, while the geometry is kept constant. The following Figure 5-3 shows the hardness development of the over- and underbent tubes.

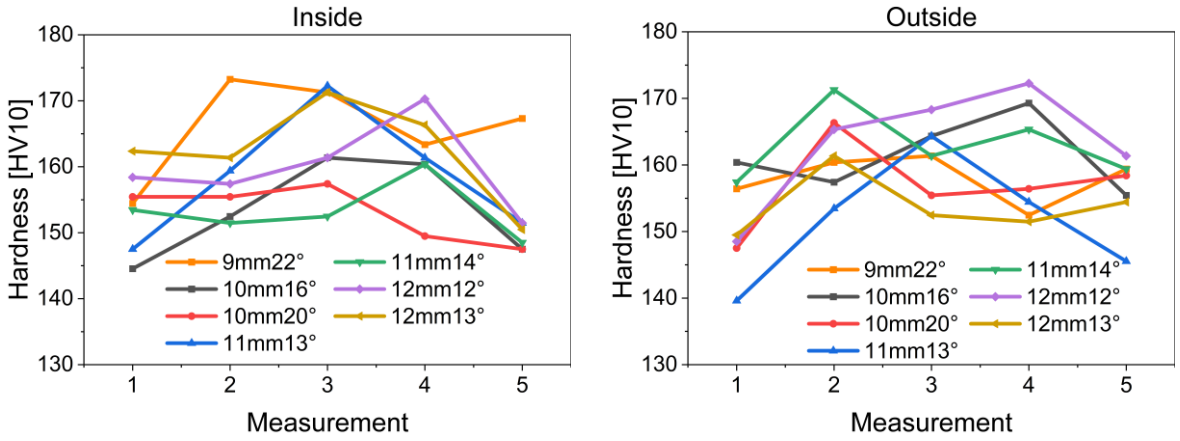


*Figure 5-3: HV 10 hardness development on the inside (left) and outside (right) of the tubes for over- and underbending. Measurements taken in area of fully deflected die.*

It can be seen that the distribution range of the hardness is especially for the inside of the tubes much more pronounced than before. Along the outside, the hardness also scatters significantly. As the hardness is closely related to both strength and residual stress state (the exact relationships being highlighted in the following Chapter 6) a pronounced scatter band indicates that both the material strength and residual stress state will also vary within these bending strategies. Further experiments, especially for residual axial stresses proving the successful decoupling will be provided in Chapter 7. Thus, new DOF are established that influence the mechanical properties of the bent tubes significantly while allowing a constant bending curvature. Hence, the superposition of stresses is now established as a decoupling strategy and the following Chapters will focus on tubes that are over- and underbent.

## 5.2 Numerical Modelling of Material Characteristics

For the numerical modelling of the material characteristics in finite element method (FEM) software Abaqus, tensile tests need to be conducted. Tensile tests allow the derivation of a flow curve, that is needed to model the plastic material behavior in Abaqus. Additionally, as explained in Chapter 2.1, tensile tests also provide insight on

the strain hardening behavior of the material undergoing plastic deformation. The tensile tests were conducted according to [130]. Testing conditions were at room temperature with a testing speed of 0.00025 1/s as to prevent any adiabatic heating of the testing samples. The tests were performed with a uniaxial tensile test machine of type Zwick/Roell Z4204. As tensile test specimens, miniature tensile test samples were chosen, that were taken from the steel tubes in the area of base material and the weld seam. In choosing miniature tensile testing samples, the effects of the curvature of the steel tubes may be minimized. Hence, enabling a tensile testing in uniaxial stress state. For the specimens taken from the weld seam, the reduced section lies right within the weld seam as the reduced section and weld seam are both 2 mm in width. Thus, the specimens include both the weld metal and HAZ and the weld seam is investigated as a whole.

To model both the base material and weld seam, the conducted tensile tests served as the basis for fitting of the flow curves. The Ludwik-Voce fitting was conducted according to Formula 2-17 using least squares method in order to find the optimal fit for a flow curve. The exact fitting parameters can be taken from the following Table 5-1.

*Table 5-1: Ludwik-voce fitting parameters for base material and weld seam.*

| Parameter | $\alpha_L$ | $b_L$ | $A_L$ | $n_L$ | $k_{0.V}$ | $Q_V$ | $\beta_V$ |
|---|---|---|---|---|---|---|---|
| Base material | 0.225 | 425 | 1200 | 0.7 | 420 | 65 | 62.92 |
| Weld seam | 0.25 | 470 | 1000 | 0.4 | 488.81 | 0.1 | 0.1 |

The following Figure 5-4 shows the conventional stress-strain curves of both the base material and the weld seam. The fitted flow curves were validated in simulating a tensile test using the mathematical fits. For the fit of the base material test sample number 4 was taken; for the fit of the weld seam test sample number 5 was used as both these samples show the average of all tests.

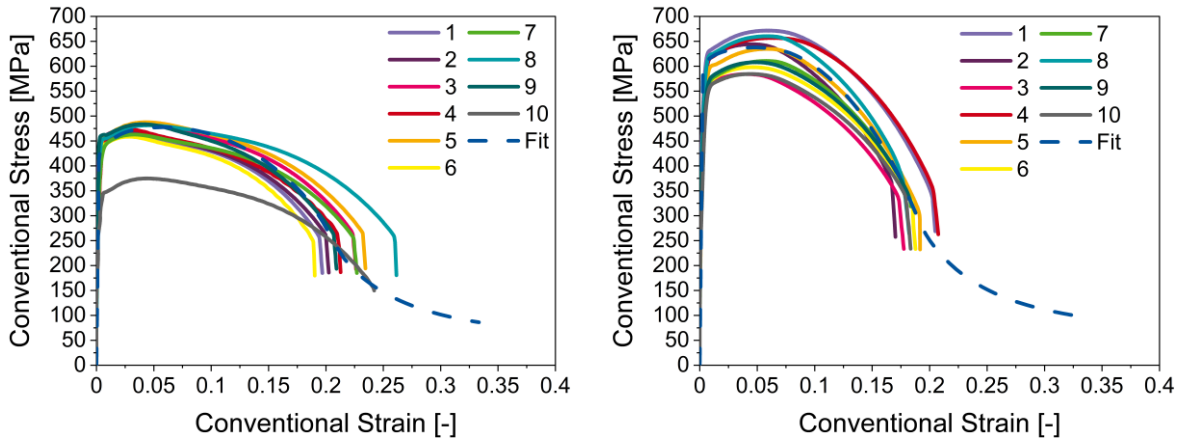


*Figure 5-4: Conventional stress-strain curves for the P235 TR1 base material (left) and weld seam (right).*

It can be observed that especially in the base material the results of the tensile tests scatter, which in turn highlights the need for a closed-loop property-control to be implemented into the freeform bending machine. Furthermore, uniform elongation is met earlier in the weld seam material than in the base material while simultaneously meeting higher tensile strength. Overall ductility in the weld material is also lower than that of the base material. This is expected as in the microstructure of the HAZ, see Figure 4-1 (2), shows that the microstructure is rather coarse compared to the base material see Figure 4-1 (1), which causes lower ductility and strength of the material. Hence, a separate modelling of the weld seam within the FEM model is necessary.
The FEM model of the bending process itself is based on the results of [73], which do not take the weld seam into account. This work extends the model by a weld seam, while simultaneously proposing the material models for P235TR1 base material. The proposed model consists of the bending die, guider and mandrel that are all modelled as rigid bodies. The tube itself is modelled using 3D deformable shell elements with element type S4R with five integration points across the tubes thickness. The element type S4R was selected as this modelling approach offers the most efficient calculation time (30 minutes using four cores). Different element types were also tested. The table below, Table 5-2, shows the element types with comparison to calculation time.

*Table 5-2: Element types used for modelling of the tube and their respective calculation time running on four cores*

| Element type | C3D8R | C3D8 | C3D8R_3 | S4 | SC8R |
|---|---|---|---|---|---|
| Calculation time in h | 8 | 8 | 20 | 2 | 5 |

For implementation of the weld seam, a partition of 2 mm in width is defined, where the flow curve of the weld seam material is implemented. The mandrel is positioned within the tube in such a way that the tube is supported during the bending process from within as to avoid folds as well as buckling. The parts of the mandrel are coupled using pins in a multi-point constraint type. To push the tube forwards and through the guider and bending die, a displacement boundary condition is defined at the end surface of the tube. Additional boundary conditions both for rotation and displacement are moving the bending die at the center of rotation during the simulation. Amplitudes are used to define the exact bending rotations and deflections. While the bending process is running, the position of the mandrel as well as the guider are fixed in place. For the whole model a friction coefficient of 0.1 is set. The close up of the set-up of the model can be seen in the figure below, Figure 5-5. All relevant parts of the model are marked accordingly.

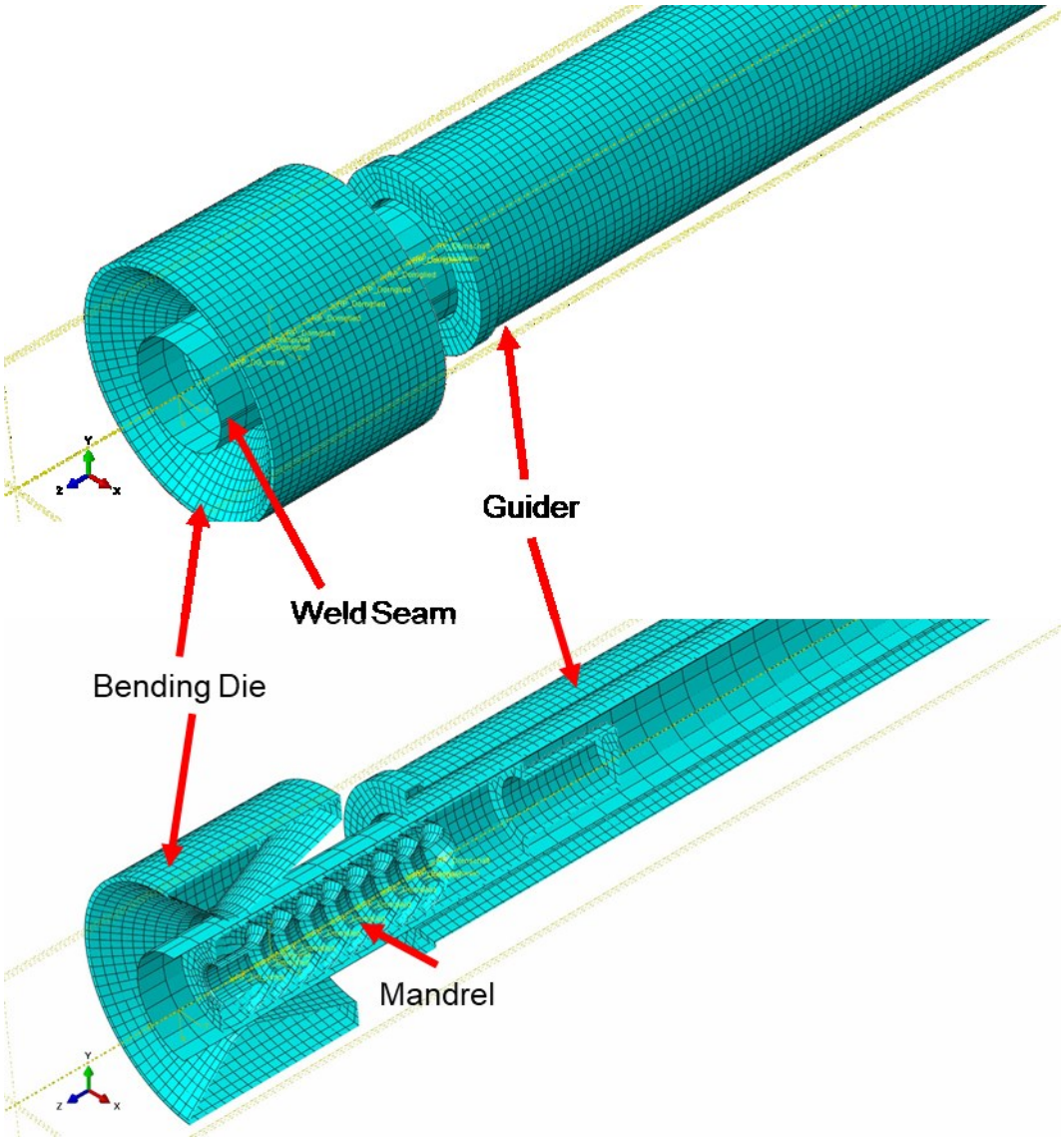


*Figure 5-5: Assembly of the FEM model implementing the weld seam. Above: Whole model; Below: Cross-Section of the model to visualize the mandrel.*

All simulations were performed using von Mises (J2) plasticity theory. As there is no possibility to take strength values directly off the bent tubes, an alternative validation parameter needs to be determined. Physical measurements that can be taken on the bent tubes are (UCI ) hardness measurements. However, Abaqus does not have a predefined output variable that describes hardness. Yet, hardness and strength are closely related one another. The exact relationship between hardness and strength is investigated in Chapter 6. It can thus be assumed that, up to necking, multiplying hardness by 2.88 results in the Mises stress and can then be used for validation of the Abaqus model. The hardness on the steel tubes was determined using a UCI hardness measurement equipment. The method thereof is described in detail in Chapter 6.2.2. To confirm the stability of UCI measurements and thus to demonstrate that UCI hardness measurements converted to von Mises stress/strength are a suitable approach to validate the Abaqus model, cross-sections were taken from the unbent tubes. The UCI hardness measurements taken on the cross-sections were then compared to the

hardness measurements taken on the surface of the bent tubes. If the hardness measurements are in concordance with each other, surface hardness measurements are suited for the use of validation. Thus, cross-sections taken from unbent material were embedded in epoxy resin to then be closely investigated regarding their UCI hardness. The measurements were taken using a customized guider, with 0.3 mm distance between them. The following Figure 5-6 shows UCI hardness measurements taken on the tube surface as well as on the tube cross-section.

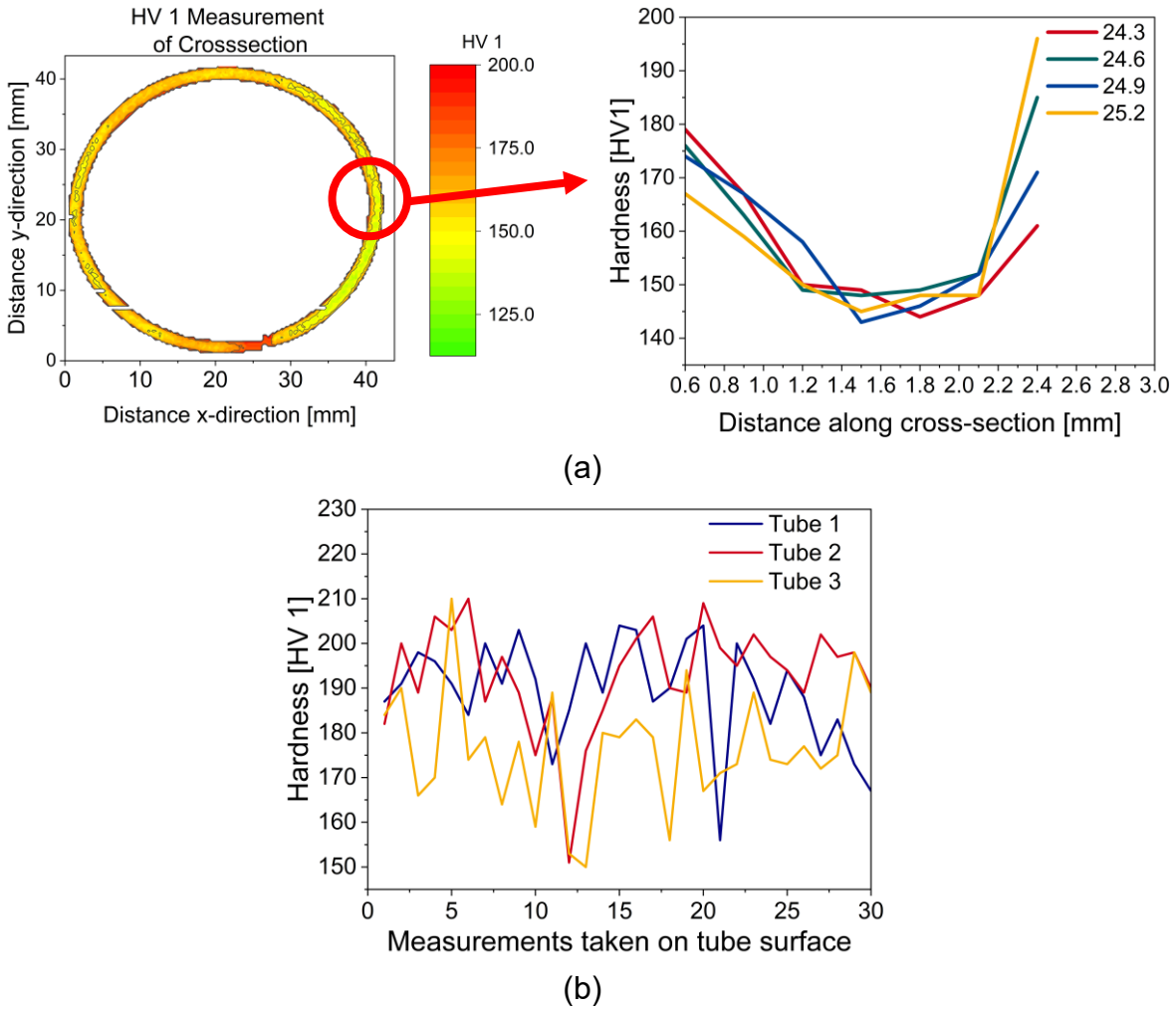


*Figure 5-6: (a) UCI hardness along cross-section (b) UCI hardness along tube surface*

It can be observed that the measurements taken on the surface have a stronger fluctuation. As these measurements were taken by hand, a stronger scatter is to be expected. However, the measurements taken on the tube cross-sections only show an increase towards the outer edges of the embedded cross-sections. This is due to the fact that, the material is embedded in epoxy resin, which influences measurement results of the UCI hardness equipment. Generally speaking, it can be said that both hard-

ness taken on the cross-section as well as along the surface range in the same intervals. Thus, hardness may be used as a validation parameter; the conversion of hardness to strength is thus a suitable validation parameter for the simulation model.
Final validation was then done comparing the converted hardness taken on the bent tubes as well as the maximum von Mises stresses from the FEM Abaqus model. The hardness measurements were taken both along the inside (along the inner bending radius, where material is compressed), outside (along the outer bending radius, where material is elongated) as well as the weld seam, see Figure 5-7.

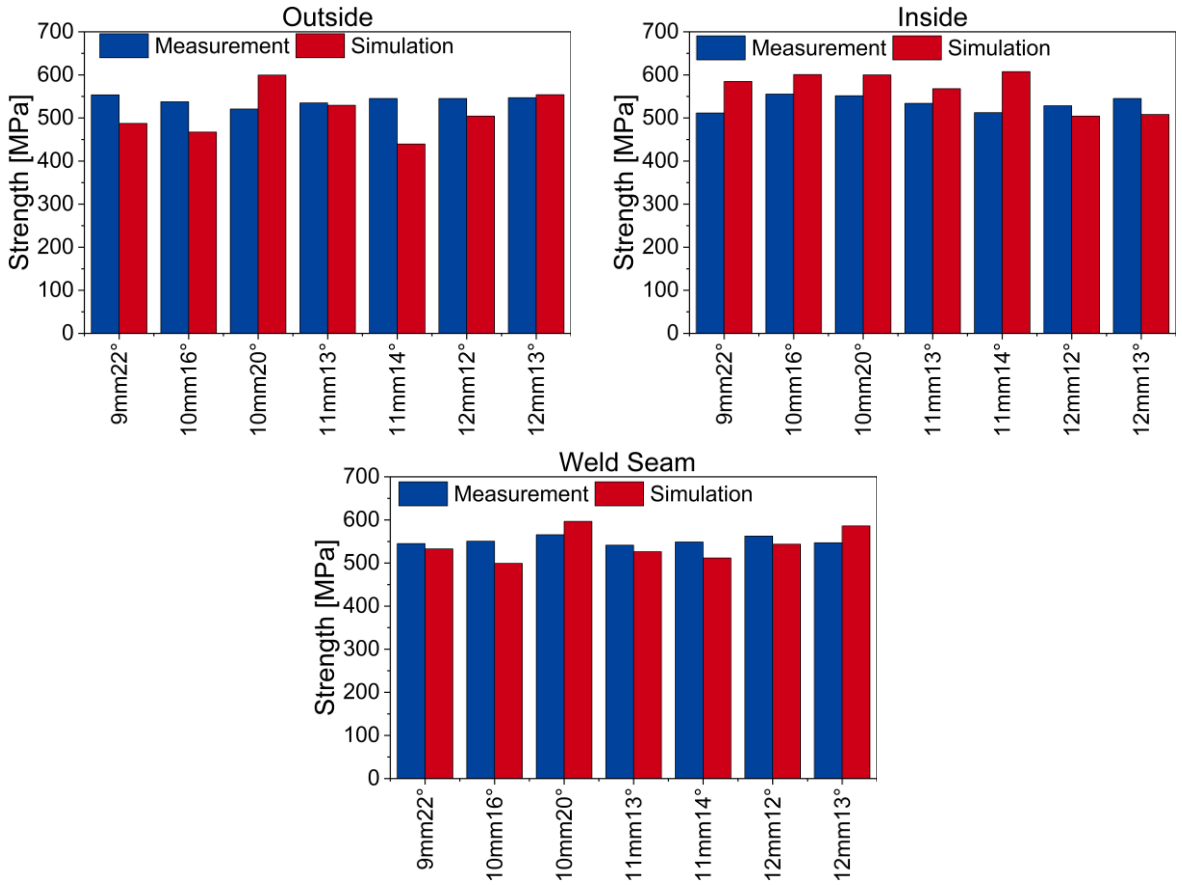


*Figure 5-7: Development of von Mises stresses based on hardness measurements as well as simulation on inside and outside of tubes as well as in weld seam.*

The strength values in the weld seam are higher than those of the base material. This is to be expected due to the different cooling conditions that the weld material experiences compared to the base material and the resulting HAZ. Furthermore, this was already indicated by the tensile tests, see Figure 5-4. Because the hardness measurements were performed in the fully bent material, all strength values were also taken post complete bending in the simulation. It can be observed that the Abaqus simulation is in good agreement with the hardness measurements converted to strength values. Strongest deviations can be seen for the bending strategy 11mm14°, however, for an overall modelling of the process, this is acceptable. Especially, as residual stresses

were not modelled within the FEM model of the tube, even though these have a non-negligible influence in the hardness as well, see detail in Chapter 5.3.

## 5.3 Investigation of residual hoop stresses in round tubes

The overall goal of this chapter is to understand the relationship between residual hoop stresses and hardness. To do so, three different residual stress annealing routes were conducted on round tube sections. Annealed as well as unannealed tube sections were then examined regarding their hardness in performing UCI hardness mappings along the tube cross-sections as well as their residual hoop stresses using the splitting method.

Residual stress annealing is commonly used to alleviate the residual stresses within a material. At the same time, a change in the mechanical properties is to be prevented. To do so, a material is heated up below $Ac_1$, austenitization temperature. It is held at the temperature for some time as to guarantee a thorough heating of the sample, followed by the most critical part, the cooling down. The cooling must be done very slowly, so that no new stresses are introduced into the material. As residual stress annealing is strongly dependent on the chosen material, the annealing routes were chosen according to the manufacturer's sheet [131]. The annealing was done in a chamber furnace manufactured by Nabertherm while in air environment at 580°C, 600°C and 620°C. The tubes were placed in the center of the furnace together with a thermocouple to monitor the exact annealing conditions. Post annealing, light-optical measurements were taken to see how the microstructure evolves due to the annealing process. The exact annealing conditions and the resulting microstructures can be taken from Figure 5-8.

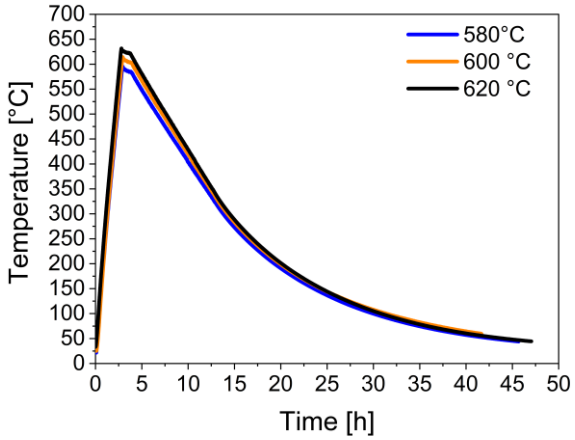


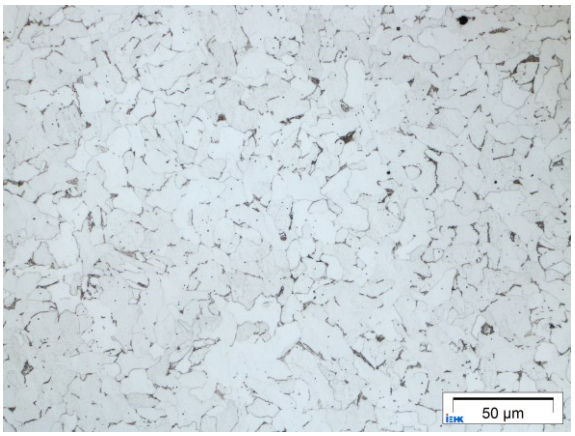


(a)

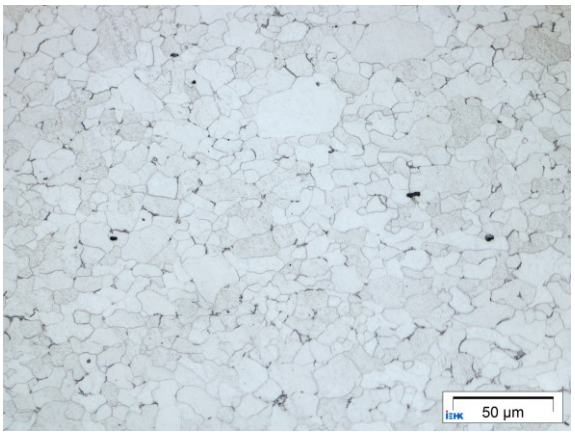


(b)


(c)

*Figure 5-8: Residual stress annealing conditions performed on the P235TR1(left) and (right) the resulting microstructures at 580°C (a), 600°C (b) and 620°C (c).*

It can be observed that the microstructure of the material in annealed state does not differ significantly from the initial microstructure of the base metal, compare Figure 4-1. Some individual grains in the 600°C and 620°C conditions are larger compared to the unannealed state. This indicates that the mechanical properties except for the residual stresses are not affected by the heat treatment.

Followingly, UCI hardness measurements were taken on cross-sections of both unannealed and the annealed material. UCI hardness measurements were chosen as the

indentation on the tubes are small and significantly more measurements can be taken along the cross-section compared to HV 10, which provides a better insight in the hardness development of the annealed tubes. The UCI hardness measurements were taken at a distance of 0.3 mm on tube cross-sections that were embedded in epoxy resin. The measurements were done according to DIN 50159-1 [132]. The results of the UCI hardness mappings can be seen in the following Figure 5-9.

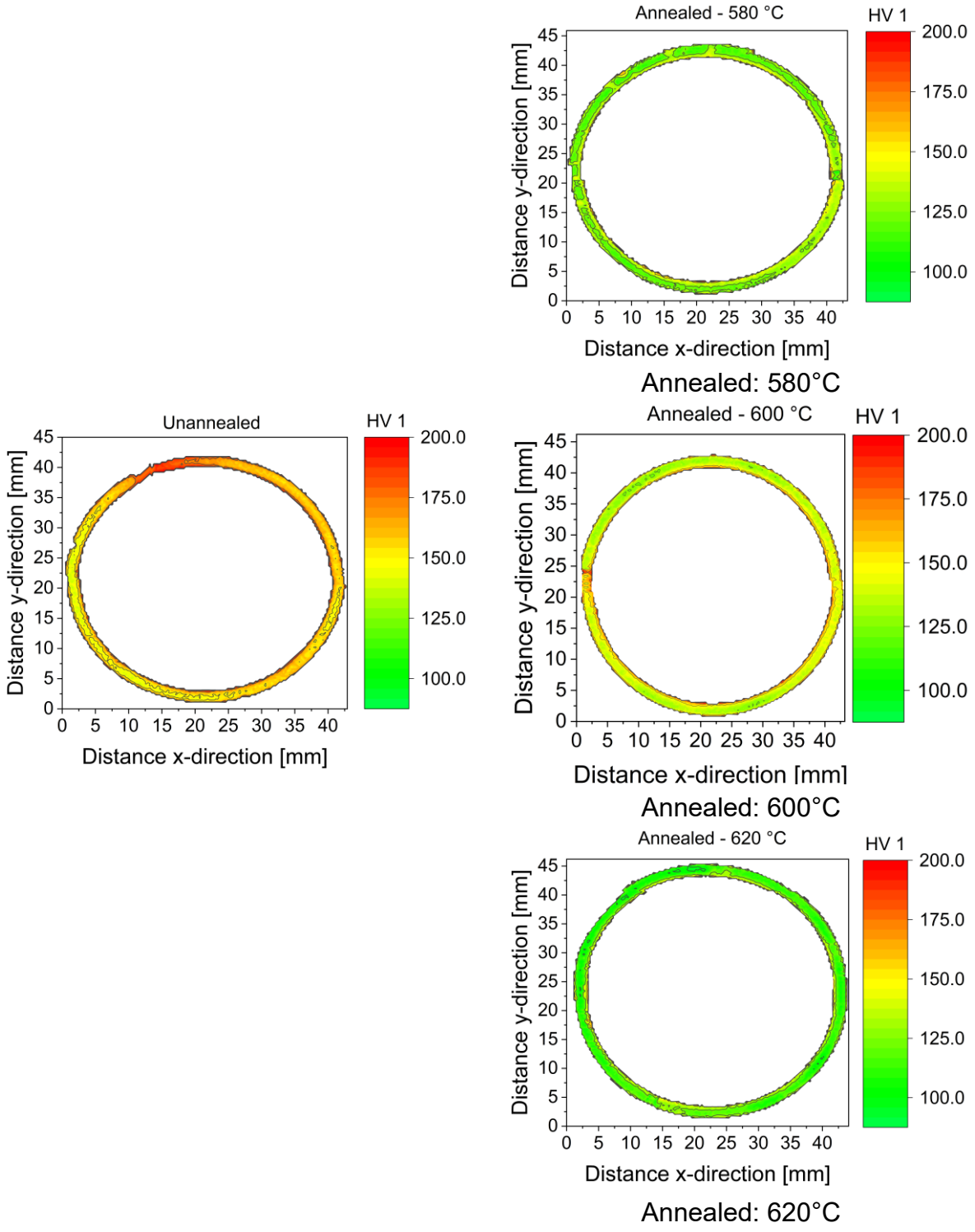


*Figure 5-9: UCI hardness mappings on (left) and (right) the resulting microstructures at 580°C, 600°C and 620°C.*

It can be seen that the hardness in the annealed states is significantly lower in the unannealed state. The increased hardness in each cross-section corresponds with the positioning of the weld seam. The overall hardness of the 600°C annealed state is a bit higher than that of annealed states 580°C and 620°C, which is unintuitive, however can be explained through batch fluctuations in the base material.

To investigate how the residual hoop stress state is in unannealed as well as annealed tubes, the splitting method was chosen, as it is a quick and inexpensive way to determine residual hoop stress that is effective on round tubes. In cutting into tube sections longitudinally, material subjected to residual hoop stresses will change its diameter. This allows the quantitative determination of residual hoop stresses in the tubes using the following mathematical relationship, Formula 5-1 [133,134]. Seven measurements were taken on the unannealed tubes and one on each of the annealed segments.

$$\sigma_{Hoop} = \pm \frac{E - s}{1 - \vartheta^2} * \frac{D_f - D_0}{D_f * D_0} \qquad \textit{Formula 5-1}$$

Where $\sigma_{Hoop}$ are the hoop stresses, $E$ the Young's modulus, $s$ the thickness of the tube, $\vartheta$ the poisson's ratio, $D_0$ the outer diameter before splitting and $D_f$ the diameter after splitting. For all tubes a thickness of $s = 2{,}6\ mm$ is taken. The results of the splitting method can be taken from the following Table 5-3:

*Table 5-3: Parameters for calculation of the residual hoop stresses according to [134].*

| Sample | 580° C | 600° C | 620° C | 1 | 2 | 3 | 4 | 5 | 6 | 7 |
|---|---|---|---|---|---|---|---|---|---|---|
| $\sigma_{Hoop}$ [MPa] | 183 | 166 | 147 | 237 | 237 | 225 | 234 | 234 | 222 | 233 |
| $D_0$ [mm] | 42.40 | 42.44 | 42.31 | 42.2 | 42.22 | 42.32 | 42.18 | 42.26 | 42.29 | 42.19 |
| $D_f$ [mm] | 42.96 | 42.95 | 42.76 | 42.92 | 42.93 | 43.00 | 42.88 | 42.94 | 42.96 | 42.90 |

The residual hoop stresses in the unannealed tube sections lie between 222 MPa and 237 MPa, while in the annealed states between 147 MPa and 183 MPa. Hence, the residual stress annealing was successful.

Since the hardness as well as the residual stress state in the annealed tubes are both decreasing, while the microstructure does not change significantly, it can be stated, that hardness and residual stress state are closely linked together. This relationship is explored further in the upcoming Chapter 6.

## 5.4 Conclusion and Evaluation of the results

This chapter is intended to firstly identify suitable DOF for the decoupling of the geometrical evolution of the bent steel tubes from the final mechanical properties. The forming temperature as a DOF was dropped early on as the placement of a heating coil within the machine is difficult to realize and can only be placed in front of the guider of the machine. However, that would entail that the material cools down significantly until it is actually bent. Another solution could have been a partial heating system. Tests by Maier [64] were conducted using a partial heating system, however, this led to considerable distortion of the tubes within the partially heated sections of the tube and was

also conducted prior to the bending and no further heating could be realized during the actual bending, again leading to heat loss of the component.
This makes temperature in the case of freeform bending an unsuitable DOF for control, as there is too much underlying heat loss that a control would need to implement, making it unnecessarily complicated.
The DOF/actuators feed rate as well as mandrel position do not show that they offer DOF to successfully decouple the mechanical properties from the geometrical evolution of the tubes. All tubes with varied feed rate and mandrel position have the same final bending geometry, however, also a very similar hardness profile. Hence, a decoupling using these DOF is not recommended.
Albeit, it could be established successfully that the superposition of stresses in the form of over- and underbending in tilting the tube out of its usual tangential position can successfully decouple the geometrical evolution from the microstructure evolution/mechanical property evolution during the process. In addition, this DOF can be controlled directly and offers the most suitable DOF/ actuator for a property-controlled freeform bending process. Hence, all further investigation will be based on the over- and underbent steel tubes.
Furthermore, this chapter introduces the material models of the base material and the weld seam for the FEM model in Abaqus CAE. The model is validated using hardness tests. This ultimately allows to generate a larger database for closed-loop control as well as a quick tool to evaluate process variables. Yet, the modelling of residual stresses, which are non-negligible in round steel tubes have not been modelled. This would further enhance the quality of the simulation model. However, as a preliminary simulation model for the macroscopic characteristics of local strengths and plasticity in the tubes, it suffices.
Lastly, the relationship between measurand hardness and residual hoop stresses (property of interest for the soft sensor) was examined. To do so, different residual stress annealing routes were performed on P235 TR1 to specifically realize different residual stress profiles in the tubes. These segments were then subjected to UCI hardness measurements to closely analyze the development of hardness versus residual hoop stresses. It could be observed that hardness decreases with a decrease in residual hoop stresses.
Based on these findings, a soft sensor can now be established, which is the topic of the following two chapters.

# 6 A System Identification and Implementation of a Soft Sensor for Freeform Bending

Sophie Charlotte Stebner, Daniel Maier, Ahmed Ismail, Shubham Balyan, Michael Dölz, Boris Lohmann, Wolfram Volk and Sebastian Münstermann

Materials (2021), 14, 4549
https://doi.org/10.3390/ma14164549

This chapter presents a soft sensor for the freeform bending process with movable die that allows the inline derivation of the mechanical properties of strength, residual hoop stresses as well as induced plasticity based on UCI hardness tests. The proposed soft sensor relies on the, in control engineering oftentimes used EKF, a state-space model for dynamic, non-linear systems.

The relationship between the measured hardness and the states of interest (strength and residual hoop stresses) is investigated and implemented into the EKF. The proposed filter then allows the prediction of the parameters of interest. Based on the estimations on materials strength, the induced plasticity level can subsequently be derived.

*Note: The figures were adapted from the original article for a better fit within the format of this document.

**Abstract**: The primary goal of this study is the formulation of a soft sensor that predicts industrially relevant mechanical properties for freeform bending. This serves as the foundation of a closed-loop property control. It is hypothesized that by inline measurement of hardness, predictions regarding residual hoop stresses, local strength and strain level can be achieved. A novel hardness-based correlation scheme is introduced, which is implemented into an extended Kalman filter (EKF) and allows an inline prediction of local strength, residual hoop stresses and plasticity. Furthermore, the ultrasonic contact impedance (UCI) method is validated as a suitable inline measuring solution.

**Keywords**: soft sensor; extended Kalman filter; freeform bending; residual hoop stresses; hard-ness; control-loop; measurement suitability; ultrasonic contact impedance

## 6.1 Introduction

Industrial plants are usually equipped with a manifold of sensors that are used to monitor as well as to control processes. Dependent upon the monitored process, the equipped sensors may have sampling rates that are too low or the measurements can only be conducted through extensive offline analyses, which is unsuitable for efficient process control [9,11]. Thus, researchers started developing predictive mathematical models from physically measured data sets that allow the continuous monitoring of relevant state variables of the processes. These predictive models, in combination with physically measured sensor data, are so-called soft sensors [9,11]. Soft sensors find their application in various fields, such as the control and optimization of bioprocesses [135], quality monitoring in the petrochemical industry [136] or even in the field of soft robotics [137]. Dependent upon the physical content of the soft sensor, the soft sensor model can be differentiated into two categories, namely model-driven and data-driven soft sensors. Model-driven soft sensors, also called white-box models, completely rely on physical-mathematical models of the process. Data-driven soft sensors, also called black-box models, are empirical models that purely rely on statistical relationships. A combination of these two models is also common, and is referred to as a grey-box model [9,11,138]. The authors in [138] present an overview of the characterization and classification of models and modelling specifically in metal forming, as well as in introduction to model selection.

The freeform bending process with a movable die offers an approach to bending complex geometries without changing the bending tool. Currently, a set geometry is bent while neglecting the mechanical properties of the workpiece. As freeform bending causes plastic deformation of the tube, not only does the material harden but the residual stresses in the part are influenced significantly [139]. Yet, the residual stress state, the hardening of the material and the ductility influences further processing steps

down to the production line as well as the service behavior of the component [29,39,43]. Thus, the need to control the mechanical properties decoupled from a set geometry arises, as this allows precise adjustment of the mechanical properties. The authors in [139] describe the bending process in detail and study the influence that different degrees of freedom of the freeform bending process have on the mechanical properties. They introduced a novel bending strategy, so-called non-tangential bending, which now allows the mechanical properties to be influenced while keeping a set geometry. Compared to normal freeform bending, the bending die has a non-tangential position during maximum deflection to the bent component. This position can lead to either underbending or overbending of the tube, see Figure 6-1. Non-tangential bending extends the result space for freeform bending and can be used for a decoupling of bent geometry (radius and angle of the tube) and the resulting properties of the tube [139].

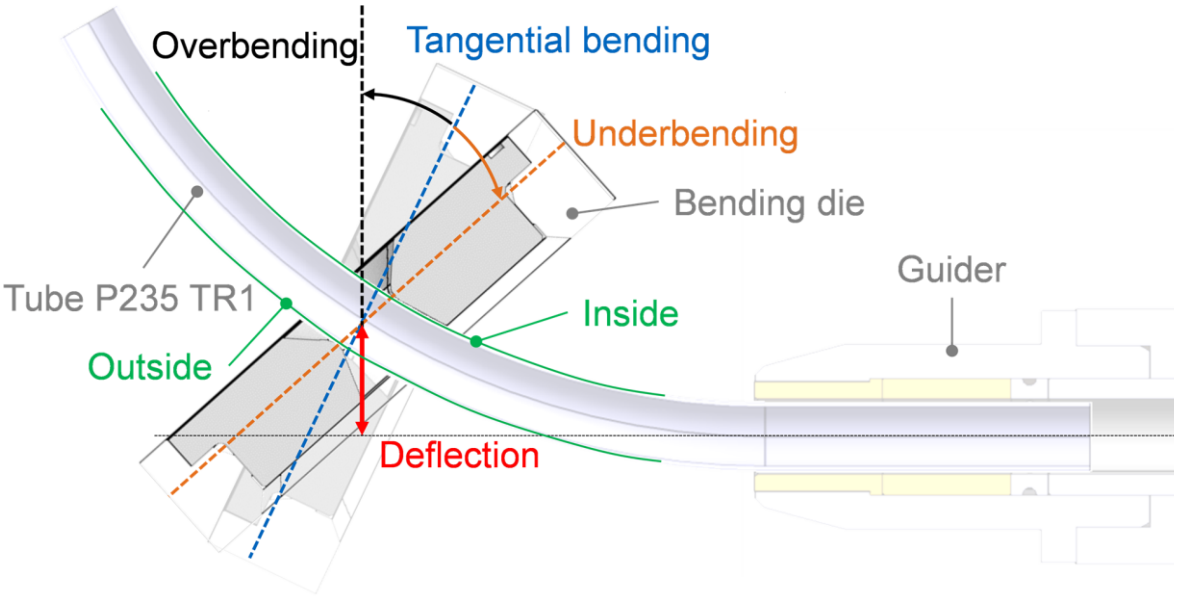


*Figure 6-1: Schematic depiction of non-tangential bending (over- and underbending) for freeform bending with movable die. Adapted from Ref. [7].*

The authors in [139] namely introduce seven bending strategies (9mm22°, 10mm16°, 10mm20°, 11mm13°, 11mm14°, 12mm12° and 12mm13°), where the denotation of, e.g., 9mm22° means that the bending tool was deflected by 9 mm and had a rotation angle of 22°. These bending strategies offer the same set geometry and constitute the tubes studied in this paper.

As the mechanical properties can currently only be determined by time-consuming, offline measurements, an intelligent solution in the form of a soft sensor is needed, as this allows inline prediction of inline unmeasurable quantities and can then serve as a basis for a control loop based on mechanical properties.

To develop a soft sensor for the freeform bending process with movable die, an analysis of the process data delivered by the physically measured data sets is necessary. This allows the derivation of a concept for correlating state variables in the soft sensor. This paper focuses on the process data analysis and the measurement equipment suitability and proposes a novel correlation scheme for local strength, strain level and residual hoop stresses derived from ultrasonic contact impedance (UCI) measurements for freeform bending, which will be introduced in Section 2. Part of the process data analysis is how the novel freeform bending strategy of non-tangential bending influences the mechanical properties of the material. Due to the bending process, the material will undergo plastic deformation, which will affect the residual stresses, plasticity and local strength [25,29].

Residual stresses are multi-axial stresses in equilibrium within a closed system that is not subject to any external forces or torques [39]. The residual stress states in the workpiece are influenced by nearly all manufacturing processes. A change in residual stress state can be caused by, e.g., locally varying thermal conditions or inhomogeneous plastic deformation [41,43]. In most cases, residual stress states can be neglected, yet in some cases the residual stress state must be considered as it determines the technical application of the workpiece. If not considered, the residual stress state can lead to failure of the workpiece such as crack formation, distortion, or maybe even detrimental failure [39,43]. Residual stresses are categorized into three types, namely residual stresses of type I, II and III. They can be of tensile and compressive nature and are dependent upon the orientation in the tube. They can be differentiated into hoop residual stresses, longitudinal residual stresses and radial residual stresses [140]. Tensile residual stresses can render an entire workpiece useless if the component must withstand high load stresses, while compressive residual stress states can positively influence the workpiece's lifespan [41].

The residual stress state can currently only be quantitatively investigated by extensive offline analyses such as (semi-) destructive investigation methods, e.g., the drill hole method [141,142] and sectioning methods [134], as well as non-destructive investigation methods such as the x-ray diffraction measurement or magnetic methods, e.g., BHN analysis [28,143]. Magnetic BHN, in particular, poses a good alternative, but the signal among different types of materials is not comparable as different microstructures lead to different micromagnetic signals [28]. Yet, to make freeform bending more efficient, an inline monitoring of the residual stresses is needed that can also be used across a variety of materials, which will be investigated in this work.

In addition to the residual stress state, the strain hardening of the material, due to the bending process, needs to be investigated. Strain hardening of a material is influenced namely by the degree of deformation $\varphi$, the strain rate $\dot{\varepsilon}$ and the Temperature $T$. The authors in [139] have shown that the influence of the strain rate $\dot{\varepsilon}$ on strain hardening during freeform bending with a movable die can be neglected. During forming, $\varphi$

changes the order and density of the dislocations, phase distribution and grain shape of the material. During cold forming, an increased $\varphi$ causes the dislocation density of the material to rise, meaning the material strain hardens while the elongation capacity decreases [25,29]. Depending on the loading case of the bent workpiece, it is necessary to know how much the material strain hardened and elongated during the bending process, as it will influence the application and lifespan of the workpiece [28]. Thus, the local strength as well as plasticity are of importance to monitor during the bending process.

It is commonly known that tensile testing provides information on materials' characteristics such as yield strength, tensile strength, strain hardening behavior and maximum elongation [130]. It is also commonly known that the tensile strength of a material can be analytically correlated to the measured hardness [144]. Furthermore, an influence of residual stresses on hardness have also been proven [145]. Yet, an analytic correlation between hardness, the local strength and residual stresses has not yet been proposed. Thus, this work proposes a novel correlation scheme based on measured hardness, Section 6.2.3, that is implemented into a soft sensor.

For the soft sensor itself, a suitable model must be identified. When analyzing the system closely, the development of the mechanical properties influenced by the freeform bending process depicts a dynamic, nonlinear system. The term of a dynamic system describes a state space within which the defined coordinates describe the state at any given point in combination with a dynamical rule using the present values of the state variables in order to describe the state variables' direct future [146]. While nonlinearity of a dynamic system means that the system's output cannot be described by a linear operator applied to the system's input [109]. The nonlinearity of the system is derived from the results of [139], as the residual hoop stress state influences the hardness nonlinearily. Models for nonlinear, dynamic systems are manifold. Among these are for example NARMAX models [147], neural networks relying solely on statistical relationships between variables [147], Kalman-filters [147] and various others. The authors have chosen the extended Kalman filter to model the development of the mechanical properties, as this is a well-researched algorithm for non-linear dynamic systems that has a relatively low complexity [148]. As no previous filter has been introduced for the freeform bending process, the authors chose the EKF as the basis for the proposed soft sensor. Thus, any other model will not be discussed further.

The extended Kalman filter (EKF) is an advancement of the Kalman filter. As the development of the mechanical properties depicts a nonlinear system, the EKF is needed. The EKF linearizes the system about a current estimate in each time step by implementing a Jacobian matrix, meaning a first-order partial derivative of a vector function with respect to a vector [148]. To give a state estimate, the algorithm utilizes two steps: a prediction and an update step that are modelled by the following equations [148]:

*Prediction Step*

| | | |
|---|---|---|
| State Estimate | $\hat{x}_k^- = g(\hat{x}_{k-1}^+, u_{k-1})$ | *Formula 6-1* |
| Error Covariance | $P_k^- = F_{k-1} P_{k-1}^+ F_{k-1}^T + Q$ | *Formula 6-2* |

*Update Step*

| | | |
|---|---|---|
| Measurement Residual | $\tilde{y}_k = z_k - h(\hat{x}_k^-)$ | *Formula 6-3* |
| Kalman Gain | $K_k = P_k^- H_k^T (R + H_k P_k^- H_k^T)^{-1}$ | *Formula 6-4* |
| Updated State Estimate | $\hat{x}_k^+ = \hat{x}_k^- + K_k \tilde{y}$ | *Formula 6-5* |
| Updated Error Covariance | $P_k^+ = (I - K_k H_k) P_k^-$ | *Formula 6-6* |

The hat operator describes that the variable is an estimate, whereas the superscripts − and + denote that the estimates are predicted or updated estimates of the variable. Term $P$ is called the state error covariance and describes the error covariance the filter thinks the estimate error has. Due to its summation with $Q$, the error covariance increases in the prediction step, which means that the filter is more uncertain in the estimate of the state variable after prediction [148]. During the update step, the measurement residual, $\tilde{y}_k$, is computed first. It is the difference between the true measurement, $z_k$, and the estimated measurement, $h(\hat{x}_k^-)$, where $h$ is the measurement matrix. The residual is later multiplied by the Kalman gain $K_k$ to provide the updated state estimate $\hat{x}_k^+$. The filter then computes the updated error covariance $P_k^+$ to use in the next time step. The updated error covariance is smaller than the predicted error covariance, meaning the filter became more certain. $F$ and $H$ are two Jacobian matrices, which serve the purpose of linearizing the nonlinear system [148].

The following sections will present how the correlation scheme based on hardness deriving from local strength, ductility and residual hoop stresses is formulated and how each term influences the hardness. Furthermore, the measurement suitability of UCI hardness measurements is analyzed as an inline-monitoring solution by investigation surface influences as well as cross-referencing the UCI method with Vickers hardness scale HV 10 measurements (Dia-Testor 731, Instron Wolpert, Ludwigshafen, Germany). The derived correlation scheme and all influencing parameters are lastly implemented into the EKF to enable inline monitoring of all relevant mechanical properties during the freeform bending process.

## 6.2 Materials and Methods

This section gives a short overview of the investigated material. Furthermore, inline measurement suitability of UCI hardness measurement equipment is investigated. The focus lies on the introduction of the novel correlation scheme based on UCI hardness measurements that depict the basis for inline monitoring of the residual hoop stresses, the local strength, as well as the plasticity during freeform bending.

### 6.2.1 P235 TR1

The material used in this investigation is P235 TR1. It is a low-alloyed steel grade that is designed for pressure purposes, where the alphanumerical definition of TR1 depicts a grade without fixed values for the impact energy or a defined aluminum content [116,117]. The material is ferritic with a small fraction of perlite, see Figure 6-2. The chemical composition investigated by optical emission spectrometer can be taken from Table 6-1.

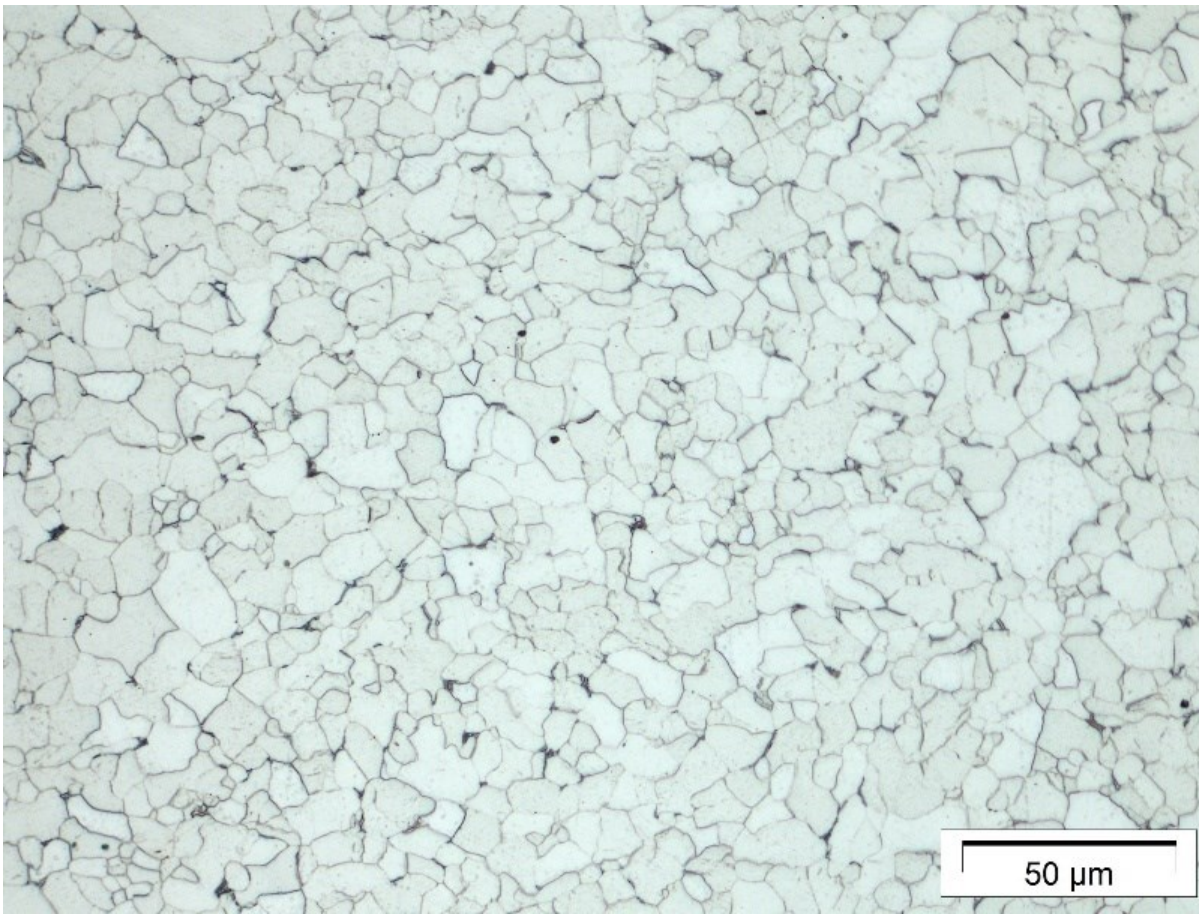


*Figure 6-2: Microstructure of P235 TR 1 investigated by light optical microscope, magnification 500×.*

*Table 6-1: Chemical composition of P235 TR 1 in mass percent investigated by optical emission spectrometer.*

| **Element** | C | Si | Al | Mn | P | S | Cr | Cu | Mo | Ni |
|---|---|---|---|---|---|---|---|---|---|---|
| P235 TR1 | 0.037 | 0.027 | 0.025 | 0.11 | 0.0048 | 0.0016 | 0.041 | 0.244 | 0.011 | 0.081 |

The circular steel tubes have an outer diameter of 42.4 ± 0.5 mm, a thickness of 2.6 ± 0.3 mm and a length of 800 ± 2 mm. The tubes are welded longitudinally and are finished evenly both on the inner and outer part of the tube as is necessary for freeform bending. The tubes are manufactured according to DIN EN 10217-1 and DIN EN 10219-1 [116,117].

### 6.2.2 Inline-Measurement Suitability and Measurement Uncertainties of UCI Hardness Testing

Firstly, it must be established whether UCI hardness testing is suitable for inline measuring of hardness. UCI hardness testing uses a longitudinally oscillating rod with a Vickers diamond at the end. This diamond is pushed into the object to be tested. The defined load is usually applied by a spring. The rod oscillates at its natural resonant frequency, which depends mainly on its length. When the Vickers diamond penetrates the sample, this vibration is damped. The damping of the rod and thus the change in frequency to be measured depends on the size of the contact area between diamond and sample. In combination with the known load and the stored calibration values, the measured frequency directly determines the hardness of the material [28,132]. The advantage of the UCI hardness measuring method is that it offers a good inline-measuring capability as the measuring equipment is portable, can be integrated into the freeform bending machine, and is of a semi-destructive nature. However, as faulty test equipment and measuring uncertainties can lead to faulty test results, the UCI hardness measurements will be investigated regarding their inline measurement suitability as well as regarding the systematic and statistical measuring uncertainties.

The measurement suitability will be examined by cross-referencing UCI hardness measurements with HV 10 measurements. The HV 10 measuring method also utilizes a diamond attached to a straight pyramid with an angle of 136° between the opposing sites to indent the test specimen surface. The diamond is pushed vertically into the material with a defined test force F. The Vickers hardness HV 10 is then calculated by measuring the mean value of the diagonals that result from the indentation of the diamond and are corrected by a factor due to the curvature in the tube [149]. To conduct the HV 10 measurements, the surface of the tube must be polished, because HV 10 relies on the optical measurement of the indentation. A tarnished surface cannot be evaluated. Thus, the surface to be investigated was treated by a fan grinder with the grit of 80 to clean off any tarnishes. HV 10 measurements were chosen as the results

are comparable to UCI hardness measurements and it is an established method to determine hardness in a stationary fashion [28].

A method used in statistics to compare two measurement methods of the same variable that serves as a tool to analyze the concordance between these two methods is the so-called Bland–Altman plot. Such a plot will be defined for UCI hardness measurements and HV 10 measurements. Given that the difference between the measurements is normally distributed, plotting the difference between the measured values of UCI hardness and HV 10 measurements against the mean value and implementing three lines that define the limits of agreement, i.e., the mean value of the difference as well as the mean value of the difference plus or minus 1.96 times the standard deviation of the difference, it is possible to determine the agreement between the two measuring tools. It is recommended that 95% of the data points should lie within the limits of agreement. If that is the case, HV 10 measurements can be replaced by UCI hardness measurements [150,151]. To test the normal distribution of the difference between the measurements, a Kolmogorov–Smirnov test was conducted [152].

Additionally, a study regarding influences of the surface condition of the results is conducted, as [153] have shown that surface roughness can influence measurements. Surface roughness analysis was performed by investigating two different surfaces– the untreated and polished surface. The polished surface was treated by a fan grinder with a grit of 80 along the inside and outside surfaces of the material. Denotation of inside and outside is used according to Figure 6-1.

Lastly, measurement uncertainty is analyzed by determining the systematic measurement error and statistical measurement uncertainty of the UCI hardness measuring device (INNOVATEST MET-U1A, HaBu Hauck Prüftechnik GmbH, Hochdorf-Assenheim, Germany). Systematic measurement errors are deviations in the measurement results that are the same every time a measurement is taken. They cannot be identified by statistical analyses. This type of error is difficult to determine as well as to eliminate. Usually, systematic errors are due to the experimental set up or the calibration of the equipment [154]. Statistical measurement uncertainty is a characteristic value obtained from measurements and is used together with the measurement result to identify a range of values for the true value of the measurand [154]. A simple method to determine statistical measurement uncertainty is determining the repeatability standard deviation as follows:

Repeatability Standard Deviation

$$s = \sqrt{\frac{1}{n-1}\sum_{i=1}^{n}(x_i - \bar{x})^2} \qquad \textit{Formula 6-7}$$

where $x_i$ is the corresponding single measured value and $\bar{x}$ the arithmetic mean of all measurements. In general, the larger the statistic, the better the probability distribution of the true value can be estimated from the standard deviation and mean [154]. Thus, a statistic of thirty measurements under equal conditions were conducted.

### 6.2.3 Correlation Scheme Based on Hardness

The core of this work lies in the proposed, novel correlation scheme based on hardness that offers an analytical relationship between hardness, local strength and residual stresses within the tube (see Formula 6-8)).

Correlation Scheme

$$HV_{Total} = HV_{Groundstate} + HV_{Strain\ Hardening} + HV_{Residual\ Stresses} \quad \textit{Formula 6-8}$$

The correlation scheme hypothesizes that the measured hardness of the total system is influenced especially by three parameters:

- The hardness of the ground state, meaning the hardness of the material itself without any influences of strain hardening or residual stresses due to shaping within the material. It can be measured by hardness measurements taken from tensile test samples, as these are in a uniaxial stress state.
- An increase in hardness due to the strain hardening of the material because of plastic deformation by bending.
- Lastly, the residual stresses within the steel tube.

As the algorithm derives the local strength from the hardness, the information of the strength will then be utilized by the soft sensor to derive the level of plasticity.
Each of the above mentioned parameters of the correlation scheme as well as the derivation of the level of plasticity are investigated closely within this work. The tests were performed on non-tangentially bent steel tubes according to [139]. All influencing parameters are investigated separately. The next section introduces the methods of determining the individual parameters.

#### *6.2.3.1 Determination of $HV_{Total}$*

From the total hardness measurements, the soft sensor will ultimately derive the local strength, residual hoop stresses and plasticity level. Total hardness was determined by conducting UCI hardness measurements by hand along the surface of the steel tubes (see Figure 6-3). Three hardness measurements were taken every two centimeters apart on the inside as well as the outside of the tube. Only three measurements were taken, as the measurements need to have a small distance between them so as not to measure the same point twice, since this leads to faulty results and can result in the indenter breaking.

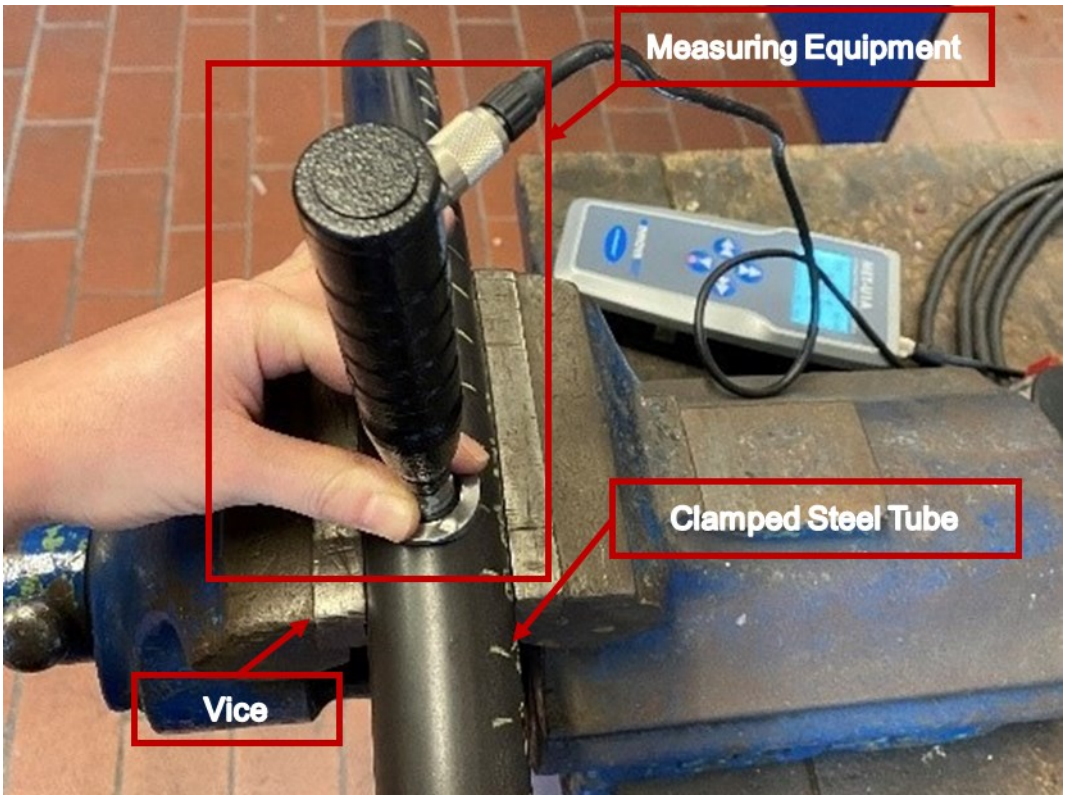


*Figure 6-3: Method of conducting UCI hardness tests on bent steel tube (outside). UCI measuring equipment is used by hand to take hardness measurements of clamped steel tube.*

#### *6.2.3.2 Determination of HV $_{Groundstate}$, HV $_{Strain\ Hardening}$ and Plasticity*

In conducting tensile tests according to DIN EN ISO 6892-1 [130] with miniature tensile test samples, both the strain hardening and plasticity level of the material can be studied. By taking the hardness value of miniature tensile test samples, an overview of the hardness without any influences due to shaping the material into the tube is given. Ten specimens were tensile tested until failure to determine the strain hardening behavior for an array of samples. These data were then used to model the tensile test with Abaqus CAE in order to derive the local strength and ultimately the true plasticity level. A flow curve was fitted using the Ludwik–Voce Equation (see Formula 2-17). The according fitting parameters can be taken from Table 5-1.

Another fourteen specimens were tensile tested and stopped at certain plasticity points, namely 1% until 14% of conventional plastic strain, to measure the hardness the material has at various plasticity points. By analyzing the displacement in the stopped tensile test, the according strength values can be derived from the simulation, thus the strain hardening behavior can be determined.

After testing, the stopped miniature tensile test samples were embedded into epoxy resin and UCI measurements were taken along the surface of the reduced section to

determine $HV_{Groundstate}$ and $HV_{Strain\ Hardening}$. In taking the UCI hardness and matching the hardness to the local strength value, the relationship between hardness and local strength can be derived and subsequently implemented into the soft sensor.
The level of plasticity was also derived by using the data from the simulation. In analyzing the plasticity level and varying strength values derived from hardness measurements by the EKF, the strength values can be cross-referenced with the tensile tests, thus offering insights into the plasticity level reached during plastic deformation, see Section 6.2.3.4.

#### *6.2.3.3 Determination of HV Residual Stresses*

To determine the last term of the correlation scheme, $HV_{Residual\ Stresses}$, the influence that hoop stress has on hardness was closely analyzed. To do so, the approach the authors in [134,139] chose was utilized and this analysis relies on their results.
In plotting the residual stresses against the hardness, a regression can be derived to model the development of the residual hoop stresses with varying hardness of the EKF. The regression results that are implemented into the EKF will be presented in Sections 6.3.5 and 6.3.6.

#### *6.2.3.4 Implementation into the Soft Sensor*

The previously determined relationships now need to be implemented into the soft sensor. The soft sensor computes the different mechanical properties in two steps. Firstly, the EKF is implemented, which derives and predicts the local strength and residual hoop stresses. In the second step, after the EKF derives the local strength value, the soft sensor then uses the strength value and scans the tensile test data for the same strength values. The soft sensor starts to scan the data when plastic deformation begins as the elastic deformation behavior is not of interest and could lead to faulty predictions. After the tensile test data is scanned, the soft sensor then returns the true strain that was induced during bending.
For the EKF, an initial state needs to be declared. In this case, the initial state is a vector that describes the hardness, residual hoop stresses and strength of the material. For the initial state, uncertainty in form of the covariance matrix needs to be implemented, namely $P$ in Formula 6-2. As the initial state was a vector, the covariance matrix is now a matrix containing the implemented three states. The values for $Q$ in Formula 6-2 depend on the sensor accuracy. If the sensor accuracy is high, smaller values should be initialized, whereas larger values should be implemented if the sensor accuracy is low. In initialization, the values were set to 0.9. Fundamental to the algorithm is the dynamics matrix and the Jacobian matrix thereof. The dynamics matrix depicts how the residual hoop stresses and local strength values develop depending on the hardness. This means that the analytical relationships that were determined in Sections 6.2.3.2 and 6.2.3.3 are implemented into the dynamics matrix and determine the state estimate $\hat{x}_k^-$ in Formula 6-1. The Jacobian of the dynamics matrix, namely $F$

from Formula 6-2, is then used to calculate the error covariance and influences the Kalman gain. The EKF must also be given what is measured and how the measurement relates to the initialized state vector. Again, the filter is told that measurement of hardness is computed to strength and residual hoop stresses. Then, the Jacobian of the measurement matrix with respect to the state matrix is computed and is utilized in the computing of the measurement residual, Formula 6-3, of the update step. The filter now approximates the current measurement by multiplying the predicted state with the measurement matrix, Formula 6-4. In multiplying the residual and the Kalman gain, the correction of the predicted term based on the new measurements is obtained, Formula 6-5. When the updated state estimate is computed, the error covariance is computed (Formula 6-6) and used in the next prediction step. The subscript $k$ describes in this case the spatial progression along the steel tube.

When in use, the algorithm reads a csv-file with UCI hardness measurements taken previously on the steel tube. The data is then processed by the EKF, meaning that the residual hoop stresses and strength are derived and their development is predicted. The predicted local strength is then used to derive the level of plasticity. This means that the EKF returns a local strength value and this term is then used to scan the tensile test data for a matching pair. As already mentioned, the scan begins with plastic deformation to circumvent any mismatches with strength matches during elastic deformation. Ultimately, the algorithm provides estimates and predictions for residual hoop stresses, local strength and plasticity based on hardness measurements by utilizing mathematically derived relationships. The operating principle of the soft sensor is illustrated in Table 6-2.

*Table 6-2: Operating Principle of Soft sensor. The EKF predicts strength and residual hoop stresses; the soft sensor then uses the predicted strength values from the EKF named predList.Strength and scans the tensile test data to return the plasticity level in plasticityList.*

| **Algorithm 1: Extended Kalman Filter for Material Parameter Prediction** | |
|---|---|
| **Input :** Hardness values on inside/outside at different points on the material | |
| **Output:** Intermediate output: Predicted strength and hoop stress values for the corresponding hardness values | |
| Final output: Plasticity range for each of the predicted strength values | |
| 1 | initialize empty material parameter prediction list ’predList’ and ’plasticityList’ |
| 2 | initialize a pandas dataframe (distance and inside-outside hardness) |
| 3 | compute ‘strength’ values for the corresponding hardness values using the correlation: **strength = hardness × 2.88** |
| 4 | compute ‘hoop stress’ values for the corresponding hardness values using the correlation: **hoop-stress = 46.2502 × exp(0.00992 × hardness)** |
| 5 | initialize $x_0$ (initial state vector). If nothing is known, simply enter zero here. |
| 6 | define a state matrix, which consists of all possible attributes in the system and a dynamics matrix with respect to the state matrix. |

7 compute the Jacobian matrix $J_A$ (first-order partial derivatives) of the dynamics matrix with respect to the state matrix.

8 define a measurement matrix which consists of all attributes that are being measured in the system and compute its Jacobian matrix $J_H$ with respect to the state matrix.

9 the non-linear function $g(x_k, u)$ consists of all the regression expressions, where the control input $u$ is zero and function $h(x)$ is the measuring function that consists of the measurements from regression.

10 initialize state co-variance matrix $\mathbf{P}$ to add uncertainty to the initial state (if the sensors are not accurate) and process noise co-variance matrix $\mathbf{Q}$ for the 'prediction' step.

11 initialize measurement noise co-variance matrix $\mathbf{R}$ (use smaller values if sensors are accurate) **for the** 'correction' step.

12 Function Prediction ( ):

13 Project the state ahead: $x_{k+1} = g(x_k, u) = \begin{bmatrix} 2.88 \times \text{hardness} \\ 46.2502\ e^{0.00992 \times \text{hardness}} \\ \text{hardness} \end{bmatrix}$

14 Project the error co-variance ahead: $P_{k+1} = J_k\, P_k\, J_A^T + Q$

15 **return** $x_{k+1}$

16 **Function** Correction (z):

17 Compute the Kalman Gain: $K_k = P_k\, J_H^T \left(J_H\, P_k\, J_H^T + R\right)^{-1}$

18 Define the measuring function:

$$h(x_k) = \begin{bmatrix} \text{strength} \\ \text{hoop} - \text{stress} \end{bmatrix} = \begin{bmatrix} 2.88 \times \text{hardness} \\ 46.2502\ e^{0.00992 \times \text{hardness}} \end{bmatrix}$$

19 Update the estimate via measurement: $x_k = x_k + K_k(z_k - h(x_k))$

20 Update error co-variance: $P_k = (I - K_k\, J_H)\, P_k$

21 **for** $z$ in measured values **do**:

22 val = Prediction ()

23 Add val to predList

24 Correction (z)

25 **end**

26 **Computation of Plasticity after EKF predicted strength**

27 initialize a pandas dataframe 'df' (measured strength and plasticity values)

28 perform the required rounding off for the measured as well as the predicted strength values to get an appropriate match.

29 **for** value in predList.Strength **do**

30 result = df.loc[df['Strength'] == value].Plasticity

31 Add result to plasticityList

32 **end**

33 **return** plasticityLis

## 6.3 Results and Discussion

This section presents the results and the discussion of this work. Firstly, the measuring equipment suitability is analyzed where UCI hardness measurements in comparison to HV 10 measurements are shown. Additionally, surface roughness influences are given. Yet, the focus lies in the derivation of local strength, residual hoop stresses, and plasticity by hardness measurements. The results for each term in the correlation scheme will be presented and a regression drawn. Furthermore, the implementation of the regressions in the EKF algorithm and the predictions generated by the soft sensor will be introduced.

### 6.3.1 Measurement Equipment Suitability—Comparison of Measuring Methods

The measurement suitability of the UCI hardness measurements is investigated by comparing the UCI hardness values with HV 10 measurements. This was done by performing both UCI hardness measurements and HV 10 measurements on all seven differently non-tangentially bent steel tubes. Figure 6-4 shows exemplarily the comparison of UCI hardness vs. HV 10 hardness on tubes 10mm16° both on the inside and the outside of the tube. Based on that data, a Bland–Altman plot was formulated for the UCI hardness and HV 10 measurements to ultimately prove whether UCI hardness measurements are suitable for inline measuring.

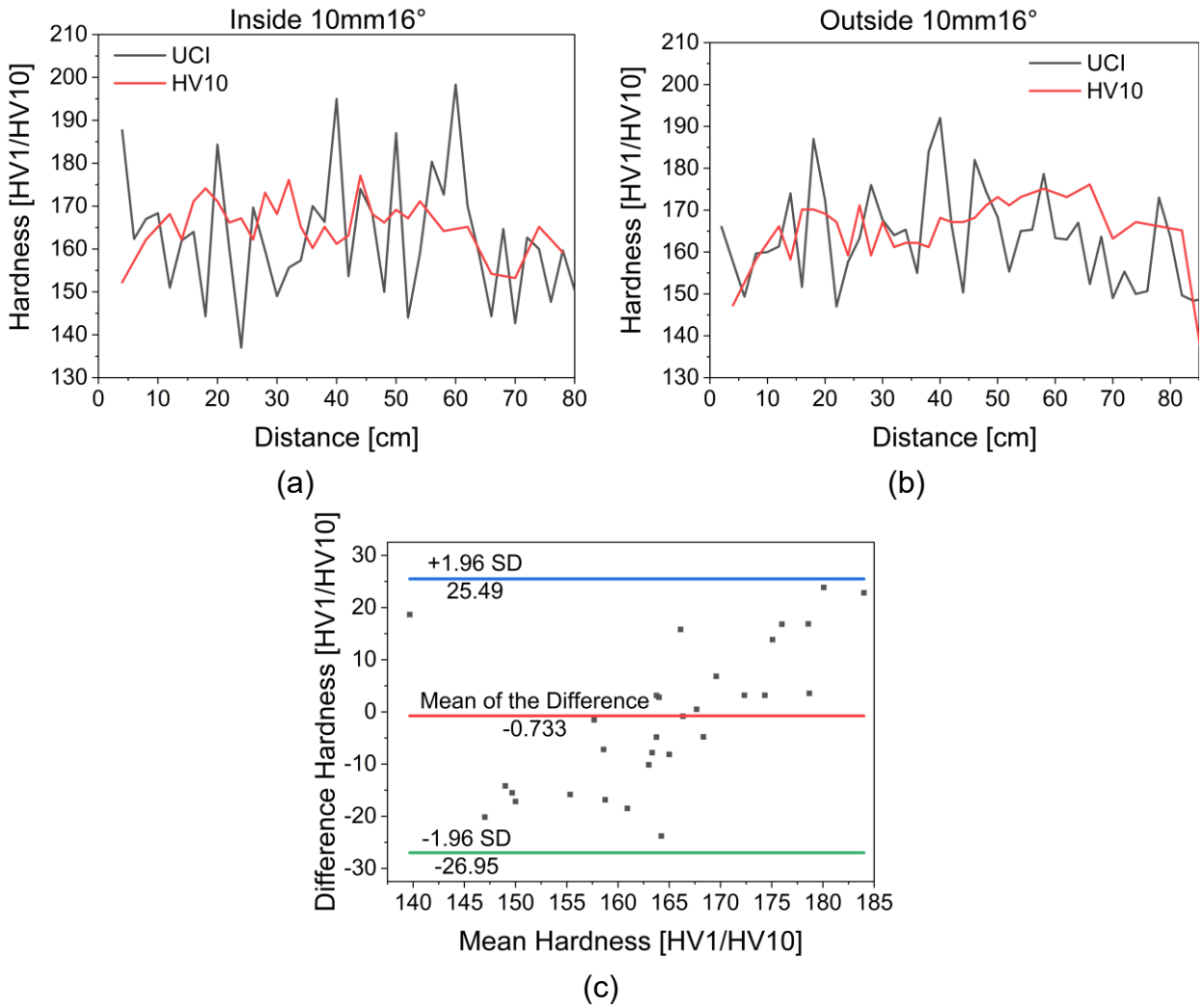


*Figure 6-4: UCI hardness plots vs. HV 10 hardness plots for measurement suitability analysis; (a) UCI hardness vs. HV 10 measurements of non-tangentially bent tube with bending strategy 10mm16°on the inside; (b) UCI hardness vs. HV 10 measurements of non-tangentially bent tube with bending strategy 10mm16° on the outside; (c) Bland–Altman plot for concordance analysis between UCI hardness and HV 10 hardness measurements taken on 10mm16° bent tube.*

In Figure 6-4, the UCI measurements scatter more than the HV 10 measurements. However, it is visible that both measurements suggest the same hardness development along the tube. Considering that UCI hardness measurements are taken by hand, a higher scatter in measurement data is plausible. Even though the steel tube was clamped tightly during measurement and the measurements were conducted by the same person, manual measurements have the tendency to scatter in a larger fashion. To quantitatively describe whether UCI hardness measurements are suitable for in-line measuring, a Bland–Altman plot was formulated according to Section 6.2.2. The Kolmogorov–Smirnov test shows that for a confidence interval of $\alpha = 0.05$ the critical value of 0.2342 is not surpassed by the maximum deviation in the test statistic, namely 0.0808, meaning the null hypothesis will not be rejected. Thus, the difference is distributed normally, and a Bland–Altman plot can be formulated to compare UCI hardness

and HV 10 measurements. The Bland–Altman plot shows that the mean of the difference is −0.733 and the limits of agreement are −0.733 + 1.96 × SD and −0.733—1.96 × SD. All data points lie within the defined limits of agreement, meaning that UCI hardness measurements offer a good alternative to HV 10 measurements and are suitable as an inline measuring method [150,151].

### 6.3.2 Measurement Equipment Suitability—Investigation of Surface Roughness Influences

Figure 6-5 shows the development of hardness measurements along the inside and outside of the steel tube with treated and untreated surfaces. All seven non-tangentially bent steel tubes were examined, but only two exemplary tubes are shown in the following figures, as the results are comparable.

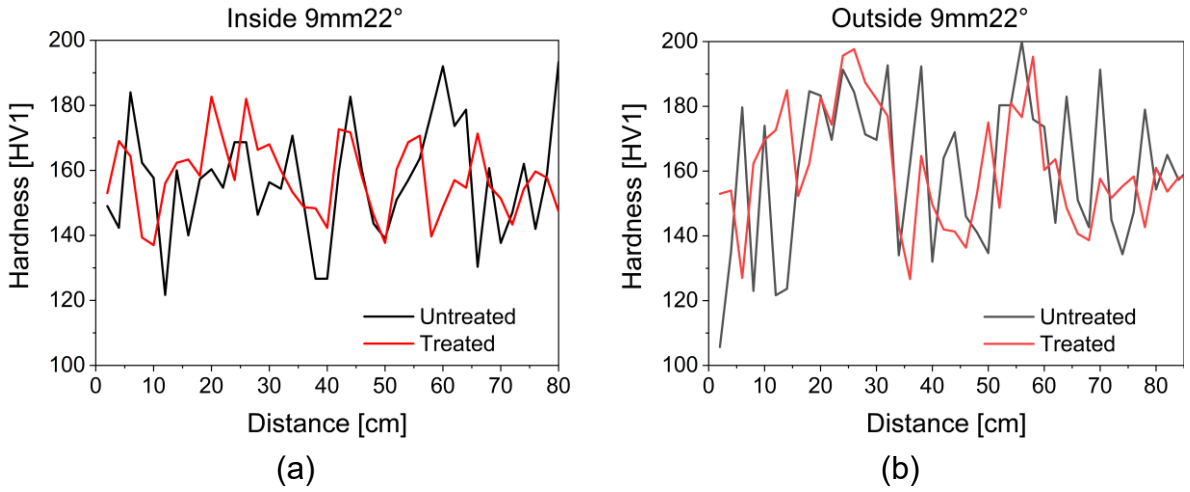


*Figure 6-5: Development of UCI hardness on treated and untreated surfaces along the inside and outside of the steel tube; (a) UCI hardness development on untreated and treated surfaces on inside of steel tube 9mm22°; (b) UCI hardness development on untreated and treated surfaces on outside of steel tube 9mm22°.*

Surface roughness influences, seen in Figure 6-5, do exist for the UCI hardness measurements. Outliers become less prominent in the treated surfaces, yet both measurements describe identical trends in hardness. Surface roughness in this case means a tarnished surface and roughness due to lubricants from bending. Although an inline surface preparation will not be possible during the bending process, the authors decided to formulate the correlation scheme based on measurements with treated surfaces, particularly as the individual correlation terms of $HV_{Strain\ Hardening}$ and $HV_{Residual\ Stress}$ were also determined on samples with a treated surface. It is permissible to formulate the correlation scheme based on data with treated surfaces, as the surface roughness does not have an influence on the underlying mechanical properties such as strain hardening and residual stress state variations. Furthermore, the UCI measurement method relies on the dampening of the oscillation in the rod and not on

an optical evaluation. Thus, it is acceptable to perform measurements on surfaces with a higher roughness later on [153].

### 6.3.3 Measurement Equipment Suitability–Investigation of Systematic Measurement Error and Statistical Measurement Uncertainty

As a systematic measurement error, the authors could identify that the UCI measurements along the surface were taken by hand. To minimize the measurement error, all hand measurements were taken by the same person and a custom-made guider for the UCI hardness measuring device was utilized. All steel tubes were tightly clamped during the measurements as to eliminate any influences due to displacement of the sample. As the UCI hardness measurement equipment will ultimately be incorporated into the machine and guided by a machine, the systematic measurement error “manual testing” will be eliminated.

The statistical measurement uncertainty was determined by measuring a treated, unbent steel tube in an area of two centimeters with thirty measurements in order to derive the standard deviation. The following Table 6-3 depicts the statistical data as well as the standard deviation determined according to Formula 6-7.

*Table 6-3: Determination of statistical measurement uncertainty by standard deviation according to Formula 6-7.*

| **Measurement** | **1** | **2** | **3** | **4** | **5** | **6** | **7** | **8** | **9** | **10** | |
|---|---|---|---|---|---|---|---|---|---|---|---|
| HV1 | 187 | 191 | 198 | 196 | 191 | 184 | 200 | 191 | 203 | 192 | |
| **Measurement** | **1** | **2** | **3** | **4** | **5** | **6** | **7** | **8** | **9** | **10** | **s = 6.5 HV1** |
| HV1 | 189 | 185 | 200 | 189 | 190 | 187 | 187 | 190 | 201 | 204 | |
| **Measurement** | **1** | **2** | **3** | **4** | **5** | **6** | **7** | **8** | **9** | **10** | |
| HV1 | 186 | 200 | 192 | 182 | 194 | 188 | 180 | 183 | 185 | 189 | |

Thus, yielding a statistical uncertainty determined by a standard deviation of 6.5 HV 1. In conclusion, a new inline measuring sensor for freeform bending could be established.

### 6.3.4 $HV_{Total}$

HV Total development along the non-tangentially bent and treated surface steel tubes can be seen in Figure 6-6 a,b, while Figure 6-6 c,d give an exemplary overview of the hardness development of non-tangentially bent steel tube 10mm16°. Error bars derived from the standard deviation are also plotted in the diagram.

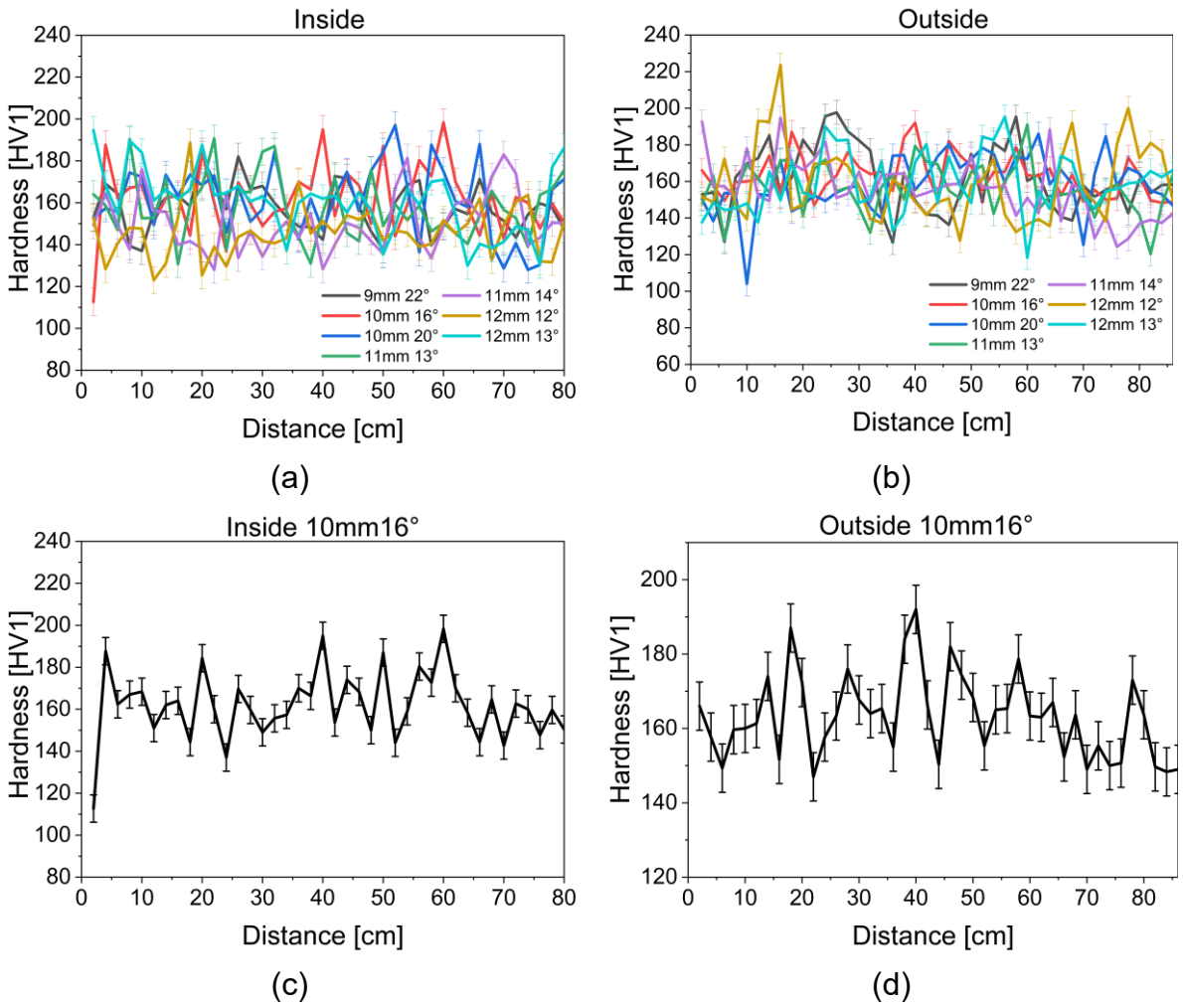


*Figure 6-6: Development of HV 1 hardness total along the (a) inside and (b) outside of the non-tangentially bent tubes (treated surface). (c) Development of HV 1 hardness for non-tangentially bent tube 10mm16° inside (d) and outside.*

As expected, the hardness seen in Figure 6-6 increases slightly where the die is fully deflected, meaning where $\Phi$ is largest, for all non-tangentially bent tubes. Although the measurements scatter, the general trend can be seen. HV 1 measurements lie for inside measurements within an interval of 147 HV 1 to 192 HV 1 and for the outside measurements within an interval of 137 HV 1 and 198 HV 1. It can also be seen that the hardness does not increase significantly for any of the non-tangentially bent tubes, which is also suggested by the conventional stress–strain curves seen in Figure 4-1, showing that the material does not have a pronounced strain hardening behavior.

### 6.3.5 $HV_{Groundstate}$, $HV_{Strain\ Hardening}$ and Plasticity

The results of the tensile tests can be taken from Figure 5-4 (left). Depicted are the conventional stress–strain curves for the tensile tests conducted at room temperature as well as the numerically modelled tensile test. The conventional strains at fracture vary from 0.19 to 0.26. The tensile test shows that the material does not strain harden strongly. Figure 5-4 (left) again shows that the material properties scatter strongly. Sample 10 is an extreme outlier and has a tensile strength value lower by 100 MPa

compared to the rest of the samples. The strong scatter in the material properties is permissible according to the norm [116,117], yet also results in difficulty of precise regression formulation. It is important to emphasize that investigations, especially regarding the fluctuations in the base material, need to be conducted and accounted for in the algorithm.

Using this data and taking hardness measurements in the different conventional plastic strain stages, a relationship between hardness and local strength can be derived in Figure 6-7. The hardness and local strength are plotted against the conventional strain level.

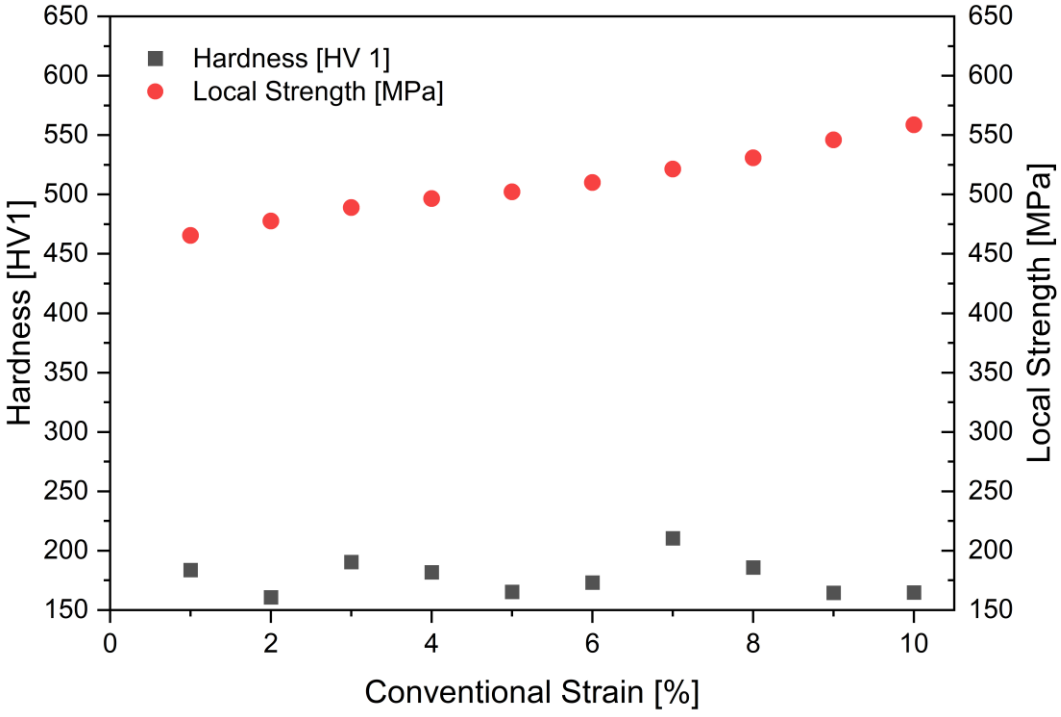


*Figure 6-7: Relationship between hardness and local strength.*

It can be seen that the local strength value does not change by much as the interval lies between 465 MPa and 558 MPa even after the conventional plastic strain level rises up to 10 %. Compared to this, the hardness values scatter in a higher fashion on an interval between 160 HV 1 and 210 HV 1. However, it is noticeable that hardness and local strength differ from each other by a scaling factor. When local strength and hardness are put into proportion, hardness scaled up by a factor of 2.88 on average results in the strength value. This scaling factor is implemented into the soft sensor to inline monitor the local strength.

To assume the relationship between hardness and local strength to be a scaling factor is suitable for a primary approach, as the material does not have a pronounced strain hardening behavior, elastic material behavior is not of interest and it is a well-known fact that base hardness can be reinterpreted as the tensile strength [144]. Further in-

vestigations should be conducted to generate more data. A regression between hardness and local strength should be derived using a material that has a pronounced strain hardening behavior.

To derive the true strain level introduced during bending, the numerical model was utilized. The stopped tensile tests at various conventional plastic strains, 1 % to 10 %, were analyzed regarding the displacement. The displacement points were compared with the simulation to gain insight into the true strain introduced by bending, as the conventional strain does not describe the actual strains in the critical areas because it does not consider the change in cross-section. The following Figure 6-8, shows the conventional strain values plotted against the equivalent plastic strain (PEEQ) values from the simulation. The true strain values from the simulation were then used by the algorithm to predict the true strain level in the bent tube. Figure 6-8 shows that the true strain increases exponentially compared to the conventional strains, as expected.

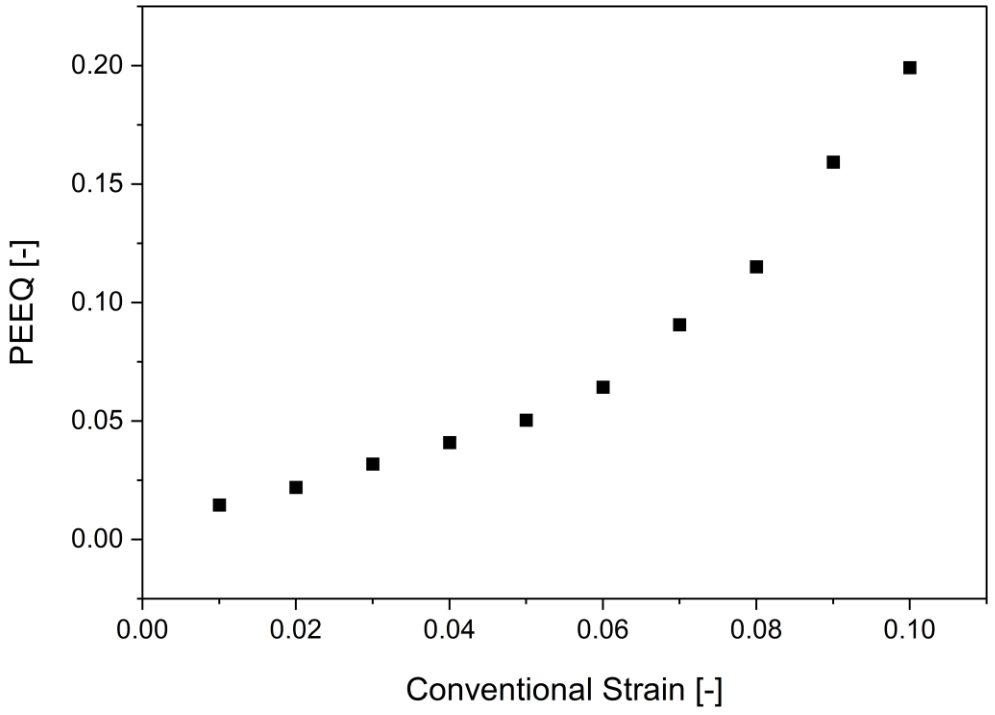


*Figure 6-8: Conventional Strains from tensile tests plotted against PEEQ values from simulation for derivation of true strain level introduced by bending.*

It must be noted that only plasticity levels up to 10 % conventional plastic strain are included. This is due to the fact that beginning at 11 % conventional plastic strain, the test samples start to neck diffusely, meaning necking both in the width and thickness direction occurs [155]. Thus, a uniaxial stress state no longer exists and a multiaxial stress state will be present in the material [29]. To still monitor the local strength and true strains but without any influences due to a change in stress state, only the data before necking is used. This is also permissible, as the bent steel tubes do not neck during bending.

To further improve the filter, tensile tests utilizing Zwicks optical measurement equipment Aramis are anticipated. These will provide meticulous data on the local true strain and can be used to derive a regression between plasticity and hardness directly, which can be implemented into the dynamics matrix of the filter.

### 6.3.6 $HV_{Residual\ Stresses}$

As mentioned in Section 6.2.3.3, the regression between residual hoop stresses and hardness relies on the results in [139]. The chosen regression to inline monitor the residual hoop stresses can be seen in Figure 6-9.

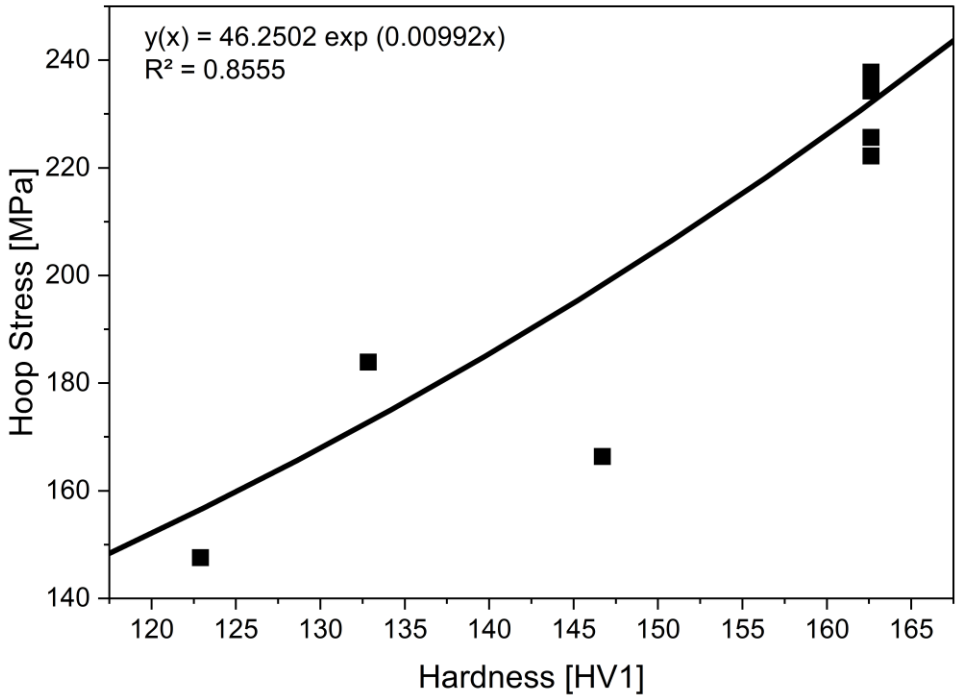


*Figure 6-9: Relationship between hardness and residual hoop stresses derived from results in. Adapted from Ref. [7].*

The regression function selected is:

*Regression Function* $y(x) = 46.2502 \exp 0.00992x$ *Formula 6-9*

This fit offers a coefficient of determination of 0.8555.

The modelling of the residual hoop stresses as an exponential function is also permissible for implementation into the algorithm. The residual of $R^2 = 0.8555$ suggests that the function represents the development adequately. Although a quadratic fit would have led to a higher residual of the regression, the development of the residual stresses was modelled with an exponential fit. The quadratic fit would have suggested that at lower hardness the residual hoop stresses would increase again. That is not the trend shown in [139]. Further data points will be generated for proper validation of the primary exponential fit. Additionally, investigations regarding residual stress influences

on hardness need to be conducted as currently only residual hoop stresses are monitored. Longitudinal residual stresses and radial residual stresses should also be incorporated as they also deter-mine the application of the work piece.

## 6.4 Implementation of Regressions into Soft Sensor

After implementing the regressions into the dynamics matrix and defining the Jacobian thereof, the soft sensor derives local strength and residual hoop stresses as seen in Figure 6-10a,b. For the computation of the algorithm, the algorithm utilizes the hardness values without standard deviation. According to the Kolmogorov-Smirnoff test, the test statistics for measurement uncertainty is normally distributed for $\alpha$=0.05. For the taken test statistic, the true value lies for 95% of all samples in the confidence interval of [188.81; 193.45]. Thus, hardness values without regard to the standard deviation are used in the algorithm, especially as defining interval limits in the EKF may lead to a distortion of the prediction due to the loop nature of the algorithm. Further studies on how interval limits influence predictions are recommended.

The algorithm uses the hardness, calculates the local strength and residual hoop stresses, and runs the EKF. After strength is predicted, the plasticity level will be forecast by scanning the tensile test data. Figure 6-10c shows the prediction of the plasticity level.

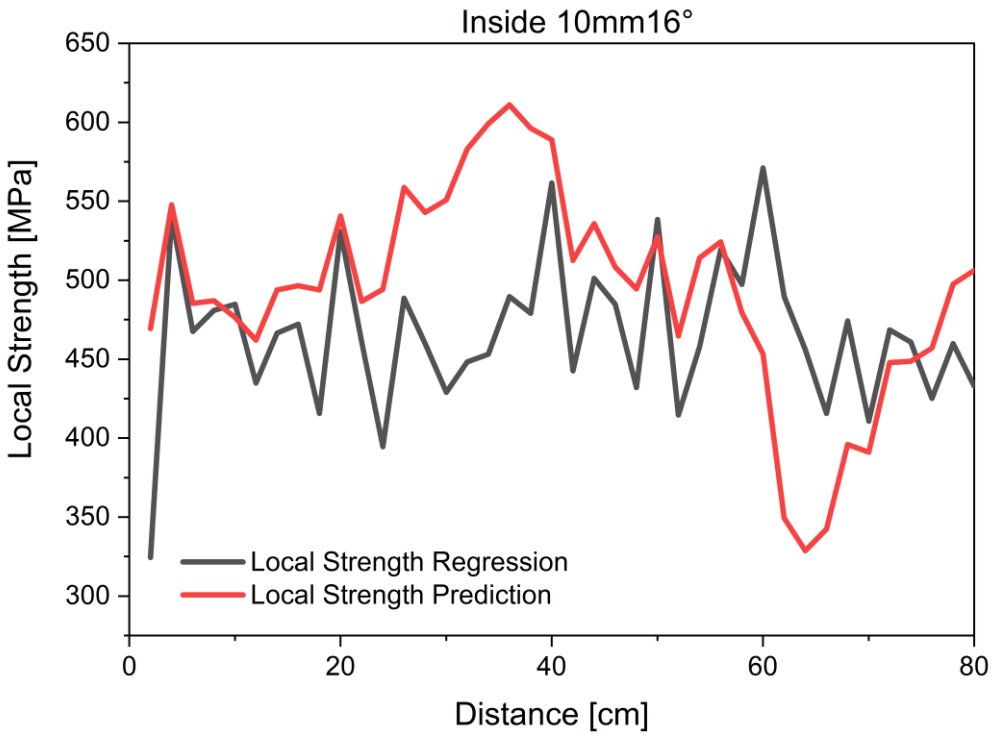
Inside 10mm16°
Local Strength [MPa]
650
600
550
500
450
400
350
300
0
20
40
60
80
Distance [cm]
Local Strength Regression
Local Strength Prediction

(a)

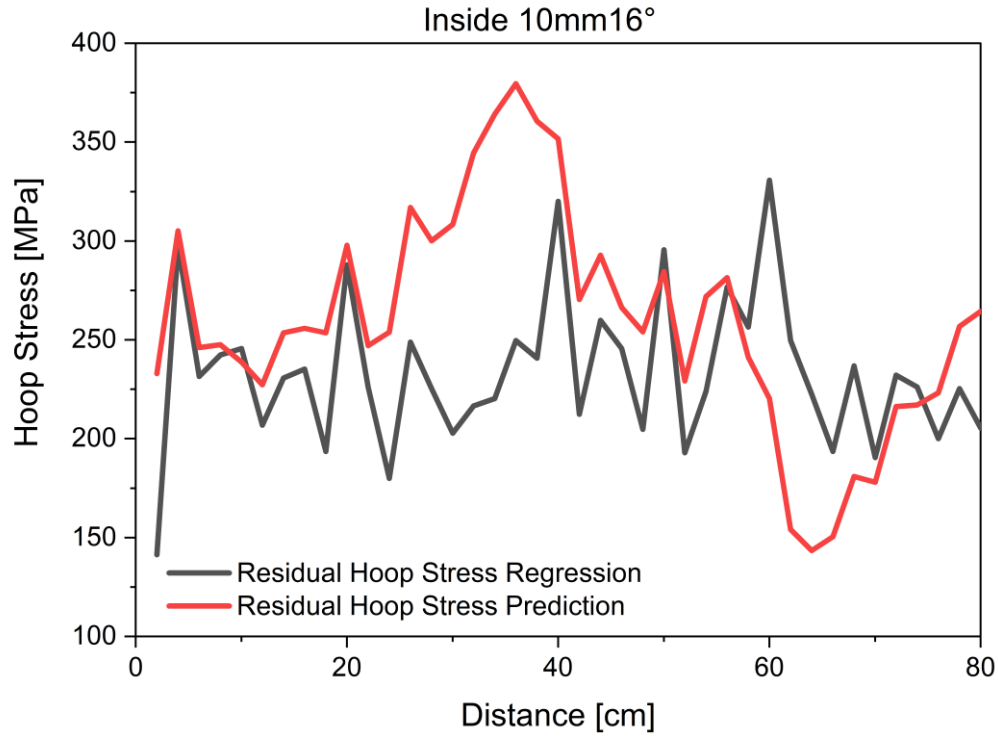
Inside 10mm16°
Hoop Stress [MPa]
400
350
300
250
200
150
100
0
20
40
60
80
Distance [cm]
Residual Hoop Stress Regression
Residual Hoop Stress Prediction

(b)

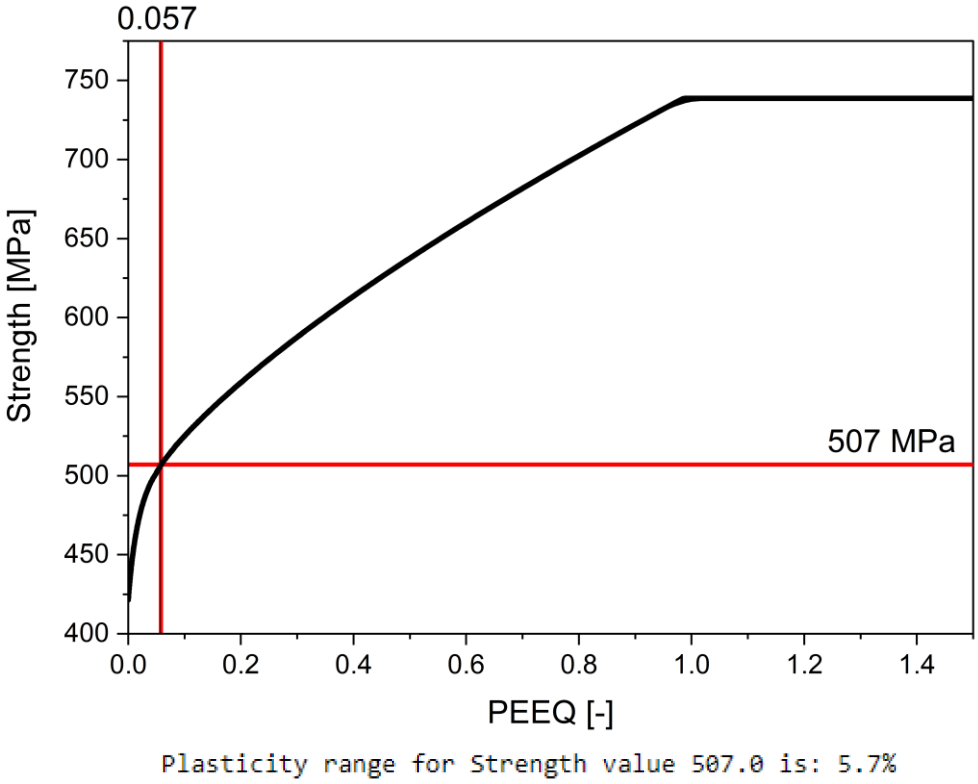


(c)

*Figure 6-10: Development of mechanical properties predicted by EKF; (a) Local strength derivation by regression and prediction; (b) Residual hoop stress derivation by regression and prediction; (c) Derivation of plasticity level in tube through predicted strength from simulation data.*

It can be seen that compared to the measurement values derived by regression, the predictions forecast the same trends. Both local strength and residual hoop stress development is predicted in the same trend as the regression derives. Yet, outliers in the predictions made by the EKF can be seen.

Thus, the current algorithm successfully offers an estimate as well as a prediction of the local strength, residual hoop stresses and plasticity. Yet, further validation is needed. Hence, more mechanical property data in the form of tensile test and residual stress analyses need to be generated. As the current modelling of noise in the EKF is solely dependent upon the taken measurements, further analyses regarding disturbances due to the process will be conducted and modelled in the filter. Furthermore, a detailed characterization of the base material to adequately identify disturbances due to scatter bands in the mechanical properties is anticipated and will be incorporated into the soft sensor. It is also intended to implement error propagation rules into the algorithm to get an even clearer prediction of the mechanical properties. As a model for the initial soft sensor for freeform bending, the EKF has proven to be a suitable algorithm as it linearizes the nonlinear system and can be customized according to preference.

As the material, seen in Figure 5-4, does not have a pronounced strain hardening behavior, strength values do not offer a large range. This can lead to difficulties in deriving the plasticity level later in the algorithm as little change in the local strength suggests a larger interval of plasticity in the algorithm. Further studies, especially regarding the local plasticity level, as mentioned in Section 6.3.5, are intended to incorporate the plasticity level into the EKF.
The greatest advantage of utilizing a correlation scheme based on hardness is that it can be transferred to various kinds of materials. The authors investigated what inline testing equipment can be utilized as a basis for a soft sensor. The most promising approaches were either using micromagnetic BHN sensors or hardness measurements. The authors decided to formulate an initial soft sensor based on hardness measurements, as this does not exclude non-ferromagnetic materials. Yet, additional investigations on the implementation of nondestructive testing results generated by BHN sensors are conducted and will be incorporated into the soft sensor. A disadvantage of the scheme is that for a new material the regressions have to be newly determined, which does take some time to test.

## 6.5 Conclusions

In conclusion, this paper offers an approach for the inline prediction of residual hoop stresses, local strength and plasticity level based on UCI hardness measurements. UCI hardness was validated as a suitable inline measuring system by cross-referencing it with established HV 10 measurements. The results show that an analytic description of residual stresses, local strength and plasticity based on hardness is possible and can be implemented into an EKF for the prediction of material properties. The following insights can be gleaned:

- UCI hardness measurement equipment is now a validated method and offers a flexible, portable measuring solution that can be integrated into the freeform bending machine.
- An analytic representation of residual hoop stresses, local strength and plasticity can be derived from the hardness of the material and serves as the prerequisite for formulation of the novel correlation scheme.
- The novel correlation scheme can be implemented into an EKF now, enabling an in-line prediction of mechanical properties during freeform bending.

It must be noted that further studies, especially regarding disturbances in the process and material, as well as error propagation, are conducted and will contribute to the design of the soft sensor. Additionally, micromagnetic BHN sensors will be integrated into the process to obtain more information, namely on changes in microstructure during the freeform bending process. This will give further insights into the change in hardness and residual stresses during bending. Furthermore, longitudinal residual stress and radial residual stress predictions will be implemented for inline prediction.

As this is a novel approach to monitoring mechanical properties during freeform bending, no comparative studies on the algorithm can yet be given. This will be the topic of further studies, as different algorithms are planned to be implemented for the freeform bending process.

## 6.6 Conclusion and Evaluation of Results

This chapter lays the basis for a soft sensor for freeform bending with movable die. To do so, UCI hardness measurements are firstly established as a suitable inline measurement equipment even for untreated surfaces based upon which relevant parameters may be derived. Initially, the UCI method is compared with the HV 10 method using a Bland-Altman plot, which is a statistical method to investigate the concordance between two results. This is done to examine whether the HV 10 measurement method can be substituted by UCI measurements, as HV 10 measurements cannot be taken inline. It can be concluded that the UCI measurements are in concordance with HV 10, thus UCI measurements can be applied.

Furthermore, surface roughness as an influencing parameter during UCI measurements was examined. UCI hardness measurements on both polished and unpolished surfaces of the round tubes were conducted, and it is observed that the surface roughness does have an influence on the measurement, however, significantly small such that for future works surface roughness effects can be neglected.

Continuing, this chapter investigates whether parameters of interest, namely local strength, plasticity and residual hoop stresses can be deduced from hardness measurements. It is hypothesized, that hardness is closely related to the local strength of the material as well as the residual hoop stresses. To understand the relationship between hardness, local strength and plasticity, tensile tests, UCI hardness and numerical simulations were performed. As the material shows no pronounced strain hardening effects, a scaling factor allowing the derivation of local strength from UCI hardness is deduced. After prediction of the local strength, the plasticity level can be derived determined from the tensile tests. Additionally, the relationship between hardness and residual stress, based on findings introduced in Chapter 5.3, is implemented into a regression model offering an acceptable coefficient of determination of $R^2$=0.8555. Both relationships are highly material dependent, however, which means that for a new material, the same, elaborate methodology must be followed as the previously determined models are not transferrable.

Lastly, based on the established regressions between hardness, local strength and residual hoop stresses, this chapter proposes a soft sensor based on an EKF that can derive local strength, residual hoop stresses and plasticity levels induced into the material during bending, which takes measurement noise into account. Yet, process noise is not yet implemented into the EKF, which would further enhance the accuracy of

predictions, however making modelling also increasingly complex. Therefore, an assessment of the added value with regard to modelling complexity of all disturbance variables in comparison to safety should be investigated.

Overall, this chapter introduces an inline-measurement as well as prediction tool for estimating relevant mechanical properties during the bending process. This allows a more efficient design of the process as a closed-loop control based on mechanical property predictions can now be formulated.

However, residual axial stresses will further need to be taken into account during the bending process, as they especially determine further processing steps after bending. Hence, the following Chapter 7 introduces an extension of the proposed soft sensor by residual axial stress predictions based on BHN measurements.

# 7 Extension of Soft Sensor by Residual Stress predictions based on Barkhausen noise measurement

A soft sensor for freeform bending with movable die is now implemented, however, this does not yet take residual axial stresses into account. Yet, residual axial stresses oftentimes cause significant distortion of the component if the equilibrium is disturbed, be it due to cutting or welding activities, which are oftentimes used in the process chain following freeform bending. Thus, it is detrimental to have a quantitative estimation of the residual axial stresses within the investigated steel tubes, as this enables the adjusting of the residual axial stresses to guarantee good manufacturability of the components after bending.

Hence, this chapter introduces an extension of the soft sensor introduced in Chapter 6 in deriving residual axial stresses based on BHN analysis. To do so, the relationship between measured BHN and the state of interest (residual axial stress measured by XRD measurements) is investigated and implemented into a static, non-linear state space model. This in turn allows a prediction of the residual axial stress state in over- and underbent tubes, while simultaneously establishing a methodology for a quantitative derivation of residual axial stresses based on BHN analysis. Usually, BHN analysis is used for a qualitative statement regarding residual stress state within the material as there are a manifold of influencing parameters that affect the signal intensity, making a sole investigation of one parameter of interest complicated. However, this study discovered, that with a change in residual stress state the geometry of the measured signal varies. This relationship is explored and finally allows a quantitative derivation of the residual axial stress state. The following chapter firstly introduces the methodology of XRD-measurements for residual stress determination followed by the utilized BHN measurement equipment. Then a sensitivity analysis of the measurement settings of the BHN equipment that are in turn used for measurement and the signal evaluation is presented, followed by the signal processing methodology. Last but not least the correlation of residual axial stresses with BHN is provided that is in turn implemented into the static, non-linear state space model.

## 7.1 XRD-measurement settings for correlation

To quantitatively correlate residual stresses with the BHN measurements, the residual stresses need to be determined. As the BHN measurements will be taken on specific locations on the tubes with limited penetration depth, a method needs to be chosen, that will take measurements near the surface as well. Hence, the choice was set to XRD measurements using the $\sin^2\psi$ method, which are based on Bragg's equation. The method allows the quantitative measurements of lattice strains and enables the determination of spatially specific stress information [143].

XRD stress analyses for quasi-isotropic and polycrystalline materials is based on the determination of lattice strains and is reliant on the identification of lattice plane spacing $d^{\{hkl\}}$ according to Bragg's Law using the basic principles of elasticity theory.

$$n\,\lambda = 2\,d^{\{hkl\}}\sin\theta^{\{hkl\}} \qquad \text{Formula 7-1}$$

Where $\lambda$ is the wavelength of the radiation, $n$ a natural number of the diffraction order of the interference and $\theta^{\{hkl\}}$ the Bragg angle [143].

Based on this knowledge, residual stresses may be determined as they influence the interplanar spacings $d^{\{hkl\}}$. If a material is in tensile state, then the distances in the interplanar spacings perpendicular to the tension are increased, while the lattice planes parallel to the tension are compressed. As residual stresses impact the interplanar distances, thus also the diffraction angle, the lattice extension ε can be determined in measuring the change of the diffraction angle [143].

For a better understanding of the measuring principle Figure 7-1 is be used.

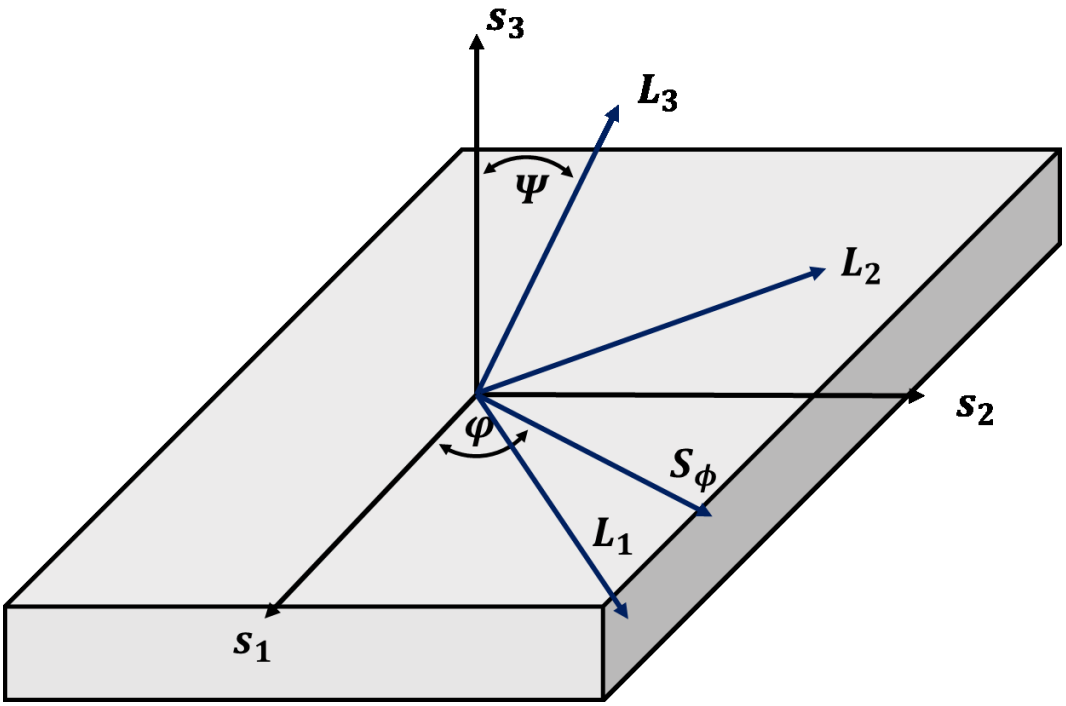


*Figure 7-1: Schematic depiction of the definition of angles for stress analysis using XRD.*

With:

| | |
|---|---|
| $S_1$, $S_2$ | Axes in the plane of the sample, $S_1$ is determined by the tester |
| $S_3$ | Axes perpendicular to the surface of the sample |
| $L_1$, $L_2$, $L_3$ | Laboratory coordinate system where $L_3$ is the normal of the diffracting lattice plane (hkl) and the angle bisector between the incoming and diffracted x-ray |
| $\varphi$ | Angle between a fixed direction in the specimen's surface and the projection of the normal of the diffraction planes |

| | |
|---|---|
| Ψ | Angle between the normal of the sample surface and the normal of the diffraction planes |
| Sϕ | Direction within which the stresses $\sigma_\varphi$ and $\tau_\varphi$ are measured |

Based on the elasticity theory, the following equation applies to the strains in direction determined by angles $\varphi$ and Ψ of macroscopically isotropic crystalline materials under the assumption that penetration depth of the x-rays is limited and $\sigma_{33} = 0$.

$$\varepsilon_{\varphi\Psi}^{\{hkl\}} = S_1^{\{hkl\}}[\sigma_{11} + \sigma_{22}] + \frac{1}{2}S_2^{\{hkl\}}[\sigma_{11}cos^2\phi + \sigma_{22}sin^2\phi + \tau_{12}sin2\phi]sin^2\Psi + \frac{1}{2}S_2^{\{hkl\}}[\tau_{13}\,cos\,\phi + \tau_{23}\,sin\,\phi]\,sin2\Psi \quad \text{Formula 7-2}$$

Where:

| | |
|---|---|
| $\varepsilon_{\varphi\Psi}^{\{hkl\}}$ | Strains in the direction defined by the angles $\varphi\ and\ \Psi$ for the lattice plane $\{hkl\}$ |
| $S_1^{\{hkl\}}$ and $\frac{1}{2}S_2^{\{hkl\}}$ | Elasticity constants for the lattice plane $\{hkl\}$ |
| $\sigma_{11}, \sigma_{22}$ | Normal stresses in $S_1$ and $S_2$ directions |
| $\tau_{12}, \tau_{13}, \tau_{23}$ | Shear stresses in the planes determined by $S_1$, $S_2$ and $S_3$ |

The tested samples were both in the unbent as well as the over- and underbent state. Sections of 5 cm were cut from the tubes for investigation. All testing was conducted with a Seifert 3003 PTS (GE Inspection Technologies, New York, NY, USA) machine using a Cr X-Ray tube. The intensity distribution of Cr-Kβ X-rays was recorded in the measuring range of 40°<2θ<165° with a counting time of 20 s and a step width of 0,05°. The resulting X-ray patterns were characterized and analyzed using Materials Analysis Using Diffraction (MAUD) software. The Fe-bcc [211] peak at 2θ ≈ 156,08° was chosen for residual stress analysis, with elasticity constants $S_1^{\{hkl\}} = 1.25\ x\ 10^{-6}$ MPa$^{-1}$ and $\frac{1}{2}S_2^{\{hkl\}} = 5.76\ x\ 10^{-6}$ MPa$^{-1}$. Using Formula 7-2, the residual stresses were determined in conducting an elliptical fitting to the measurement points.

Initially, it must be established how deep the penetration depth of the XRD-measurements are. This is a complicated endeavor, as the penetration depth varies with different angles of incidence. However, in general it is assumed, that XRD-measurements taken on steel samples have a penetration depth of about 10 µm [156]. Overall, there were 48 measurements taken on the over- and underbent tubes – 22 measurements were taken on the unbent while 26 measurements were taken on the bent tubes. The measurements taken in unbent state can be seen Figure 7-2 (a), while the measurements taken on the bent tubes can be seen in Figure 7-2 (b).

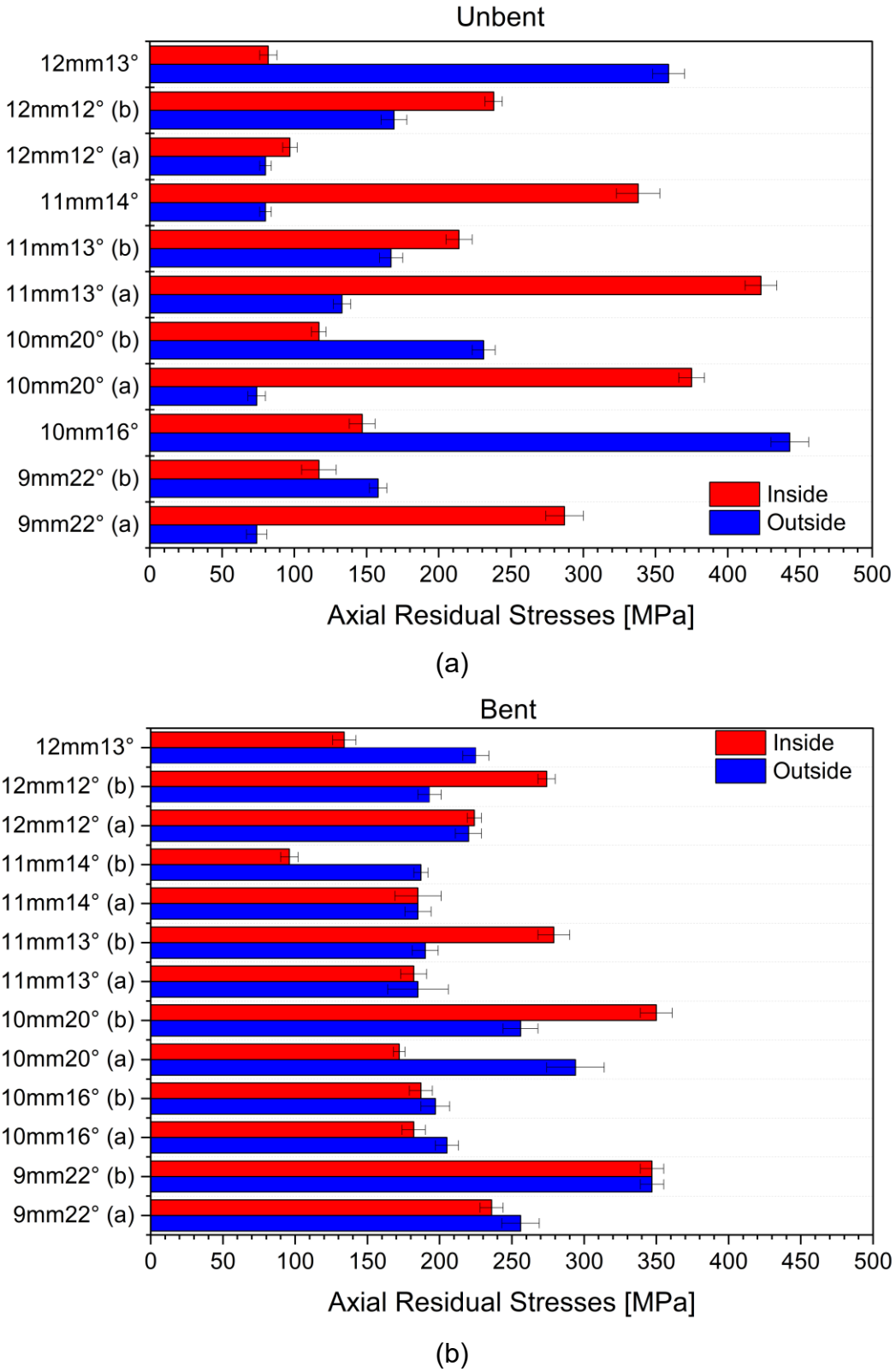


*Figure 7-2: Residual axial stress distribution in the over- and underbent tubes; (a) unbent state; (b) bent state.*

It can be observed that in the unbent state, the residual axial stresses vary between 74 MPa and 443 MPa. The denotation of inside and outside in the unbent state is not relevant in the general overview of the residual axial stresses, however it is essential

for observing the development of the residual axial stresses in the initial state i.e. the unbent state and the final, bent state in order to propose the static, non-linear model, see Chapter 7.5. The observation of strongly varying residual axial stresses in the unbent tube again emphasizes the importance of an inline-surveillance option to monitor residual axial stresses, as the residual axial stress state is essential for further production steps such as to prevent distortion. It can furthermore be seen, that on the outside circumference of the tube, the residual axial stress state is of tensile nature. This is plausible, even though the tube is unbent, however, residual axial stresses during the forming process of the tube itself were introduced. Tension on the outside of the tube is thus to be anticipated.

When analyzing the residual axial stress state within the bent tubes, the stresses are more evenly distributed. Again, all stresses are of tensile nature. This is especially noteworthy for the inside, meaning the rather compressed area of the tubes. The overall residual axial stresses vary between 96 MPa and 350 MPa, resulting in a more favorable stress state after inducing plasticity as they are lower than in the unbent state, particularly with regard to the yield stress of the material at about 450 MPa. Furthermore, these results validate, the successful decoupling of the final geometry of the bent tubes and the mechanical properties, notably the residual axial stresses, making a closed-loop control structure possible that can manipulate the actors of the machine so that a desired residual axial stress state can be introduced while the predefined bending geometry may still be maintained.

## 7.2 Barkhausen noise – QASS µmagnetic

The BHN measurement equipment utilized in this study is the QASS µmagnetic, developed by QASS GmbH. BHN is induced by the excitation field, hence the chosen magnetizing parameters can affect the BHN signal significantly. Furthermore, as BHN is the discontinuity during magnetization due to the interaction of the domain walls within the observed material and the microstructure of the material, BHN is also strongly influenced by microstructural parameters, such as grain size, dislocation density and so on, as they influence the domain wall motion. Meaning mechanical properties such as residual stresses and hardness influence the BHN as they also entail a change in the microstructure of the material.

Stresses in particular influence magnetic properties, i.e. BHN. This is tightly tied to the so-called phenomenon of magnetostriction, which refers to the change in dimensions when a material is exposed to a magnetic field. This change occurs due to the in Chapter 2.1.5 described motion of the domain walls. Due to magnetostriction, when a stress is applied to a material, the stress influences the domain structure and creates a source of a novel magnetic anisotropy, which will influence permeability and remanence of the investigated material [44]. Investigations have shown that in materials with positive magnetostriction, which is the case for steels at low fields, as was tested in this work

[44], an increase in tensile stresses will lead to an increase in permeability as well as magnetization in the negative saturation magnetization of the hysteresis, whereas a decrease in the permeability and magnetization can be seen in the positive saturation magnetization. Furthermore, the coercive field and thus the energy loss in the same field will decrease [157]. Thus, it will be seen in the BHN signal, specifically in the shape of the hysteresis curve which is reflected in the QASS measurement signal.
The experimental setup of the QASS µmagnetic measuring system consists of a measuring computer, power amplifier and the sensor with an integrated preamplifier, see Figure 7-3.

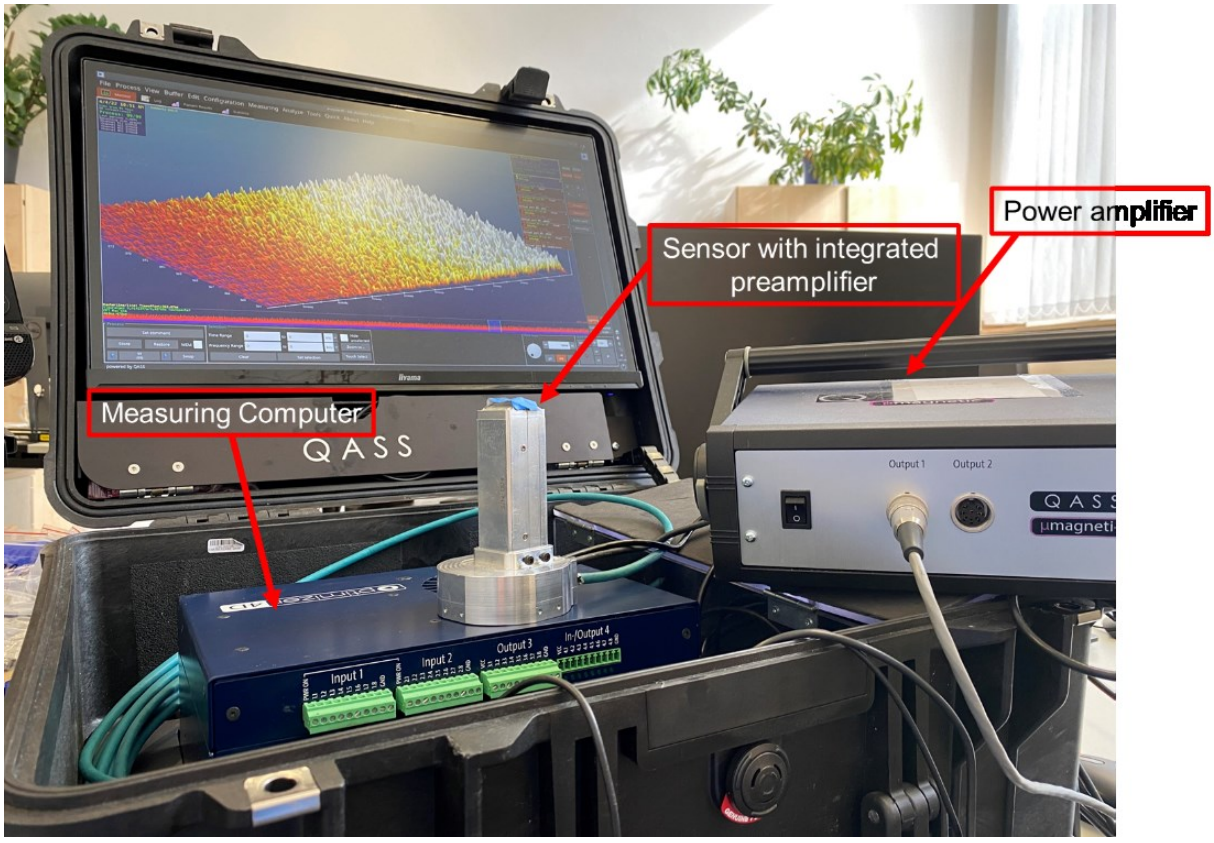


*Figure 7-3: Set-up of the QASS µmagnetic measuring system; relevant parts marked.*

Via the interfaces on the measuring computer the power amplifier and sensor are connected to the computer. The measuring system utilizes the magnetic BHN analysis in combination with an exceptionally high sampling rate and a real-time spectral analysis to qualitatively monitor changes in the microstructure of ferromagnetic materials. The measurements themselves are conducted across an airgap. To assure that the airgap is at a constant distance the sensor head is covered with a layer of coating. The measuring computer is, additionally, equipped with a unique software where all relevant settings for the measurements are communicated. The adjustable parameters are listed in the following Table 7-1:

*Table 7-1: Adjustable parameters in the QASS μmagnetic measuring system and the finally chosen measuring parameters*

| **Parameter** | **Function** |
|---|---|
| Amplitude of BHN [mV] | Can be set to multiples of 64 [mv] up to 955 [mV] |
| Frequency [Hz] | Customizable according to material and wished penetration depth |
| Amplification | Sets the amplification of the preamplifier |
| Fast Fourier Transform | This enables the system to perform a Fast Fourier Transformation (FFT) of the signal to convert the time-amplitude signal into a time frequency amplitude signal; the original time-amplitude signal can also be recorded and displayed |
| Sample rate and FFT-oversampling | The oversampling enables the system to generate further samples and determines along with the sample rate how many spectra are generated, e.g. sample rate = 2MHz = 2x106 Hz and oversampling = 4 leads to: (2 x 106 Hz x 4) / 1024 x 103 Hz = 7812,5 spectra/s. Due to the Fourier Transformation the term needs to be divided by 1024 as these are the Fourier sampling points of the system. |
| FFT Logarithm | The FFT-logarithm weights high-frequency and low-frequency signals differently. The lower the chosen value, the more dominant the low-frequency signal components appear. |

The setting of the measurement parameters is strongly dependent upon the characteristics of the material. This entails that the settings regarding frequency and amplitude in the equipment to generate the magnetic field must be selected carefully. It must be ensured that no magnetic saturation occurs during the measurement, but also that the measurement signal is stable as well as processable.

A key part is to find a suitable frequency. According to Faraday's Law, the induced voltage of the signal $U_{ind}$ is proportional to the rate of change in the magnetic induction [158].

$$U_{ind} = -\frac{d\phi}{dt} = -nS\frac{dB}{dt} \qquad \text{Formula 7-3}$$

In which $n$ is the number of coil turns, $S$ the area of the sample cross-section and $B$ the magnetic flux density of the excitation field. From Formula 7-3 it can be inferred that especially the magnetic flux density and the frequency influence the BHN. To choose the right magnetization frequency, two points must be kept in mind: Firstly, based on Faraday's law (Formula 7-3) assuming that the cross-section $S$ stays constant, the induced voltage of the signal $U_{ind}$ is positively correlated to the frequency of the excitation magnetic field $\frac{dB}{dt}$ meaning frequencies that are too low can lead to low BHN energy levels, which negatively influences evaluation of the BHN hill symmetry. Secondly, it needs to be guaranteed that the excitation magnetic field penetrates the

material and magnetization occurs in the sample region under the sensor. The magnetic field obeys the wave equation when a flat sinusoidal electromagnetic wave attenuates on a laminar surface [87]:

$$\nabla^2 H - \sigma\mu\frac{\partial H}{\partial t} - \varepsilon\mu\frac{\partial^2 H}{\partial t^2} = 0 \qquad \text{Formula 7-4}$$

With $\mu$ being the permeability of the material, $\varepsilon$ the electrical permittivity, $\sigma$ the electrical conductivity and $H$ the intensity of the magnetic field. The solution leads to:

$$B = B_0 \exp[i(az - \omega t)] \exp(\frac{-z}{\delta}) \qquad \text{Formula 7-5}$$

Where $z$ is the position at which $B$ was measured, $\omega$ the wave frequency and $\delta$ the penetration depth. Here, the amplitude of the wave decreases to $\frac{1}{e}$, where e is the Euler constant, and penetration depth is defined as:

$$\delta = \sqrt{\frac{2}{\omega\sigma\mu_0\mu_r}} \qquad \text{Formula 7-6}$$

It can be observed that the penetration depth is inversely proportional to the wave frequency. Thus, the frequency must be chosen such that the penetration depth of the magnetic BHN measurements will be in congruence with the penetration depth of the subsequent XRD measurements. An estimation of the penetration depth of the BHN measurements is given in the next section, after identification of the ideal measurement settings. It must be mentioned, that due to the various amplifying as well as measurement settings, the BHN results cannot and are not given a defined energy SI-Unit. The following chapters will refer to the measured energy levels with the unit “QASS Unit” [QU]. However, the results for one steel grade are comparable and can be used for the qualitative as well as quantitative description of the mechanical properties as all the settings are kept constant between the measurements and can be kept constant for one steel grade.

## 7.3 Optimal measurement settings and methodology for data extraction from signal

BHN analysis is very susceptible to the microstructure evolution, meaning that macrostructural occurrences dependent upon the microstructure evolution such as hardness and residual stress state have a significant impact upon the BHN signal. During forming processes, the component not only hardens but also shows a significant redistribution of residual stresses. However, as this entails a superposition of effects, a sole investigation of the signal intensity cannot be recommended. Literature [159] though suggests, that the residual stress state in the materials influences the geometric characteristics of the hysteresis curve. This is also seen in the geometry of the QASS µmagnetic measurement signal. Hence, to quantitatively derive residual stresses from BHN,

both the geometry and intensity of the signal is used. Thus, this chapter investigates optimal measurement settings for further signal processing.

The parameters that may be varied in the QASS µmagnetic measuring system are listed in Table 7-1 and were adjusted for the sensitivity analysis as followed: the amplitude of BHN [mV] was quantized in steps of 64 mV as predefined by the software, frequency [Hz] in steps of 100 Hz up to 1.5 kHz, Amplification from 500:1 up to 5000:1 in steps of 100, sample rate from 30 kHz up to 4 MHZ also as predefined by the equipment and oversampling from “no oversampling” up to 64:1 during measurement. All testing was performed on P235 TR1 tube material, unbent and results were investigated regarding their suitability for evaluation of signal intensity as well as symmetry characteristics.

After the BHN measurements are conducted, the raw data is to be processed. For basic processing, the data parsing python scripts from the developer QASS are utilized. The built-in measuring frequency in the QASS µmagnetic lies within the range of 1-512 Hz, resulting in vast amount of data. Thus, using the parsing script, the data is compressed by a “compression ratio” that sums up data across the defined ratio. In this study, the compression ratio was set to 8, meaning that the frequencies lying between 1-8Hz, 9-16Hz and so on, are summed up for each 8 frequencies, leaving the raw data of 512 Hz to be separated into 64 groups. As the variation of BHN with respect to time is to be investigated, the python array indices containing the data are converted into a time series. However, noise is still an issue. To minimize noise, the hill-shaped signals across the frequencies are added together. In doing so, the to be assumed random noise approaches zero and the BHN signal is strengthened. As shown in Figure 7-4 the processed signal results in two triangularly shaped hills.

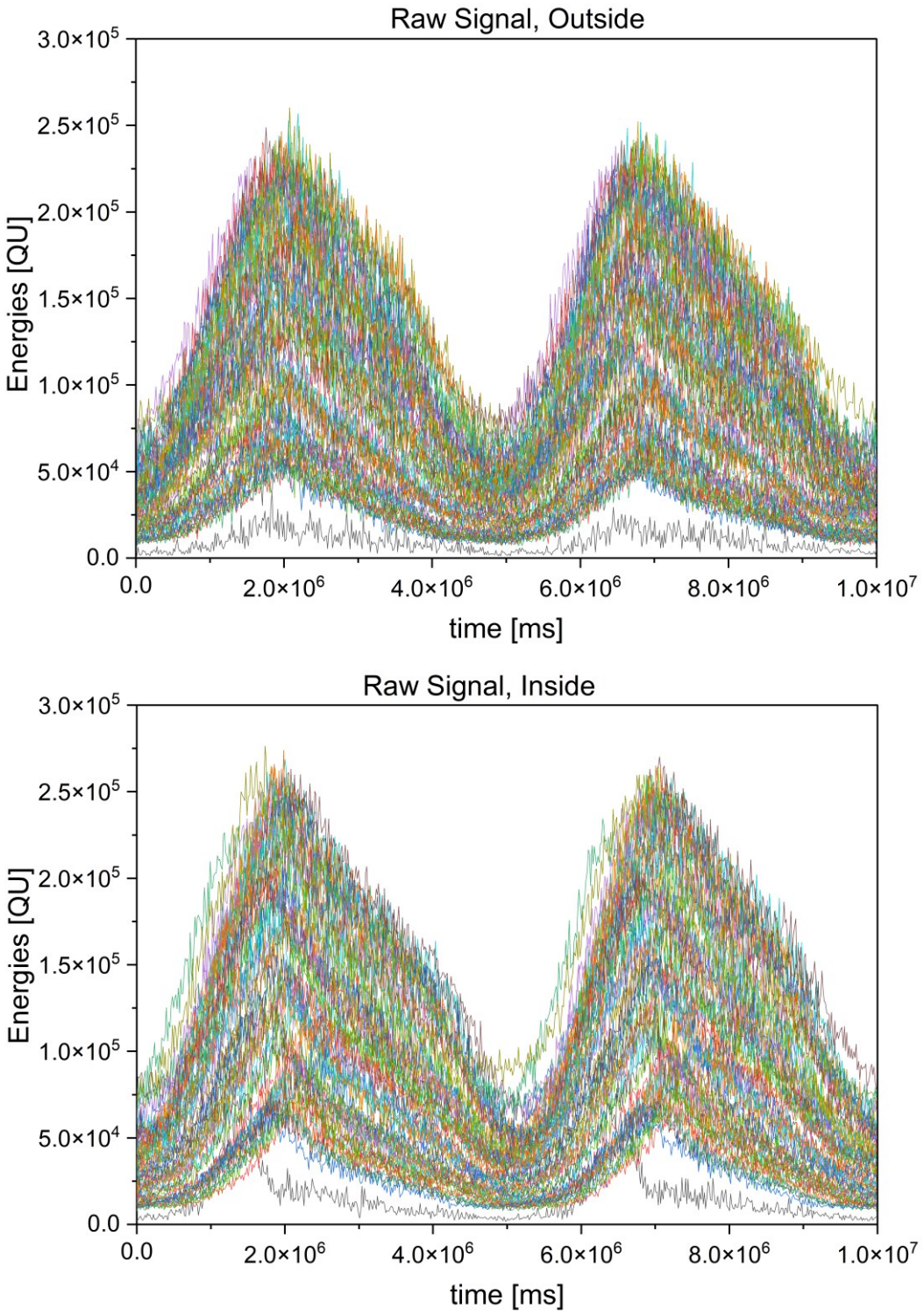


*Figure 7-4: Through python script processed, raw signal taken on 10mm16° tube in point of maximum deflection.*

Both hills together depict the integration of the hysteresis loop that was traversed due to the magnetic field. Due to that fact, symmetry effects that occur in the hysteresis loop can also be seen in the hill-shaped signal, making a geometric evaluation of the signal appropriate. As previously mentioned, the signal itself cannot be given the SI-unit [A/m] as the raw signal is manipulated utilizing filters and amplifications, that are

dependent on the investigated material. This means that a comparison of measurement signals among different materials is not logical, however, comparing the signal for one material is valid and appropriate. Ultimately, this work will refer to the term “QASS unit” [QU] when describing the signal intensity.

To suppress possible background noise in the signal entirely, a high-pass filter at about 5-10 % of the peak intensity in the signal is defined, see Figure 7-5 (a). Only the measurements above this high-pass filter will be processed for symmetry characteristics. Next, the contours of the hill-shaped signals are extracted and are evaluated regarding their extent of asymmetry. Even though, background noise is now successfully suppressed, local noise and vibrations in the contours are visible, Figure 7-5 (a). These, however, complicate the evaluation of the symmetry characteristics. Hence, the contours of the signal are processed by mean smoothing, meaning the value of the signal is replaced by the mean values of the signal nearby. This work utilizes a mean smoothing kernel size of five. Thus, each value of the signal is replaced by the mean value of its preceding two as well as following two values. The smoothed signal can be seen in Figure 7-5 (b).

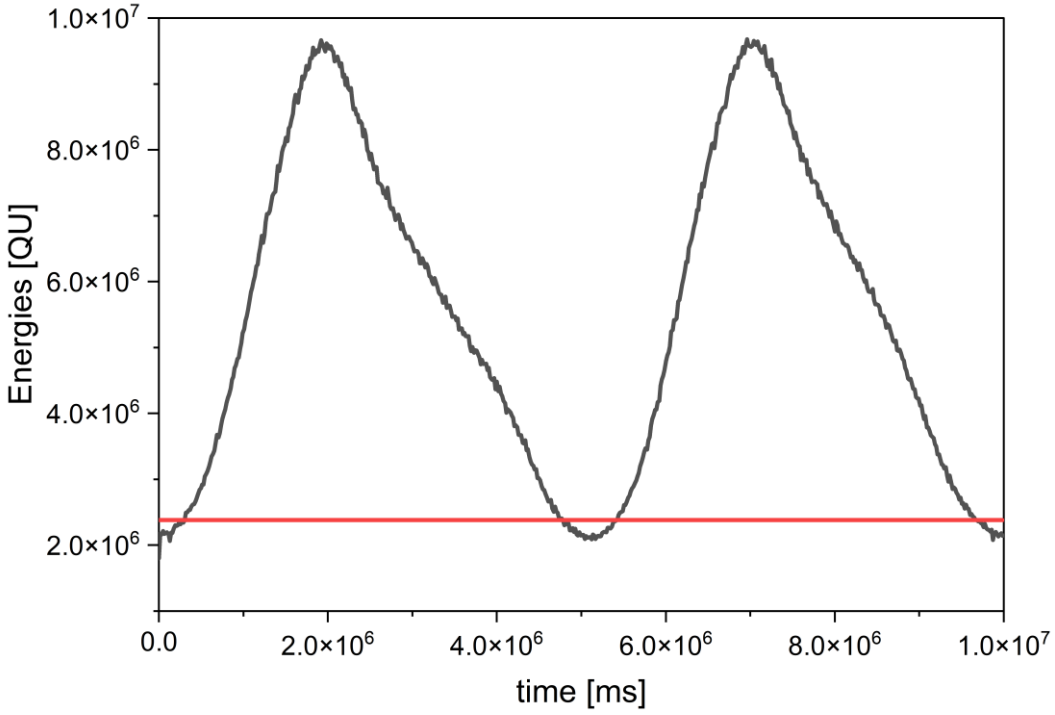


(a)

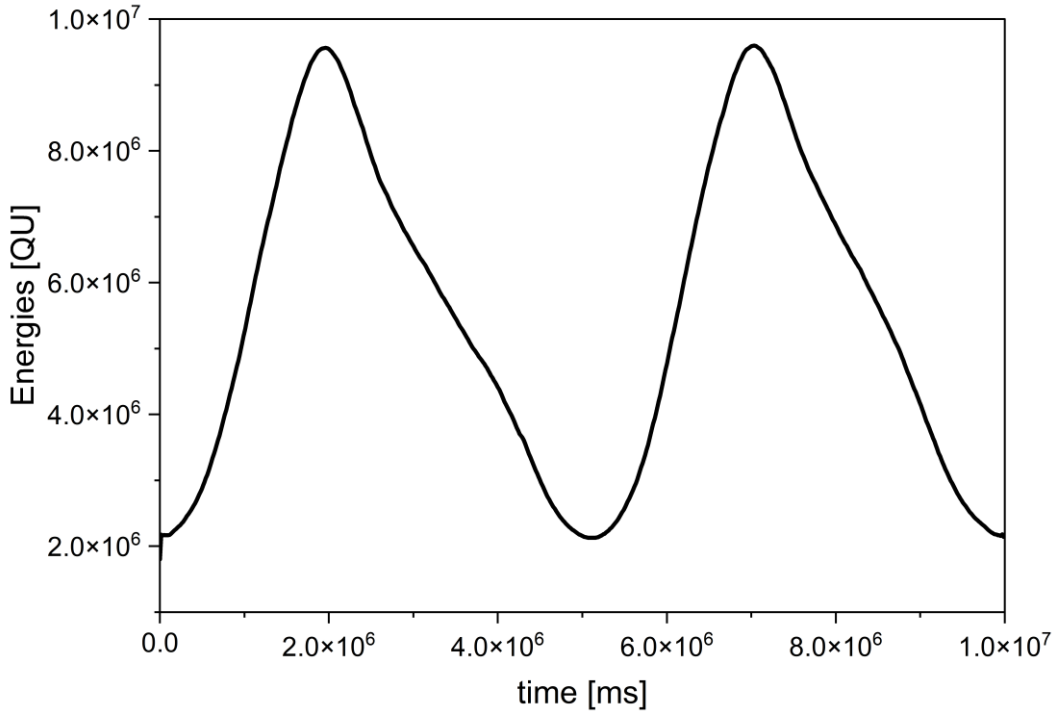


(b)

*Figure 7-5: a) Extracted and unsmoothed signal with defined high-pass filter; (b) extracted and smoothed signal.*

Lastly, the symmetry characteristics are processed using something this work will refer to as Symmetry Factor (SF). The smoothed signal above the high-pass filter is evaluated using the following equation:

$$SF = \frac{t_{max} - t_{center}}{l}$$ Formula 7-7

With $t_{max}$, $t_{center}$ and $l$ being the maximum point in the signal, the center point of the signal and the length of the bottom line above the high-pass filter. Figure 7-6 shows the evaluation using SF, where a left-skewed signal is negative, a symmetrical signal is zero and a right-skewed signal positive.

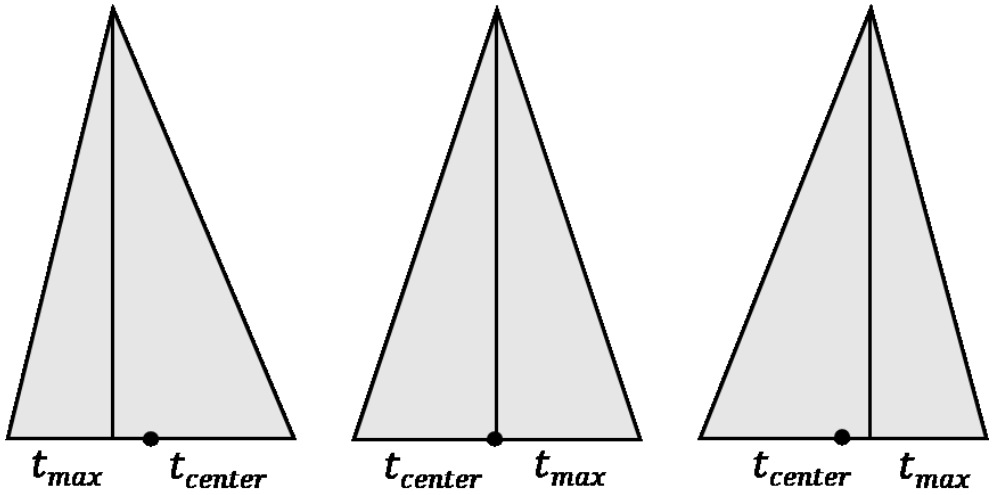


*Figure 7-6: Schematical Depiction of the SF evaluation; left-skewed, symmetrical and right-skewed.*

During the systematic variation of the different measurement settings, it was observed that a variation of the oversampling as well as sample rate in most combinations led to very poor measurement results on the P235 TR1 where data processing was made impossible. Furthermore, setting the BHN amplitude to higher energies than 466 mV led to magnetic saturation, meaning the intensity of the signal plateaued. Hence, amplitudes above 466 mV are also ruled out for further processing. The parameter frequency showed, that with an increase, the signal intensity led to good results, however the detected BHN hill symmetry became very irregular, which led to an exclusion of high frequencies as that would require the signal to be smoothed strongly, thus distorting the measurement result significantly. The higher the chosen amplification, the higher the signal intensities, however at high amplifications the SF evaluation showed that both SF left and right did not differ much from zero, making it a poor choice for correlation to residual stresses. The most robust and steady results using the prototype sensor from QASS µmagnetic were ultimately identified to, see Table 7-2:

*Table 7-2: Settings of measurement equipment for P235 TR1*

| Amplitude [mV] | Frequency [Hz] | Amplification | FFT-transform | Sample rate [MHz] | Oversampling | FFT-log |
|---|---|---|---|---|---|---|
| 255 | 100 | 2000 | On | 0:4 | 3:8 | Off |

When conducting the BHN measurements with the determined settings, it could be observed, that the measurements taken by hand and offline show very good stability. The standard deviation of the measurements previously determined lies at $3{,}61 \times 10^4$ QU. Hence, inline-suitability of the BHN measurement equipment is given. To estimate the penetration depth of the utilized sensor apparatus using the measurement setting parameters seen in Table 7-1, Formula 7-6 using the skin effect is used. The penetration depth is estimated to lie at around 400 µm. Higher magnetizing frequencies such as 1000 Hz led to measurements being taken closer to the surface, however, signal processing especially regarding the evaluation of symmetry characteristics is impossible at higher magnetizing frequencies, as the measurement becomes too noisy. It must be noted that the penetration depth of the BHN and XRD measurements differ to some extent, however the correlation is still proposed, as an alternative BHN measurement settings was not feasible, especially with regard to signal stability and processing possibilities, also the correlated residual stress measurements are of type I, meaning macroscopic stresses that are valid for larger regions within the material.

## 7.4 Barkhausen noise measurement evaluation

After identification of the best measurement settings, BHN measurements were conducted on over- and underbent material. A typical raw signal of the conducted BHN measurements can be taken from Figure 7-4. After first visual inspection of the raw signal, it can already be seen, that the BHN hills are not symmetrical, but rather left-skewed, making an evaluation of the symmetry characteristics plausible and auspicious, as well as a good preliminary tool for residual stress evaluation, as it was observed in all measurements that the stronger the left-skewedness of the measuring signal, the higher the tensile stress state within the tubes.

Figure 7-7 depicts the measurements of BHN signal intensity as well as the derived SF for the inside, bent tubes. Generally, it can be said that the higher the detected energy in the measurement position, the lower the SF. Thus, a largely inversely proportional relationship between the signal intensity and symmetry characteristics can be inferred.

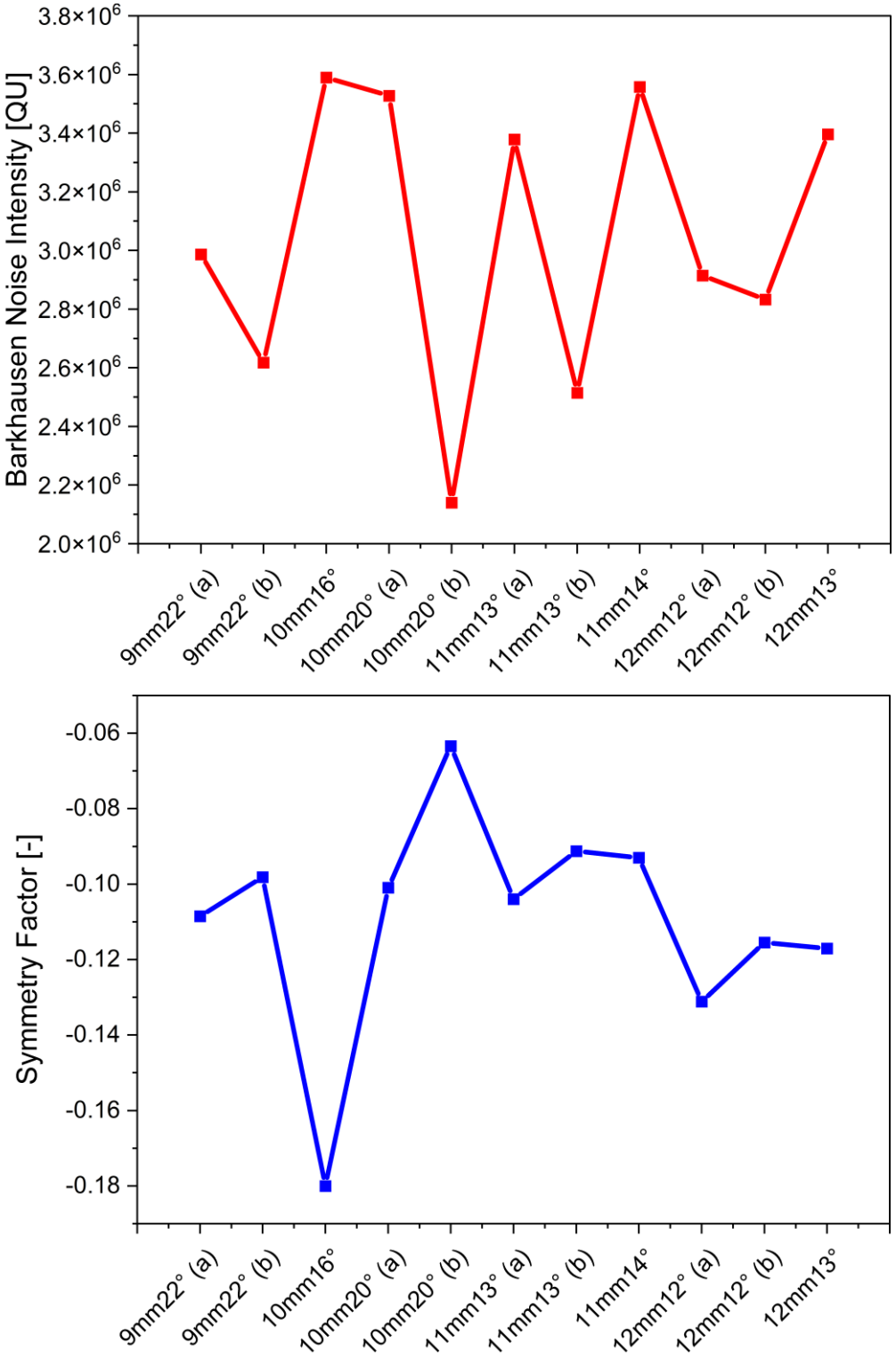


*Figure 7-7: Exemplary extracted energies in QASS Units [QU] and SF on inside, bent tubes.*

From Figure 7-7 it can be deduced, that signal intensity alone is not a suitable parameter to derive the residual axial stress state in the tubes, as even tubes with similar residual stress states such as 11mm14° unbent, outside and 12mm12° unbent, outside both with residual axial stresses of 80 MPa show moderately to strongly varying signal

intensities: energies of 3.557 x$10^6$ QU and 2.9148 x$10^6$ QU respectively. This observation is logical, however, as signal intensity is dependent upon several factors, such as dislocation density, grain boundary distribution or grain sizes just to name a few [160–162]. Nevertheless, especially factors such as dislocation density are influenced during the bending process. Hence, an overlapping of various effects can quickly occur, making it difficult or even impossible to establish and identify a clear characteristic line between the signal intensity and residual stresses.
Equally, the same observation can be made for just the SF alone, SF=-0.093 and -0.131. However, a combined approach of the detected symmetries and energy levels, will give a sufficient understanding as well as information for the successful derivation of the residual axial stress state in the over- and underbent tubes based on BHN.

## 7.5 System description and modelling

Now, that the residual axial stress states in unbent and bent parts of the tubes are determined, and the BHN signal setting parameters and evaluation methods are determined, the relationship between residual axial stress state and the BHN signal are to be determined. The following section will introduce the implemented state space model and describe the correlation method as well as the fitting parameters chosen. Thereafter, the polynomial features of the regression model will be introduced, and the corresponding residual introduced as the indicator for the best model. Furthermore, the derivation of the state equation will be introduced and investigated regarding the quality of the proposed model.
In state space modelling, a non-linear system can commonly be described using the state equation and the output equation as previously mentioned in Formula 2-22 and Formula 2-23. The following two equations are, again, state equation and output equation in a special form. Nevertheless, they are listed again to demonstrate the exact modelling approach adopted in this chapter.

$$x_k = f(x_{k-1}, u_{k-1}, w_{k-1}) \qquad \text{Formula 7-8}$$

$$y_k = h(x_k, v_k) \qquad \text{Formula 7-9}$$

With $x_k$ being the observed states, $u_{k-1}$ the control and $w_{k-1}$ the process noise and function $f$ (state transition function) describing the relationship between the state at time $k$ and $k-1$, function $h$ (observation function) in Formula 7-9 describes the non-linear relationship between the measurement variable $y_k$ meaning the BHN signal intensity and the state variable $x_k$ meaning the residual axial stresses.
After retrieving the BHN measurements and XRD measurements, correlation of the two is conducted to find function $h$ and furthermore function $f$. As the correlation scheme will propose the function $h$, Formula 7-9, of the BHN signal in the model to be proposed, influencing states as well as inputs must be identified. In this study, the influencing states are the residual axial stresses and the symmetry characteristics of the

BHN signal (meaning the newly introduced SF), while the influencing inputs are the deflection of the bending die, the utilized bending angle and the measurement position meaning whether measurements were taken in unbent or bent state. The correlation coefficients between the residual axial stresses and determined parameters are computed to evaluate the significance of correlation. This work utilizes the Pearson method for the computation of correlation coefficients, as it is the most commonly used method that shows the significance of the correlation relationship between variables. The computed coefficients can be taken from Table 7-3, where the BHN is the maximum of the BHN signal and SF the symmetry factor. The correlation coefficient ranges from -1 to 1, where the value of 1 suggests a linear relationship between the variables and 0 implies no linear dependency.

*Table 7-3: Pearson correlation coefficients of individual correlation parameters.*

| | Stress | BHN | SF | Deflection | Angle | Position |
|---|---|---|---|---|---|---|
| Stress | 1 | 0.029174 | 0.56958 | -0.16611 | 0.118104 | -0.03678 |
| BHN | 0.029174 | 1 | -0.05836 | 0.553892 | -0.38313 | 0.055844 |
| SF | 0.56958 | -0.05836 | 1 | 0.0078 | -0.10226 | -0.46173 |
| Deflection | -0.16611 | 0.553892 | 0.0078 | 1 | -0.91452 | -1.6 E-16 |
| Angle | 0.118104 | -0.38313 | -0.10226 | -0.91452 | 1 | 1.55 E-16 |
| Position | -0.03678 | 0.055844 | -0.46173 | -1.6 E-16 | 1.55 E-16 | 1 |

The residual axial stresses are strongly correlated to the SF, weakly correlated to the deflection and angle. Although, residual axial stresses are very weakly correlated to the BHN and measurement position, they will be used in the correlation.

To choose an appropriate correlation strategy, the linearity between the parameters is analyzed. Figure 7-8 shows that the residual axial stresses with respect to the SF show a highly non-linear relationship.

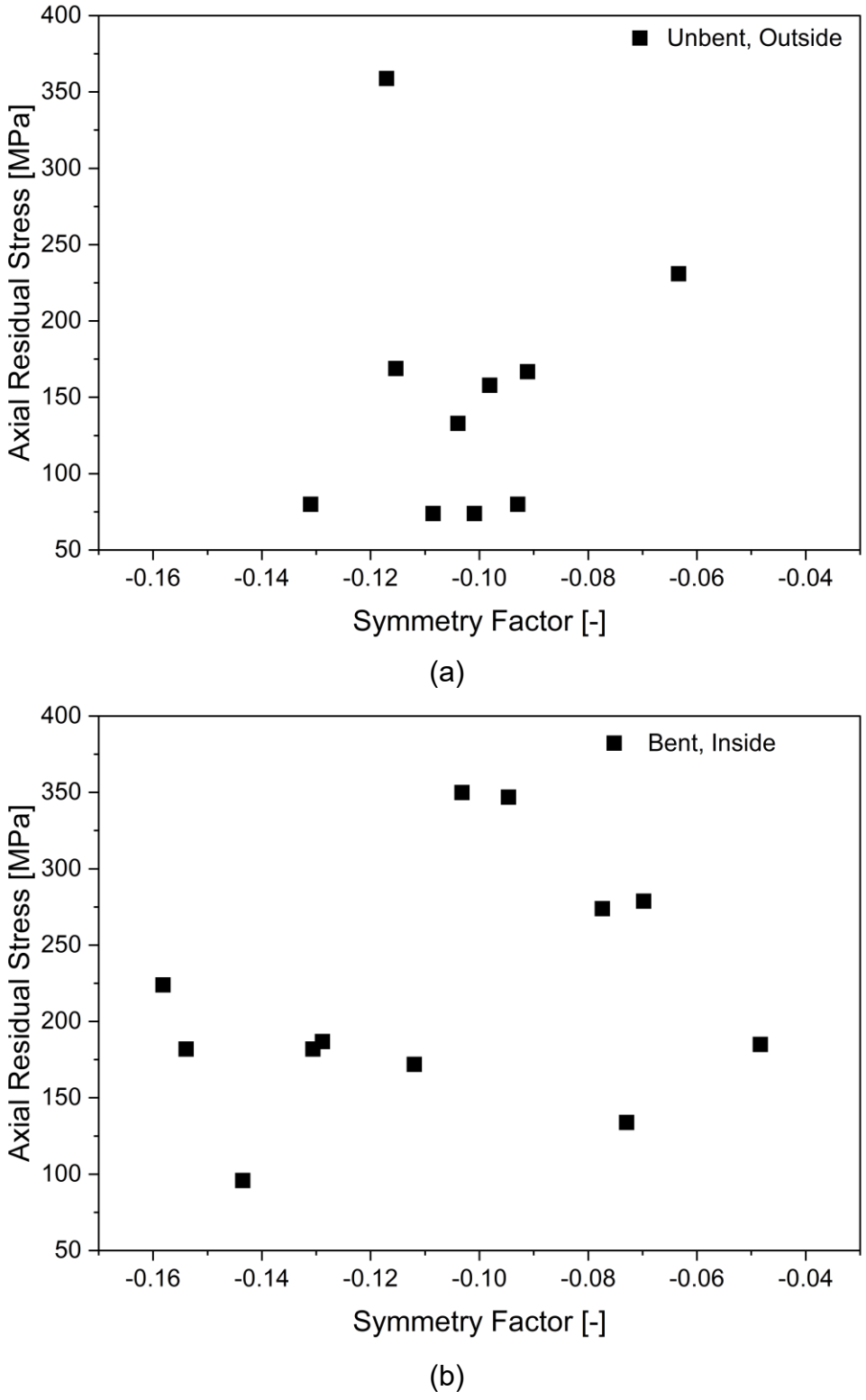


*Figure 7-8: Exemplary relationship of residual axial stresses and SF in (a) unbent and (b) bent states to show non-linearity.*

Thus, a polynomial regression is chosen for correlation. When proposing a regression, the chosen features need to be modified such that the fitting model can be optimized. In this work, the SF is used as its negative reciprocal in the regression model, as it entails the following advantages: the SF sign, meaning whether the geometry of the signal is rather right- or left-skewed, remains the same. Furthermore, initially, the range

of the SF lie between -0.05 and -0.2 while the residual axial stresses range from 50 MPa to 500 MPa, leading to even small vibrations and noise having a significant impact on the stability of the model. After taking the negative reciprocal, however, the range of SF increases to a range of 5 to 20, such that the symmetry characteristics of different BHN measurements may be distinguished more clearly and the noise in the symmetry of the BHN signal has less effect on the regression model.

After determining the suitable parameters and considering the non-linear relationships of the input data, the for python supplied method of PolynomialFeatures is used [163]. Polynomial features are features established in raising a chosen modelling parameter to an exponent. This creates new input features based on the existing features. A feature, raised to an exponential power, changes the probability distribution, which often leads to an ultimately improved regression model performance. In this work a polynomial feature of degree 3 was chosen under the consideration of the parameters: residual axial stresses ($x_1$), SF ($x_2$), deflection ($x_3$), angle ($x_4$) and position ($x_5$).

After generating the higher order of polynomial features, the problem of polynomial regression becomes one of linear regression. In general form, the optimal coefficients vector $\theta$ and the intercept $b$ must be chosen such that Formula 7-10 has a minimum error under consideration of the previously generated polynomial features $F$:

$$BHN = \theta^T F + b \qquad \text{Formula 7-10}$$

The error of the correlation is defined by the cost function seen in Formula 7-11, where $y_i$ is the real value and $\hat{y}_i$ the predicted value of the regression model.

$$Error = min \sum_i^n (y_i - \hat{y}_i)^2 \qquad \text{Formula 7-11}$$

However, this classical approach in polynomial regression oftentimes leads to overfitting of the data, especially if the data set is limited in size, meaning that the fitting model aligns too perfectly with the data. As a result, the fitting model works very well on the initial data set, however, poorly for general use.

To overcome this problem, this work uses the modified polynomial regression of Ridge regression, where the difference lies in the defined cost function, see Formula 7-12.

$$Error = min \sum_i^n (y_i - \hat{y}_i)^2 + \alpha \sum_i^n (\theta_i^2) \qquad \text{Formula 7-12}$$

The term $\alpha \sum_i^n (\theta_i^2)$ is a penalty term that can be manipulated to overcome the problem of data overfitting. The larger the chosen $\alpha$, the smaller the effect of overfitting, however, leading to a decrease in the prominent independent variables. During the correlation process, $\alpha$ cannot be optimized, which is why a one-dimensional grid search method is used to find the best performing $\alpha$ parameter from values (0,1] in step sizes of 0.01, which is then evaluated using the $R^2$ score.

After deriving the function $h$, the state equation must be derived. To derive this dependence, the analogous methodology as for deriving the output equation.

The performance of both the output equation and state equation is evaluated using the $R^2$ score. It is a statistical parameter indicating the proportion of the variance for a dependent variable explained by an independent variable or variables. If the $R^2$ is equal to 1, then all estimates given by the model are equivalent to those measured, when the $R^2$ is equal to 0, the model simply estimates all values as its mean values. Hence, the higher the $R^2$ score, the better the prediction performance of the regression model. The following algorithms, Table 7-4 and Table 7-5, show the pseudo codes for the derivation of the output and state equation.

*Table 7-4: Algorithm for output equation.*

**Algorithm 1: Derivation of correlation scheme for output equation.**

**Input :** maximum deflection (def), angle, position of measurement (pos), residual axial stress (rs), symmetry factor (sf).

**Output:** Barkhausen noise

1 Compression: compress the BHN measurement along the frequency axis (mean pooling) (usually from 512 to 64)
2 Sorting: sorts the given times and BHN signals w.r.t. time
3 Normalizing: shift the BHN signal curves to center
4 Noise Suppression: suppress measurement noise of BHN signal in summing up signals with different frequencies
5 Curve Smoothing: smooth the BHN signal curve using mean smoothing
6 Symmetry Evaluation: compute symmetry factor $sf = \frac{t_{max} - t_{center}}{l}$ of processed BHN signal, where $t_{max}$, $t_{center}$ and $l$ are the pedal point, the center point along the bottom length of the signal and the bottom length of the signal and generate the negative reciprocal $-1/sf$.
7 Polynomial Features Generation: generate the polynomial features of def, angle, pos, rs and sf of degree 3.
8 Correlation: correlate the measured BHN w.r.t. generated polynomial features by means of Ridge regression.
9 Evaluation: find the Ridge regression model with best $R^2$ score.
10 return BHN

*Table 7-5: Algorithm for state equation.*

**Algorithm 2: Derivation of correlation scheme for state equation**

**Input :** maximum deflection (def), angle, stress state, position of measurement (pos), residual axial stress (rs) before and after bending.

**Output:** predicted residual axial stresses.

1 Polynomial Features Generation: generate the polynomial features of def, angle, stress state, pos, rs of degree 2.
2 Correlation: correlate the residual axial stresses after w.r.t. generated polynomial features by means of Ridge regression dependent upon time.
3 Evaluation: find the Ridge regression model with best $R^2$ score.
4 return predicted residual axial stresses

100 ridge regression models are derived, where the hyperparameter $\alpha$ is varied from 0.01 up to 1. All the derived regression models are then assessed regarding their $R^2$ score. The model with the best $R^2$ score is then implemented into the model. $R^2$ scores for the output equation lie between -20,11 at its worst up to 0.6707, which is then chosen for correlation. The optimal coefficients vector and the intercept for the output function thus result in:

$$\theta^T =$$

$$(1\ x_1\ x_2\ x_3\ x_4\ x_5\ x_1^2\ x_1^2x_5\ x_1x_3\ x_1x_4\ x_1x_5\ x_2^2\ x_2x_3\ x_2x_4\ x_2x_5\ x_3^2\ x_3x_4\ x_3x_5\ x_4^2\ x_4x_5\ x_5^2$$
$$x_1^3\ x_1^2x_2\ x_1^2x_3\ x_1^2x_4\ x_1^2x_5\ x_1x_2^2\ x_1x_2x_3\ x_1x_2x_4\ x_1x_2x_5\ x_1x_3^2\ x_1x_3x_4\ x_1x_2x_5\ x_1x_4^2\ x_1x_4$$
$$x_1x_5^2\ x_2^3\ x_2^2x_3\ x_2^2x_4\ x_2^2x_5\ x_2x_3^2\ x_2x_3x_4\ x_2x_3x_5\ x_2x_4^2\ x_2x_4x_5\ x_2x_5^2\ x_3^3\ x_3^2x_4\ x_3^2x_5\ x_3$$
$$x_3x_4x_5\ x_4^3\ x_4^2x_5\ x_4x_5^2\ x_5^3)$$

$$= (0\ -4{,}49x10^3\ 6{,}02x10^3\ -4{,}40x10^2\ 3{,}85x10^4\ 2{,}97x10^2\ -4{,}93x10^4$$
$$-2{,}99x10^2\ -8{,}86x10^3\ -7{,}88x10^3\ 7{,}85x10^3\ 9{,}43x10^4\ 1{,}76x10^4$$
$$-1{,}31x10^4\ -2{,}92x10^2\ -4{,}40x10^3\ 9{,}17x10^4\ -9{,}01x10^3$$
$$-7{,}40x10^2\ -1{,}20x10^5\ 2{,}94x10^2\ 5{,}58x10^3\ 2{,}10x10^3$$
$$-1{,}61x10^3\ 6{,}68x10^1\ 1{,}49x10^5\ -5{,}10x10^2$$
$$-9{,}38x10^3\ 1{,}61x10^2\ 2{,}11x10^4\ 1{,}91x10^4\ -1{,}95x10^3$$
$$-1{,}15x10^5\ 3{,}77x10^1\ -5{,}04x10^3\ 1{,}02x10^3$$
$$-1{,}26x10^3\ 1{,}84x10^2\ 7{,}77x10^4\ 3{,}14x10^4$$
$$-1{,}17x10^2\ 1{,}54x10^4\ 1{,}31x10^1\ -6{,}02x10^3\ 1{,}15x10^4\ -3{,}34x10^4$$
$$-7{,}49x10^3$$
$$-9{,}72x10^4\ 2{,}34x10^1\ 1{,}08x10^4\ 2{,}51x10^3\ 1{,}49x10^{-1}\ 6{,}10x10^2)$$

and $b = -6884429.95$

Figure 7-9 shows the output equations derivation of the BHN signal intensity using the parameters described. The $R^2$ value lies at 0.6707, meaning the regression model is a suitable fit, however, can be improved.

It can be observed that the model derives best results for the inside of the tubes, whereas the results for the bent, outside tubes show the largest deviations. The highest deviation between the derived and measured BHN signal intensity is seen in the bent, outside 10mm20° (b) tube. Here, the model overestimates the measurement by $7.28x10^5$ QU. The larger deviation between the measurements and the derived values from the regression model in the outside, bent tubes may be due to the fact, that the regression model in the evaluation of the signal intensity, does not regard the influences of other pinning site effects, such as grain boundary distribution, grain sizes and/or inclusions. These will all influence the signal intensity, and a superimposition of effects cannot be fully ruled out. Hence, a separated investigation of the influencing pinning sites may improve performance of the prediction model, however, at cost of model simplicity and calculation time of the model.

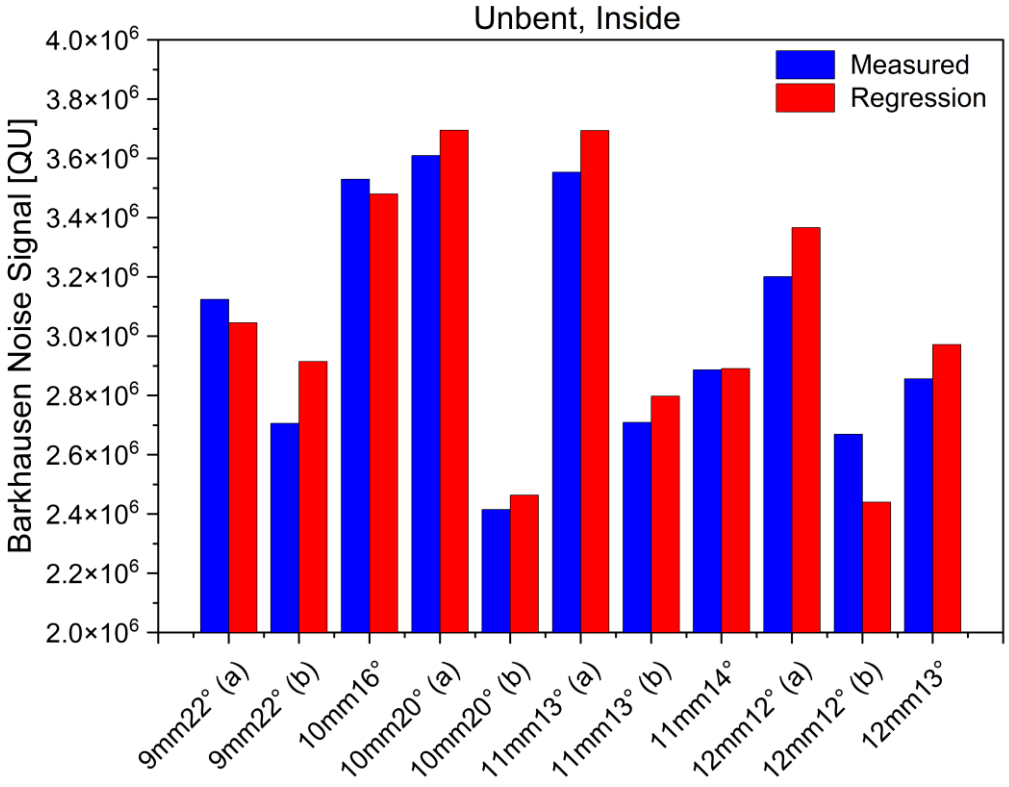
Unbent, Inside
Measured
Regression
Barkhausen Noise Signal [QU]
4.0×10^6
3.8×10^6
3.6×10^6
3.4×10^6
3.2×10^6
3.0×10^6
2.8×10^6
2.6×10^6
2.4×10^6
2.2×10^6
2.0×10^6
9mm22° (a)
9mm22° (b)
10mm16°
10mm20° (a)
10mm20° (b)
11mm13° (a)
11mm13° (b)
11mm14°
12mm12° (a)
12mm12° (b)
12mm13°

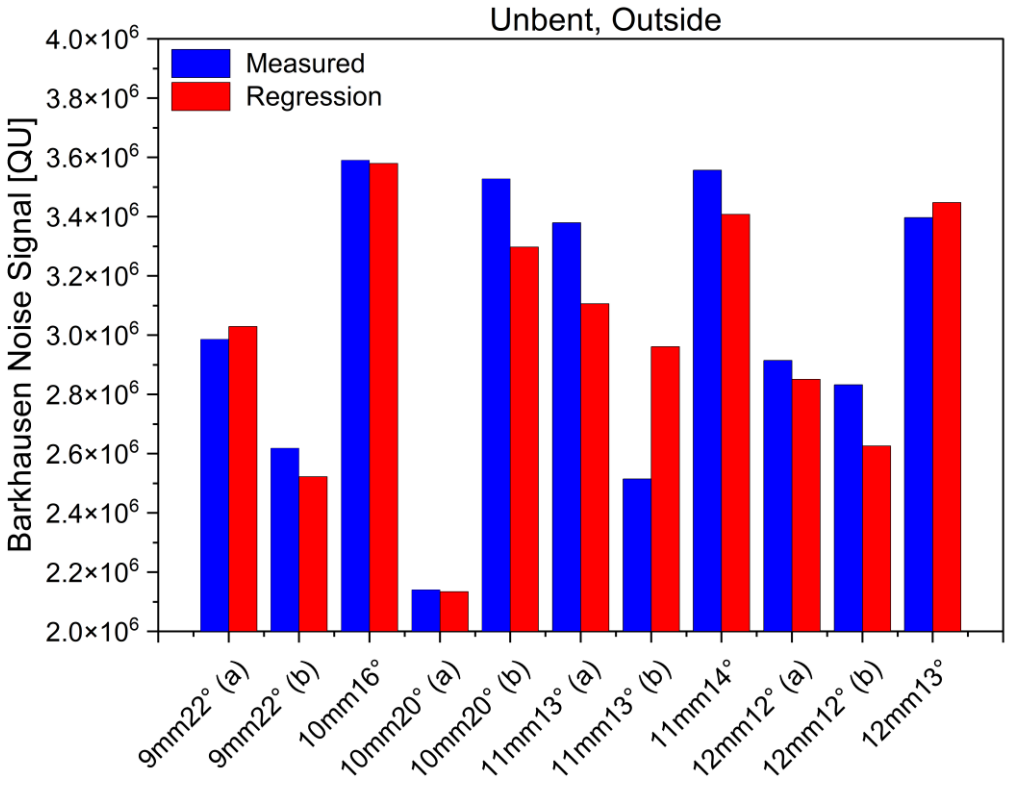
Unbent, Outside
Measured
Regression
Barkhausen Noise Signal [QU]
4.0×10^6
3.8×10^6
3.6×10^6
3.4×10^6
3.2×10^6
3.0×10^6
2.8×10^6
2.6×10^6
2.4×10^6
2.2×10^6
2.0×10^6
9mm22° (a)
9mm22° (b)
10mm16°
10mm20° (a)
10mm20° (b)
11mm13° (a)
11mm13° (b)
11mm14°
12mm12° (a)
12mm12° (b)
12mm13°

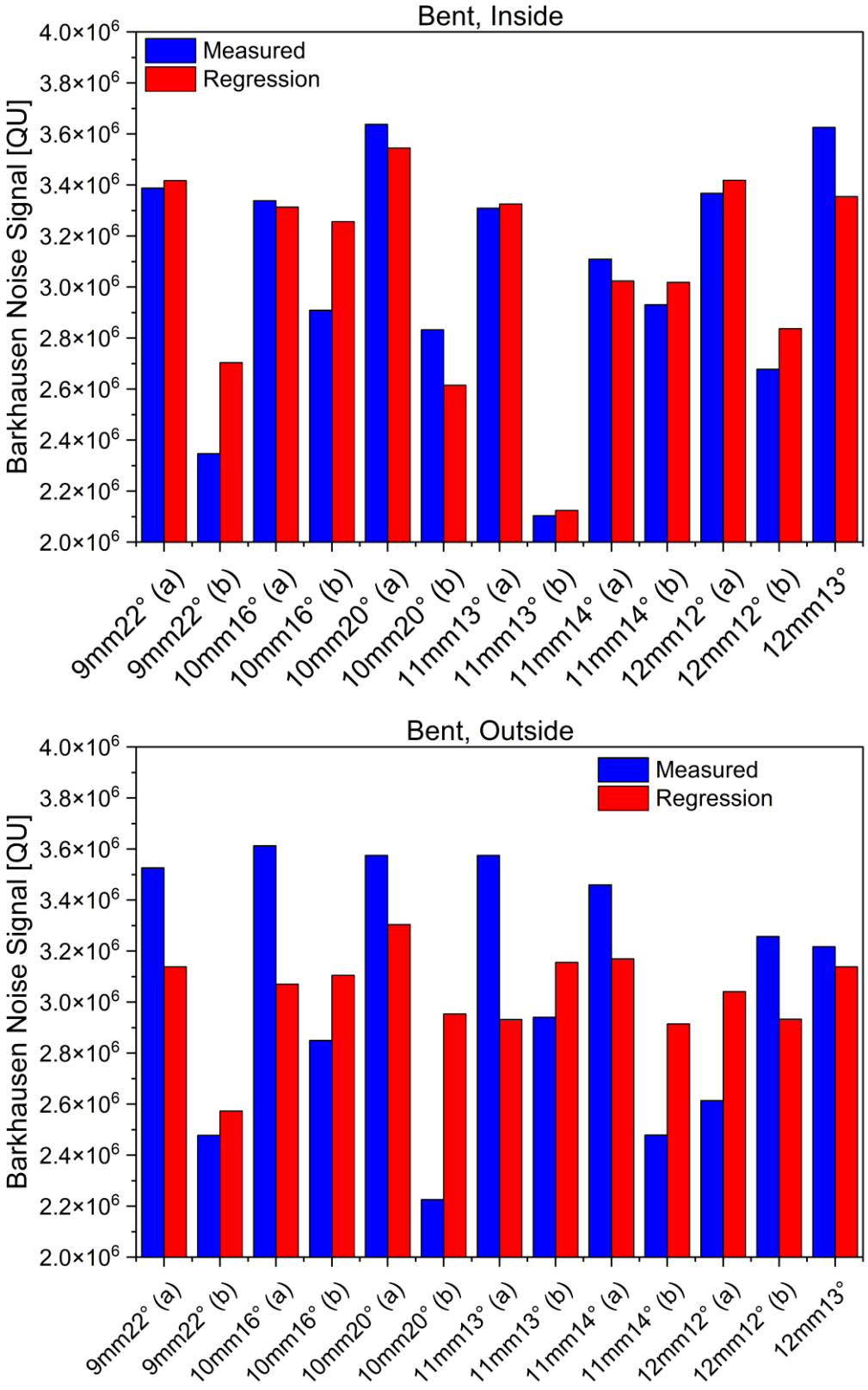


*Figure 7-9: Derived BHN signal by means of regression based on symmetry characteristics and signal intensity.*

The model performance, overall, can be enhanced with a higher number of measurements, especially XRD-measurements. However, due to the high cost of the measurements only 48 measurements in total could be conducted, resulting in a sufficiently

accurate regression model to be proposed. Further measurements, nevertheless, are recommended.

For the state equation, the optimal coefficients vector is:

$$\theta^T = (1\ x_1\ x_2\ x_3\ x_4\ x_5\ x_1^2\ x_1^2x_5\ x_1x_3\ x_1x_4\ x_1x_5\ x_2^2\ x_2x_3\ x_2x_4\ x_2x_5\ x_3^2\ x_3x_4\ x_3x_5\ x_4^2\ x_4x_5\ x_5^2)$$

$$= (0\ \ 1{,}914x10^0\ \ -9{,}06x10^0\ \ 1{,}092x10^0\ \ 9{,}784x10^{-1}\ -3{,}44x10^1\ -3{,}59x10^0\ -2{,}08x10^1\ 2{,}81x10^0\ -8{,}66x10^0\ 1{,}53x10^0\ 4{,}54x10^0\ 2{,}21x10^0\ 2{,}59x10^0\ 2{,}48x10^{-1}\ \ 0\ \ 2{,}50x10^1\ -3{,}16x10^{-1}\ 5{,}87x10^0\ \ 3{,}59x10^{-1}\ \ 2{,}31x10^{-2})$$

and $b = 4710{,}70$

The results derived by the state equation can be observed in Figure 7-10. The results for randomly chosen measurements on the over- and underbent tubes in bent and unbent state, where also XRD residual stress measurements were taken on. The $R^2$ of the proposed state function lies at 0.9181, meaning the proposed model provides a very good fit, as can be seen in the results delivered. Furthermore, two data points were extracted from the data set to give a validation of the proposed model. The predicted residual axial stresses are overall in very good agreeance with the physically taken measurements (maximum deviation of 33 MPa), hence a validated model is introduced.

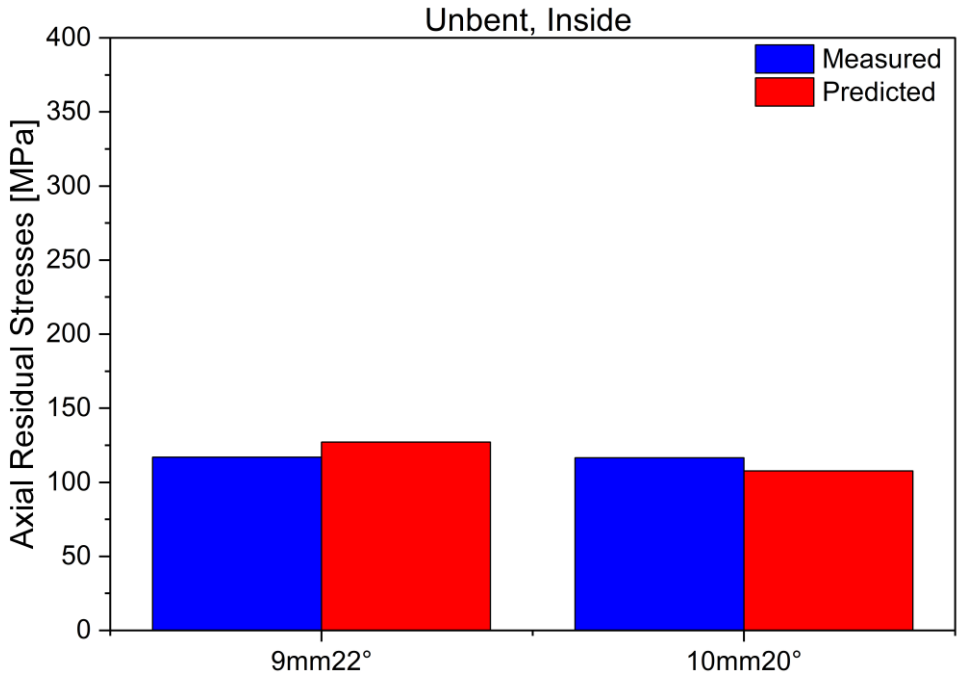
Unbent, Inside
Measured
Predicted
Axial Residual Stresses [MPa]
400
350
300
250
200
150
100
50
0
9mm22°
10mm20°

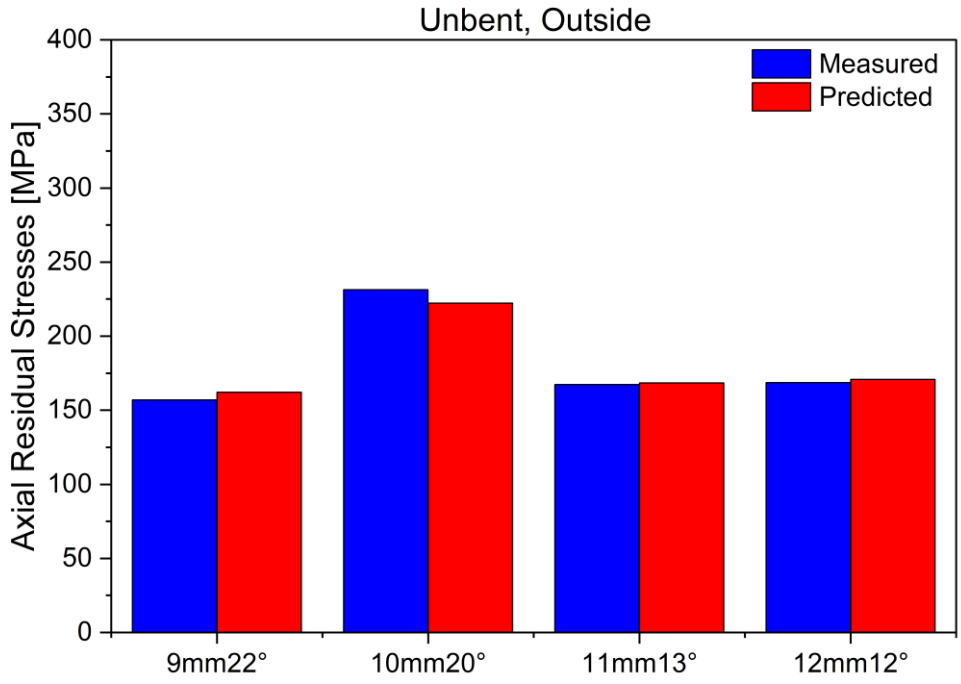
Unbent, Outside
Measured
Predicted
Axial Residual Stresses [MPa]
400
350
300
250
200
150
100
50
0
9mm22°
10mm20°
11mm13°
12mm12°

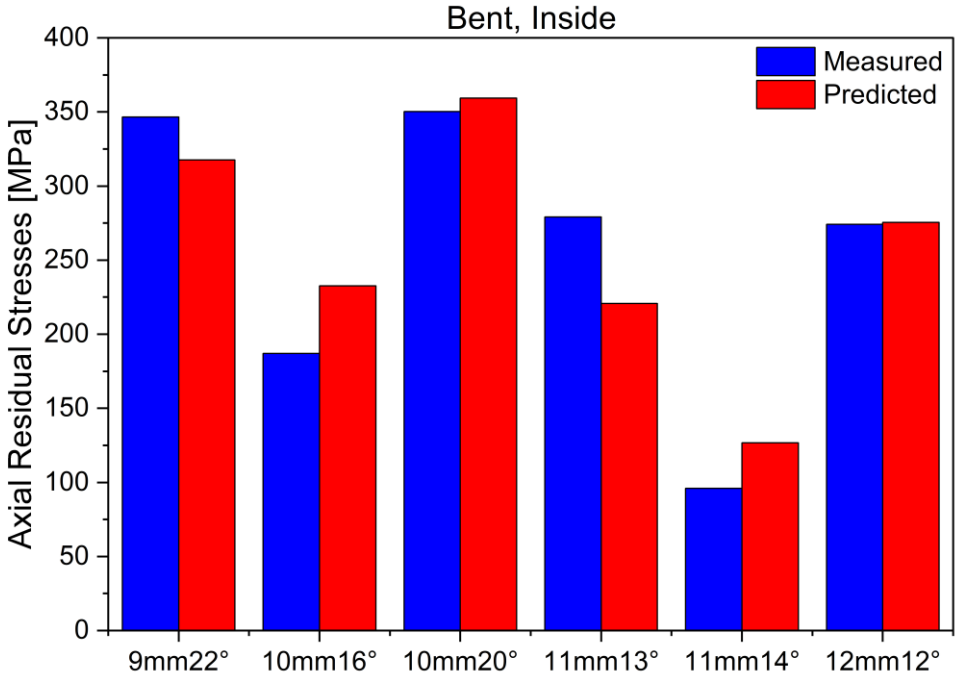
Bent, Inside
Axial Residual Stresses [MPa]
0
50
100
150
200
250
300
350
400
Measured
Predicted
9mm22°
10mm16°
10mm20°
11mm13°
11mm14°
12mm12°

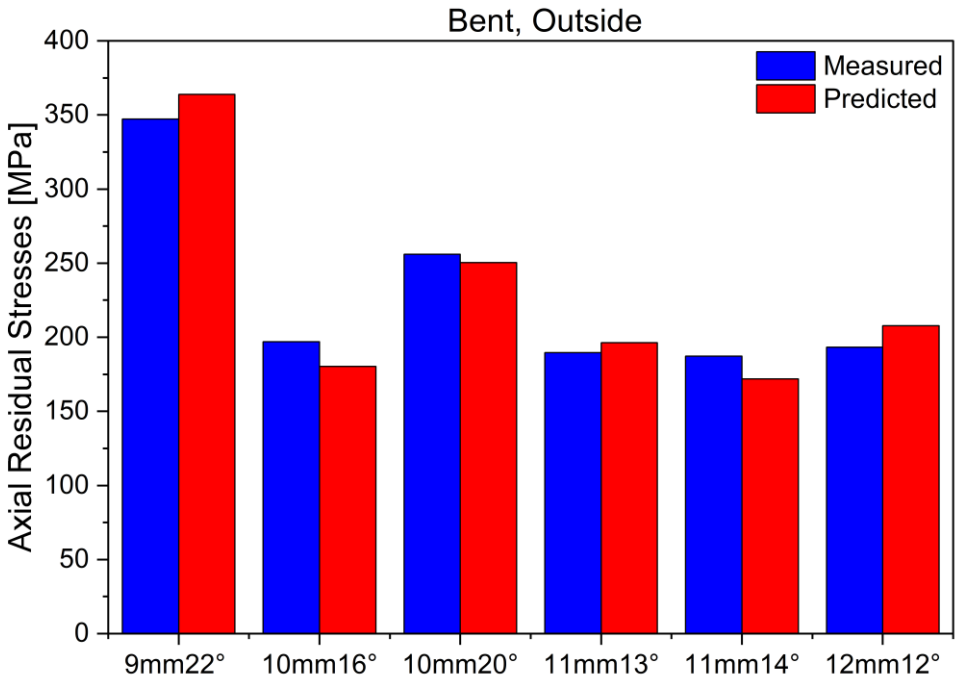
Bent, Outside
Axial Residual Stresses [MPa]
0
50
100
150
200
250
300
350
400
Measured
Predicted
9mm22°
10mm16°
10mm20°
11mm13°
11mm14°
12mm12°

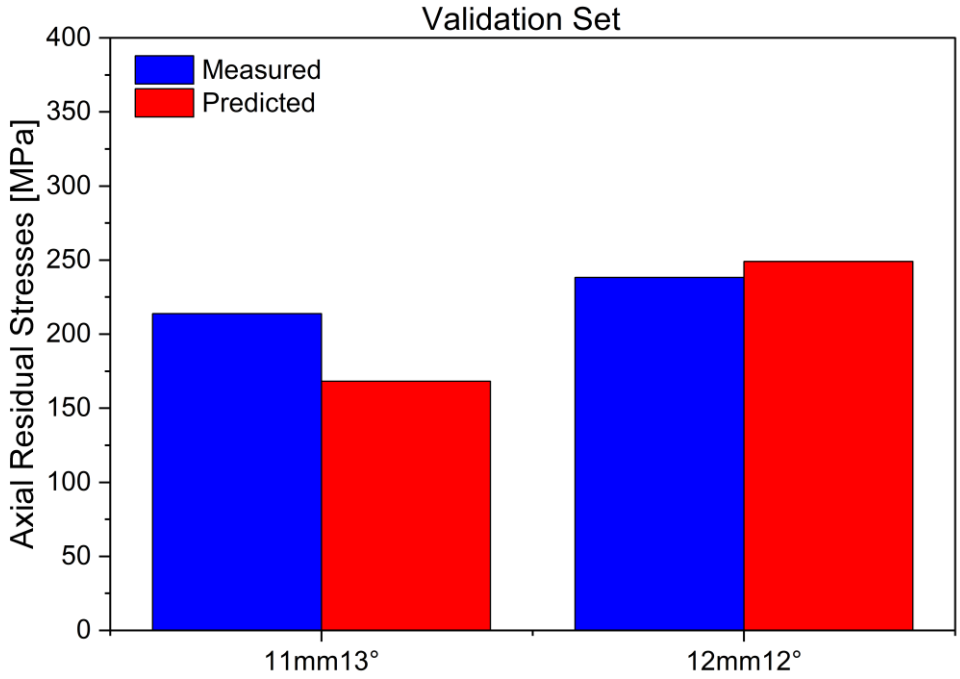


*Figure 7-10: Derived residual axial stress level by means of regression based on symmetry characteristics and signal intensity as well as validation predictions using proposed model.*

Generally, it must be mentioned, that the proposed model is still based on a limited data set. Additional measurements will be beneficial to further improve model performance. However, the proposed model is valid for use on the newly introduced bending strategy of non-tangential, i.e. over- and underbending, of the tubes and will have a strong impact on the sustainability as well as economic efficiency of the process, as the residual axial stress level in the tubes can now be quantitatively derived during the bending process. Based on the prediction of the residual axial stress levels, a closed-loop control can be implemented within the freeform bending process. In now knowing the quantitative residual axial stress level within the tubes, distortion and complications in the post-production steps can be minimized, hence leading to less scrap metal.

## 7.6 Conclusion and Evaluation of Results

Overall, this chapter introduces a static, non-linear model for prediction of residual axial stresses for over- and underbent tubes based on BHN analysis, that extends the soft sensor introduced in Chapter 6 using the DOF presented in Chapter 5. To do so, the residual axial stresses were measured using XRD-measurements, which is a method that allows the quantification of residual stresses type I based on crystal lattice spacing. The conducted measurements not only provided the basis for correlation with BHN but also validate the successful decoupling of geometry and residual stresses due to the superposition of stresses (see Chapter 5.1.3). It is observed, that the over- and underbending introduces significantly different levels of residual axial stresses, that are then used to correlate with BHN.

Furthermore, BHN analysis was conducted. To begin with a sensitivity analysis of the utilized measurement equipment, QASS µmagnetic measuring system, is performed as magnetic characteristics are strongly dependent upon the tested material. Since there are a manifold of parameters that can be set, that all influence the magnetic field or evaluation thereof, the sensitivity analysis aims to find the most adequate settings to guarantee stable, reproducible measurements on P235 TR1, as well as a processable signal for correlation. Considering the penetration depth of the magnetic field, ideal measurement settings for the investigated P235 TR1 are identified, that can be commonly used for BHN analysis from now on. Even though, the penetration depth of the XRD- and BHN-measurements are not in perfect congruence, a correlation is still auspicious as XRD provides residual stresses of type I, meaning they are present in a larger area in the material.

BHN analysis is strongly influenced by several microstructural occurrences such as grain boundaries or dislocation density just to name a few. Due to this superposition of effects that automatically occurs after bending because of the strain hardening effects, the mere observation of the signal intensity cannot be recommended, as it provides too little information. However, it was observed that when the residual axial stress state is influenced, the change in stress state can be observed in the symmetry of the measurement signal. The reason lies in the fact that if a material is under stress, the magnetic field is given a preferred orientation, resulting in the tilting of the hysteresis curve. This means, that if the residual axial stresses in the tubes redistribute, the BHN measurement signal in the QASS µmagnetic measuring system, shows a skewedness. Thus, this skewedness was mathematically examined, and a so-called SF is introduced, which now in combination with the signal intensity enables a precise correlation between BHN and residual axial stresses. As measurements were taken in unbent as well as bent state, the implementation of a static, non-linear model is made possible, based on ridge regression which minimizes the effect of overfitting due to a limited data set. Hence, the model qualities are adequate for both state and output equation, whereas the state equation model could also be validated.

However, some deviation in the models is still observed, which is primarily due to the limited data set. Hence, it is recommended to conduct further measurements, especially, XRD-measurements. Furthermore, additional microstructural investigations especially regarding grain size and dislocation density may provide additional information and increase quality of the model. This in turn with be at the expense of computational efforts of the model, as it will become more complex.

All in all, the now established possibility to derive the residual axial stresses within P235TR1 steel tubes for over- and underbending, further enhances the bending process as a manipulation of the actuators to meet a defined residual axial stress level is now possible. This in turn, will lessen scrap metal as well as distortion in post-processing steps after bending.

# 8 Conclusions

The overall aim of this work was the implementation of a soft sensor for freeform bending with movable die that allows the quick derivation of selected mechanical properties in round steel tubes, that are impossible or very difficult to determine during the process. This soft sensor then enables the formulation of a closed-loop property control within the process, which in turn enhances the resource, time as well as economic efficiency. To do so, this scientific work initially explores DOF in the machine, that allows an influencing of the mechanical properties decoupled from the geometrical evolution. This knowledge is in turn used to derive a soft sensor that predicts strength, ductility, hoop and residual axial stresses based on UCI hardness and BHN measurements for P235 TR1 steel tubes.
The key findings of this work are:

- The exploitation of superposition of stresses as DOF that allows a separate influencing of geometrical evolution and mechanical properties. Furthermore, the validation thereof by means of hardness and residual stress measurements.
- The numerical modelling of the mechanical properties of the entire tube, i.e. weld seam and base material by means of tensile tests. The validation of the modelled material characteristics and implementation into the simulation model of the bending process.
- The determination that hardness is significantly influenced by strain hardening, thus the local strength of the material as well as residual hoop stresses.
- The identification of the relationships among hardness, strength, ductility, and residual hoop stresses. The mathematical modelling of these and implementation into a soft sensor based on EKF.
- The recognition that the geometry of the BHN measurement signal is distorted by residual stresses, thus revealing the detrimental parameter (called SF) for quantitative determination of residual stresses from BHN.
- The mathematical formulation of the relationship between BHN and residual axial stresses determined by XRD-measurements and implementation into the soft sensor using a state-space model.

# 9 Outlook

This scientific work introduces a soft sensor that allows the derivation of relevant mechanical properties during freeform bending with movable die. However, for industrial application of these findings, further research is recommended. The future research aspects resulting from this work are listed below:

- For further safety assessment regarding the scattering of initial mechanical properties or semi-finished product dimensions, a case study on a component made of over- and underbent tubes subjected to a certain load could be conducted. However, an implementation into the soft sensor should be made dependent on how strongly the computational efficiency is influenced.
- For a real-time application of the soft sensor, the sensors must be reduced to only BHN sensors as the UCI hardness sensor can only be used whenever the process comes to a full halt. Works by the developers QASS already show, that a correlation of BHN and hardness is feasible, entailing that the introduced methodology can further be used.
- As the introduced methodology is costly and time-consuming to derive all correlations between the parameters, a simplification of the concept could be explored. This could be done in a numerical modelling of the residual stresses or investigations whether, i.e. n-values provide critical information on the material properties which in turn lead to characteristic fields.
- The implementation of further data points is advised, especially in the BHN and residual stress model, as due to cost of the XRD-measurements only 48 data points could be taken.
- Lastly, a transfer to further material classes could be performed. It should be noted that the material needs to be ferromagnetic, otherwise the BHN sensor becomes obsolete.

# 10 References


[1] W. Hao, S. Duncan, Optimization of tool trajectory for Incremental Sheet Forming using closed loop control. In: *2011 IEEE International Conference on Automation Science and Engineering*, 779–784. IEEE; 2011.

[2] J. A. Polyblank, J. M. Allwood, S. R. Duncan, Closed-loop control of product properties in metal forming: A review and prospectus, *Journal of Materials Processing Technology* 214, 2333–2348 (2014); doi: 10.1016/j.jmatprotec.2014.04.014.

[3] J. M. Allwood, S. R. Duncan, J. Cao, P. Groche, G. Hirt, B. Kinsey, T. Kuboki, M. Liewald, A. Sterzing, A. E. Tekkaya, Closed-loop control of product properties in metal forming, *CIRP Annals* 65, 573–596 (2016); doi: 10.1016/j.cirp.2016.06.002.

[4] J. M. Allwood, O. Music, A. Raithathna, S. R. Duncan, Closed-loop feedback control of product properties in flexible metal forming processes with mobile tools, *CIRP Annals* 58, 287–290 (2009); doi: 10.1016/j.cirp.2009.03.065.

[5] G. Luxbacher, *Durchleuchten und Durchschallen: Geschichte der Deutschen Gesellschaft für Zerstörungsfreie Prüfung von 1933 bis 2018*. Hanser, München; 2018.

[6] J. R. Deepak, V. K. Bupesh Raja, D. Srikanth, H. Surendran, M. M. Nickolas, Non-destructive testing (NDT) techniques for low carbon steel welded joints: A review and experimental study, *Materials Today: Proceedings* 44, 3732–3737 (2021); doi: 10.1016/j.matpr.2020.11.578.

[7] J. Jaskowska-Lemańska, E. Przesmycka, Semi-Destructive and Non-Destructive Tests of Timber Structure of Various Moisture Contents, *Materials (Basel, Switzerland)* 14 (2020); doi: 10.3390/ma14010096.

[8] J. Jaskowska-Lemańska, J. Sagan, Non-Destructive Testing Methods as a Main Tool Supporting Effective Waste Management in Construction Processes, *Archives of Civil Engineering* 65, 263–276 (2019); doi: 10.2478/ace-2019-0059.

[9] L. Fortuna, S. Graziani, A. Rizzo, M. G. Xibilia, *Soft Sensors for Monitoring and Control of Industrial Processes*. Springer London, London; 2007.

[10] Y. Jiang, S. Yin, J. Dong, O. Kaynak, A Review on Soft Sensors for Monitoring, Control, and Optimization of Industrial Processes, *IEEE Sensors Journal* 21, 12868–12881 (2021); doi: 10.1109/JSEN.2020.3033153.

[11] P. Kadlec, B. Gabrys, S. Strandt, Data-driven Soft Sensors in the process industry, *Computers & Chemical Engineering* 33, 795–814 (2009); doi: 10.1016/j.compchemeng.2008.12.012.

[12] T. Becker, D. Krause, Softsensorsysteme – Mathematik als Bindeglied zum Prozessgeschehen, *Chemie Ingenieur Technik* 82, 429–440 (2010); doi: 10.1002/cite.201000015.

[13] P. Arpaia, R. Cuocolo, F. Donnarumma, A. Esposito, N. Moccaldi, A. Natalizio, R. Prevete, Conceptual design of a machine learning-based wearable soft sensor for non-invasive cardiovascular risk assessment, *Measurement* 169, 108551 (2021); doi: 10.1016/j.measurement.2020.108551.

[14] A. S. Dahiya, Y. Kumaresan, O. Ozioko, M. Ntagios, R. Dahiya, Soft Sensors for Electronic Skin. In: *Encyclopedia of Sensors and Biosensors*, 51–67. Elsevier; 2023.

[15] M. Gyürkés, L. Madarász, P. Záhonyi, Á. Köte, B. Nagy, H. Pataki, Z. K. Nagy, A. Domokos, A. Farkas, Soft sensor for content prediction in an integrated continuous pharmaceutical formulation line based on the residence time distribution of unit operations, *International journal of pharmaceutics* 624, 121950 (2022); doi: 10.1016/j.ijpharm.2022.121950.

[16] T. Hwang, H. J. Lee, S. Hwang, H. Yang, H. Kim, S. Jang, H. E. Jeong, Z. Y. Ryoo, J. Yeo, Self-adhesive polyurethane via selective photo-polymerization for biocompatible epidermal soft sensor and thermal heater, *Applied Materials Today* 27, 101479 (2022); doi: 10.1016/j.apmt.2022.101479.

[17] K. Qiu, J. Wang, X. Zhou, R. Wang, Y. Guo, Soft sensor based on localized semi-supervised relevance vector machine for penicillin fermentation process with asymmetric data, *Measurement* 202, 111823 (2022); doi: 10.1016/j.measurement.2022.111823.

[18] G. L. Goh, W. Y. Yeong, J. Altherr, J. Tan, D. Campolo, 3D printing of soft sensors for soft gripper applications, *Materials Today: Proceedings* 70, 224–229 (2022); doi: 10.1016/j.matpr.2022.09.025.

[19] S. Jaffer, K. Young, Noise-Adaptive Soft Sensors in Mobile Robots through Particle Filtering, *IFAC Proceedings Volumes* 42, 310–314 (2009); doi: 10.3182/20090921-3-TR-3005.00055.

[20] Q. Zou, Y. Wang, F. Yang, An intrinsically embedded pressure-temperature dual-mode soft sensor towards soft robotics, *Sensors and Actuators A: Physical* 332, 113084 (2021); doi: 10.1016/j.sna.2021.113084.

[21] G. A. de Morais, B. H. Barbosa, D. D. Ferreira, L. S. Paiva, Soft sensors design in a petrochemical process using an Evolutionary Algorithm, *Measurement* 148, 106920 (2019); doi: 10.1016/j.measurement.2019.106920.

[22] R. Sekhar, P. Shah, S. Panchal, M. Fowler, R. Fraser, Distance to empty soft sensor for ford escape electric vehicle, *Results in Control and Optimization* 9, 100168 (2022); doi: 10.1016/j.rico.2022.100168.

[23] B. Xu, C. K. Pooi, K. M. Tan, S. Huang, X. Shi, H. Y. Ng, A novel long short-term memory artificial neural network (LSTM)-based soft-sensor to monitor and forecast wastewater treatment performance, *Journal of Water Process Engineering* 54, 104041 (2023); doi: 10.1016/j.jwpe.2023.104041.

[24] E. Doege, B.-A. Behrens, *Handbuch Umformtechnik: Grundlagen, Technologien, Maschinen*. Springer, Berlin, Heidelberg; 2010.

[25] H. Hoffmann, R. Neugebauer, G. Spur, eds., *Handbuch Umformen*. Hanser, München; 2012.

[26] W. Bleck, E. Moeller, eds., *Handbuch Stahl: Auswahl, Verarbeitung, Anwendung*. Hanser, München; 2018.

[27] H. Czichos, ed., *Hütte: Die Grundlagen der Ingenieurwissenschaften*. Springer, Berlin; 1995.

[28] W. Bleck, ed., *Werkstoffprüfung in Studium und Praxis.* Mainz, Aachen; 1999.

[29] E. Hornbogen, H. Warlimont, *Metallkunde*. Springer Berlin Heidelberg, Berlin, Heidelberg; 1991.

[30] H. Altenbach, *Kontinuumsmechanik*. Springer Berlin Heidelberg, Berlin, Heidelberg; 2018.

[31] J. Rösler, H. Harders, M. Bäker, *Mechanisches Verhalten der Werkstoffe: Mit 34 Aufgaben mit Lösungen*. Vieweg + Teubner, Wiesbaden; 2008.

[32] D. Novokshanov, B. Döbereiner, M. Sharaf, S. Münstermann, J. Lian, A new model for upper shelf impact toughness assessment with a computationally efficient parameter identification algorithm, *Engineering Fracture Mechanics* 148, 281–303 (2015); doi: 10.1016/j.engfracmech.2015.07.069.

[33] F. Shen, S. Münstermann, J. Lian, An evolving plasticity model considering anisotropy, thermal softening and dynamic strain aging, *International Journal of Plasticity* 132, 102747 (2020); doi: 10.1016/j.ijplas.2020.102747.

[34] J. Lian, F. Shen, X. Jia, D.-C. Ahn, D.-C. Chae, S. Münstermann, W. Bleck, An evolving non-associated Hill48 plasticity model accounting for anisotropic hardening and r-value evolution and its application to forming limit prediction, *International Journal of Solids and Structures* 151, 20–44 (2018); doi: 10.1016/j.ijsolstr.2017.04.007.

[35] R. Hill, A theory of the yielding and plastic flow of anisotropic metals, *Proceedings of the Royal Society of London. Series A. Mathematical and Physical Sciences* 193, 281–297 (1948); doi: 10.1098/rspa.1948.0045.

[36] Y. Bai, T. Wierzbicki, A new model of metal plasticity and fracture with pressure and Lode dependence, *International Journal of Plasticity* 24, 1071–1096 (2008); doi: 10.1016/j.ijplas.2007.09.004.

[37] J. Lian, M. Sharaf, F. Archie, S. Münstermann, A hybrid approach for modelling of plasticity and failure behaviour of advanced high-strength steel sheets, *International Journal of Damage Mechanics* 22, 188–218 (2013); doi: 10.1177/1056789512439319.

[38] J. Zhu, Y. Xia, Q. Zhou, T. Wierzbicki, A Rate-Dependent Model for Metals Based on a Master Curve of Normalized Hardening Behavior of DP Steels, *Journal of Dynamic Behavior of Materials* 2, 272–282 (2016); doi: 10.1007/s40870-016-0064-4.

[39] K. H. Kloos, Eigenspannungen, Definition und Entstehungsursachen, *Materialwissenschaft und Werkstofftechnik* 10, 293–302 (1979); doi: 10.1002/mawe.19790100906.

[40] E. Macherauch, H. Wohlfahrt, U. Wolfstieg, Zur zweckmäßigen Definition von Eigenspannungen, *HTM Journal of Heat Treatment and Materials* 28, 201–211 (1973); doi: 10.1515/htm-1973-280305.

[41] M. Habschied, B. de Graaff, A. Klumpp, V. Schulze, Fertigung und Eigenspannungen*, *HTM Journal of Heat Treatment and Materials* 70, 111–121 (2015); doi: 10.3139/105.110261.

[42] H.-D. Tietz, H. Blumenauer, H. Hoffmann, *Eigenspannungen in Werkstoffen*. De Gruyter; 1977.

[43] U. Dilthey, *Verhalten der Werkstoffe beim Schweißen*. Springer, Berlin; 2005.

[44] B. D. Cullity, C. D. Graham, *Introduction to Magnetic Materials*. Wiley; 2008.

[45] P. W. Atkins, J. de Paula, J. J. Keeler, *Physikalische Chemie*. WILEY-VCH, Weinheim; 2022.

[46] G. Gottstein, *Materialwissenschaft und Werkstofftechnik*. Springer Berlin Heidelberg, Berlin, Heidelberg; 2014.

[47] M. Lambeck, *Barkhausen-Effekt und Nachwirkung in Ferromagnetika sowie analoge Erscheinungen in der Festkörperphysik*. De Gruyter; 1971.

[48] Deutsches Institut für Normung e.V., Fertigungsverfahren: Begriffe, Einteilung.

[49] Deutsches Institut für Normung e.V., Fertigungsverfahren Biegeumformen: Einordnung, Unterteilung, Begriffe.

[50] Verein Deutscher Ingenieure, VDI 3430:2014-06: Rotationszugbiegen von Profilen 25.020 (Juni 2014).

[51] L. Borchmann, *Regelung des Werkstoffflusses zur Erhöhung der Bauteilqualität beim Rotationszugbiegen*. Universitätsbibliothek Siegen; 2021.

[52] M. Hinkel, *Prozessfenster für das Spannen von Rohrprofilen beim Rotationszugbiegen unter Berücksichtigung der Tribologie*. Shaker, Aachen; 2013.

[53] C. Heftrich, B. Engel, *Erhöhung der Flexibilisierung des Rotationszugbiegens mit reduzierten Werkzeugen*. Universitätsbibliothek Siegen; 2023.

[54] L. Borchmann, C. Heftrich, B. Engel, Influence of the stiffness of machine axes on the formation of wrinkles during rotary draw bending, *SN Applied Sciences* 2 (2020); doi: 10.1007/s42452-020-03419-1.

[55] D. Landgrebe, B. Domes, T. Otto-Adamczak, M. Werner, K. Silbermann, *Querkraftfreies Freiformbiegen von Rohren*. Europ. Forschungsges. für Blechverarbeitung e.V. (EFB), Hannover; 2015.

[56] N. V. Beulich, *Entwicklung einer Methodik zur Auslegung und Absicherung des Freiformbiegens mit bewegter Matrize für dreidimensionale Biegegeometrien*; 2022.

[57] S. Groth, *Methode zur Produktplanung beim Freiformbiegen*; 2020.

[58] S. Chatti, *Optimierung der Fertigungsgenauigkeit beim Profilbiegen*. Shaker, Aachen; 1998.

[59] D. Staupendahl, S. Chatti, A. E. Tekkaya, Closed-loop control concept for kinematic 3D-profile bending. In:, 150002. Author(s); 2016.

[60] P. Gantner, H. Bauer, D. K. Harrison, A. K. de Silva, Free-Bending—A new bending technique in the hydroforming process chain, *Journal of Materials Processing Technology* 167, 302–308 (2005); doi: 10.1016/j.jmatprotec.2005.05.052.

[61] A. Ghiotti, E. Simonetto, S. Bruschi, P. F. Bariani, Springback measurement in three roll push bending process of hollow structural sections, *CIRP Annals* 66, 289–292 (2017); doi: 10.1016/j.cirp.2017.04.119.

[62] R. Neugebauer, ed., *Parallelkinematische Maschinen: Entwurf, Konstruktion, Anwendung*. Springer, Berlin, Heidelberg; 2006.

[63] R. Neugebauer, W.-G. Drossel, P. Blau, 3D-Freiformbiegen von Profilen, *Zeitschrift für wirtschaftlichen Fabrikbetrieb* 96, 611–615 (2001); doi: 10.3139/104.100494.

[64] D. Maier, *Eigenschaftsflexibles Freiformbiegen mit beweglicher Matritze*. Kollemosch Verlag und Kommunikation, Buch; 2024.

[65] Q. Yang, C. Liu, C. Cheng, X. Guo, J. Tao, Z. Ma, Effect mechanism of torsion on flat oval profile free bending, *International Journal of Mechanical Sciences* 250, 108308 (2023); doi: 10.1016/j.ijmecsci.2023.108308.

[66] P. Gantner, D. K. Harrison, A. K. M. de Silva, H. Bauer, New Bending Technologies for the Automobile Manufacturing Industry. In: S. Hinduja (ed.). *Proceedings of the 34th International MATADOR Conference*, 211–216. London: Springer London; 2004.

[67] N. Beulich, P. Craighero, W. Volk, FEA Simulation of Free-Bending – a Preforming Step in the Hydroforming Process Chain, *Journal of Physics: Conference Series* 896, 12063 (2017); doi: 10.1088/1742-6596/896/1/012063.

[68] N. Beulich, R. Mertens, J. Spoerer, W. Volk, Influence of tube rollforming on material properties and subsequent bending processes. In: *Forming Technology Forum*; 2019.

[69] N. Beulich, J. Spoerer, W. Volk, Sensitivity analysis of process and tube parameters in free-bending processes, *IOP Conference Series: Materials Science and Engineering* 651, 12031 (2019); doi: 10.1088/1757-899X/651/1/012031.

[70] X. Guo, H. Xiong, Numerical simulation and experimental study on mechanism and characteristics of tube free-bending forming process, *Procedia Manufacturing* 15, 836–843 (2018); doi: 10.1016/j.promfg.2018.07.179.

[71] X. Guo, H. Xiong, H. Li, Y. Xu, Z. Ma, A. A. El-Aty, Y. Ma, K. Jin, Forming characteristics of tube free-bending with small bending radii based on a new spherical connection, *International Journal of Machine Tools and Manufacture* 133, 72–84 (2018); doi: 10.1016/j.ijmachtools.2018.05.005.

[72] X. Guo, X. CHENG, Y. Xu, J. Tao, A. Abd El-Aty, H. LIU, Finite element modelling and experimental investigation of the impact of filling different materials in copper tubes during 3D free bending process, *Chinese Journal of Aeronautics* 33, 721–729 (2020); doi: 10.1016/j.cja.2019.02.016.

[73] M. K. Werner, D. Maier, L. Scandola, W. Volk, Motion profile calculation for freeform bending with moveable die based on tool parameters, *ESAFORM 2021* (2021); doi: 10.25518/esaform21.1879.

[74] C. J. Hellier, *Handbook of nondestructive evaluation*. McGraw-Hill, New York, NY; 2001.

[75] L. Cartz, *Nondestructive testing: Radiography, ultrasonics, liquid penetrant, magnetic particle, eddy current*. ASM International, Materials Park, OH; 1995.

[76] J. Hoła, J. Bień, Ł. Sadowski, K. Schabowicz, Non-destructive and semi-destructive diagnostics of concrete structures in assessment of their durability, *Bulletin of the Polish Academy of Sciences Technical Sciences* 63, 87–96 (2015); doi: 10.1515/bpasts-2015-0010.

[77] R. Halmshaw, *Non-destructive testing*. Edward Arnold, London; 1991.

[78] J. F. Hinsley, *Non-destructive Testing*. London; 1959.

[79] U. Pant, J. K. Shrestha, Framework for assessing bridge quality index based on the correlation of non-destructive test results, *Heliyon* 10, e26392 (2024); doi: 10.1016/j.heliyon.2024.e26392.

[80] J. Shi, J. Xia, R. Wu, K. Chen, J. Wang, Y. Hoo, Non-destructive testing method of fiber content in steel fiber reinforced concrete based on magnetization loss, *Journal of Magnetism and Magnetic Materials* 586, 171205 (2023); doi: 10.1016/j.jmmm.2023.171205.

[81] S. Karlsson, M. Kozłowski, L. Grund, S. Andersson, K. Haller, K. Persson, Non-destructive strength testing of microindented float glass by a nonlinear acoustic method, *Construction and Building Materials* 391, 131748 (2023); doi: 10.1016/j.conbuildmat.2023.131748.

[82] A. M. M. M. Perez, L. A. S. Lopes, R. F. Caron, B. B. Oliveira, M. E. Poletti, Performance evaluation of six digital mammography systems, *Radiation Physics and Chemistry*, 111635 (2024); doi: 10.1016/j.radphyschem.2024.111635.

[83] M. Neslušan, P. Minárik, R. Čep, J. Ondruš, M. Pitoňák, K. Zgútová, Measurement of bearing capacity of steel road barrier flange via Barkhausen noise emission, *Engineering Failure Analysis* 156, 107804 (2024); doi: 10.1016/j.engfailanal.2023.107804.

[84] K. Omae, T. Yamazaki, C. Oka, J. Sakurai, S. Hata, Stress measurement based on magnetic Barkhausen noise for thin films, *Microelectronic Engineering* 279, 112057 (2023); doi: 10.1016/j.mee.2023.112057.

[85] C. Chiablam, B. Poopat, M. Noipitak, S. Heyrman, Eddy current analysis for predicting deterioration stages in alumina former radiant coils, *Engineering Failure Analysis* 158, 107943 (2024); doi: 10.1016/j.engfailanal.2023.107943.

[86] J. Lee, H. Sohn, H. J. Lim, Yield strength evaluation of 3D-printed Ti–6Al–4V components based on non-contact eddy-current measurement, *NDT & E International* 144, 103082 (2024); doi: 10.1016/j.ndteint.2024.103082.

[87] T. Le Manh, J. A. Pérez Benitez, J. H. Espina Hernández, J. M. Hallen López, *Barkhausen Noise for Non-Destructive Testing and Materials Characterization in Low Carbon Steels*. Elsevier; 2020.

[88] R. Jedamski, J. Heinzel, M. Rößler, J. Epp, J. Eckebrecht, J. Gentzen, M. Putz, B. Karpuschewski, Potential of magnetic Barkhausen noise analysis for in-process monitoring of surface layer properties of steel components in grinding, *tm - Technisches Messen* 87, 787–798 (2020); doi: 10.1515/teme-2020-0048.

[89] J. A. Pérez Benitez, T. Le Manh, M. Alberteris, Barkhausen noise for material characterization. In: *Barkhausen Noise for Non-Destructive Testing and Materials Characterization in Low Carbon Steels*, 115–146. Elsevier; 2020.

[90] D. M. Stewart, K. J. Stevens, A. B. Kaiser, Magnetic Barkhausen noise analysis of stress in steel, *Current Applied Physics* 4, 308–311 (2004); doi: 10.1016/j.cap.2003.11.035.

[91] C.-G. Stefanita, D. Atherton, L. Clapham, Plastic versus elastic deformation effects on magnetic Barkhausen noise in steel, *Acta Materialia* 48, 3545–3551 (2000); doi: 10.1016/S1359-6454(00)00134-8.

[92] J. Gauthier, T. W. Krause, D. L. Atherton, Measurement of residual stress in steel using the magnetic Barkhausen noise technique, *NDT & E International* 31, 23–31 (1998); doi: 10.1016/S0963-8695(97)00023-6.

[93] Stresstech Oy, Barkhausen Noise Signal Analyzers, https://www.stresstech.com/products/barkhausen-noise-equipment/barkhausen-noise-signal-analyzers/. Accessed February 22, 2024.

[94] Fraunhofer Institute for Nondestructive Testing IZFP, Material characterization with 3MA II, https://www.vision.fraunhofer.de/de/technologien-anwendungen/technologien/zerstoerungsfreie-pruefung/ferromagnetische-bauteile.html. Accessed February 22, 2024.

[95] QASS GmbH, Hardness Testing in A Non-Destructive Manner - QASS μmagnetic, https://business.qass.net/en/zerstorungsfreie-hartemessung. Accessed February 22, 2024.

[96] S. Ghanei, M. Kashefi, M. Mazinani, Comparative study of eddy current and Barkhausen noise nondestructive testing methods in microstructural examination

of ferrite–martensite dual-phase steel, *Journal of Magnetism and Magnetic Materials* 356, 103–110 (2014); doi: 10.1016/j.jmmm.2014.01.001.

[97] N. Bowler, *Eddy-Current Nondestructive Evaluation*. Springer New York, New York, NY; 2019.

[98] B. Hull, V. John, *Non-Destructive Testing*. Macmillan Education, New York, Ny, Springer, Houndmills, Basingstoke, Hampshire; 1988.

[99] J. Fraden, *Handbook of Modern Sensors*. Springer International Publishing, Cham; 2016.

[100] W. Homberg, B. Arian, V. Arne, T. Borgert, A. Brosius, P. Groche, C. Hartmann, L. Kersting, R. Laue, J. Martschin, T. Meurer, D. Spies, A. E. Tekkaya, A. Trächtler, W. Volk, F. Wendler, M. Wrobel, Softsensors: key component of property control in forming technology, *Production Engineering* (2023); doi: 10.1007/s11740-023-01227-1.

[101] S. Kay, H. Kay, M. Mowbray, A. Lane, C. Mendoza, P. Martin, D. Zhang, Integrating transfer learning within data-driven soft sensor design to accelerate product quality control, *Digital Chemical Engineering* 10, 100142 (2024); doi: 10.1016/j.dche.2024.100142.

[102] L. Ma, M. Wang, K. Peng, A two-phase soft sensor modeling framework for quality prediction in industrial processes with missing data, *Journal of Process Control* 129, 103061 (2023); doi: 10.1016/j.jprocont.2023.103061.

[103] A. J. Frafjord, J.-P. Radicke, A. Keprate, T. M. Komulainen, Data-driven approaches for deriving a soft sensor in a district heating network, *Energy* 292, 130426 (2024); doi: 10.1016/j.energy.2024.130426.

[104] J. Cao, A. Xue, Y. Yang, W. Cao, X. Hu, G. Cao, J. Gu, Le Zhang, X. Geng, Deep learning based soft sensor for microbial wastewater treatment efficiency prediction, *Journal of Water Process Engineering* 56, 104259 (2023); doi: 10.1016/j.jwpe.2023.104259.

[105] D. Kloeser, J. Martschin, T. Meurer, E. Tekkaya, Reduced order modelling for spatial-temporal temperature and property estimation in a multi-stage hot sheet metal forming process, *Advances in Industrial and Manufacturing Engineering* 3, 100055 (2021); doi: 10.1016/j.aime.2021.100055.

[106] F. Mühl, M. Knoll, M. Khabou, S. Dietrich, P. Groche, V. Schulze, Soft sensor approach based on magnetic Barkhausen noise by means of the forming process punch-hole-rolling, *Advances in Industrial and Manufacturing Engineering* 2, 100039 (2021); doi: 10.1016/j.aime.2021.100039.

[107] J. Wu, B. Liang, J. Yang, Trajectory prediction of three-dimensional forming tube based on Kalman filter, *The International Journal of Advanced Manufacturing Technology* 121, 5235–5254 (2022); doi: 10.1007/s00170-022-09521-5.

[108] J. Bechtloff, *Regelungstechnik*. Vogel Buchverlag, Würzburg; 2012.

[109] C. Bohn, H. Unbehauen, *Identifikation dynamischer Systeme: Methoden zur experimentellen Modellbildung aus Messdaten*. Springer Vieweg, Wiesbaden; 2016.

[110] K. Ogata, *Modern control engineering*. Pearson, Boston, Mass.; 2010.

[111] G. F. Franklin, J. D. Powell, A. Emami-Naeini, *Feedback control of dynamic systems*. Pearson Prentice Hall, Upper Saddle River, NJ; 2006.

[112] M. Kuhn, K. Johnson, *Applied Predictive Modeling*. Springer New York, New York, NY; 2013.

[113] M. Braun, *Differential Equations and Their Applications*. Springer New York, New York, NY; 1993.

[114] L. Perko, *Differential equations and dynamical systems*. Springer, New York, Berlin, Heidelberg; 2001.

[115] A. Braun, *Dynamische Systeme*. Springer Fachmedien Wiesbaden, Wiesbaden; 2019.

[116] Deutsches Institut für Normung e.V., Geschweißte Stahlrohre für Druckbeanspruchungen - Technische Lieferbedingungen: Teil 1: Elektrisch geschweißte und unterpulvergeschweißte Rohre aus unlegierten Stählen mit festgelegten Eigenschaften bei Raumtemperatur 23.040.10; 77.140.75 (August 2019).

[117] Deutsches Institut für Normung e.V., Kaltgeformte geschweißte Hohlprofile für den Stahlbau: Teil 1: Allgemeines (January 2016).

[118] A. Awasthi, K. K. Saxena, V. Arun, Sustainable and smart metal forming manufacturing process, *Materials Today: Proceedings* 44, 2069–2079 (2021); doi: 10.1016/j.matpr.2020.12.177.

[119] S. Biehl, S. Staufenbiel, F. Hauschild, A. Albert, Novel measurement and monitoring system for forming processes based on piezoresistive thin film systems, *Microsystem Technologies* 16, 879–883 (2010); doi: 10.1007/s00542-010-1058-0.

[120] T. Jayakumar, C. K. Mukhopadhyay, S. Venugopal, S. L. Mannan, B. Raj, A review of the application of acoustic emission techniques for monitoring forming and grinding processes, *Journal of Materials Processing Technology* 159, 48–61 (2005); doi: 10.1016/j.jmatprotec.2004.01.034.

[121] A. Kumar, A. Das, A nonlinear process monitoring strategy for a Metal Forming process, *Materials Today: Proceedings* 59, 368–372 (2022); doi: 10.1016/j.matpr.2021.11.327.

[122] B. Ralph, S. Martin, *Digitalization and digital transformation in metal forming: key technologies, challenges and current developments of industry 4.0 applications*; 2020.

[123] M. Bambach, T. Meurer, W. Homberg, S. Duncan, Editorial to special issue “Property-controlled forming processes”, *Advances in Industrial and Manufacturing Engineering* 4, 100068 (2022); doi: 10.1016/j.aime.2022.100068.

[124] X. Gao, T. Zhang, J. Zhou, S. M. Graham, M. Hayden, C. Roe, On stress-state dependent plasticity modeling: Significance of the hydrostatic stress, the third invariant of stress deviator and the non-associated flow rule, *International Journal of Plasticity* 27, 217–231 (2011); doi: 10.1016/j.ijplas.2010.05.004.

[125] D. Reimann, K. Nidadavolu, H. ul Hassan, N. Vajragupta, T. Glasmachers, P. Junker, A. Hartmaier, Modeling Macroscopic Material Behavior With Machine Learning Algorithms Trained by Micromechanical Simulations, *Frontiers in Materials* 6 (2019); doi: 10.3389/fmats.2019.00181.

[126] D. Salehiyan, J. Samei, B. S. Amirkhiz, L. G. Hector, D. S. Wilkinson, Microstructural Evolution During Deformation of a QP980 Steel, *Metallurgical and Materials Transactions A* 51, 4524–4539 (2020); doi: 10.1007/s11661-020-05882-2.

[127] B. J. Yang, A. Hattiangadi, W. Z. Li, G. F. Zhou, T. E. McGreevy, Simulation of steel microstructure evolution during induction heating, *Materials Science and Engineering: A* 527, 2978–2984 (2010); doi: 10.1016/j.msea.2010.01.038.

[128] N. Vajragupta, S. Maassen, T. Clausmeyer, D. Brands, J. Schröder, A. Hartmaier, Micromechanical Modeling of DP600 steel: From Microstructure to The Sheet Metal Forming Process, *Procedia Manufacturing* 47, 1540–1547 (2020); doi: 10.1016/j.promfg.2020.04.347.

[129] Deutsches Institut für Normung e.V., Metallische Werkstoffe – Härteprüfung nach Vickers: Teil 1: Prüfverfahren (2024-01-00).

[130] Deutsches Institut für Normung e.V., Metallische Werkstoffe - Zugversuch: Teil 1: Prüfverfahren bei Raumtemperatur.

[131] thyssenkrupp Schulte GmbH, Werkstoffdatenblatt: Unlegierter Stahl für Druckbeanspruchung, https://de.materials4me.com/media/pdf/45/79/0c/Werkstoffdatenblatt_P235TR1_1-0254_01-2020.pdf.

[132] Deutsches Institut für Normung e.V., Metallische Werkstoffe - Härteprüfung nach dem UCI-Verfahren: Teil 1: Prüfverfahren.

[133] D. Damjanović, D. Kozak, S. Marsoner, N. Gubeljak, Residual stress state in pipe cut ring specimens for fracture toughness testing, *Materials Testing* 59, 530–535 (2017); doi: 10.3139/120.111038.

[134] E28 Committee, Practice for Estimating the Approximate Residual Circumferential Stress in Straight Thin-walled Tubing.

[135] L. Z. Chen, S. K. Nguang, X. M. Li, X. D. Chen, Soft sensors for on-line biomass measurements, *Bioprocess and biosystems engineering* 26, 191–195 (2004); doi: 10.1007/s00449-004-0350-8.

[136] D. Wang, J. Liu, R. Srinivasan, Data-Driven Soft Sensor Approach for Quality Prediction in a Refining Process, *IEEE Transactions on Industrial Informatics* 6, 11–17 (2010); doi: 10.1109/TII.2009.2025124.

[137] S. Han, T. Kim, D. Kim, Y.-L. Park, S. Jo, Use of Deep Learning for Characterization of Microfluidic Soft Sensors, *IEEE Robotics and Automation Letters* 3, 873–880 (2018); doi: 10.1109/LRA.2018.2792684.

[138] W. Volk, P. Groche, A. Brosius, A. Ghiotti, B. L. Kinsey, M. Liewald, L. Madej, J. Min, J. Yanagimoto, Models and modelling for process limits in metal forming, *CIRP Annals* 68, 775–798 (2019); doi: 10.1016/j.cirp.2019.05.007.

[139] D. Maier, S. Stebner, A. Ismail, M. Dölz, B. Lohmann, S. Münstermann, W. Volk, The influence of freeform bending process parameters on residual stresses for steel tubes, *Advances in Industrial and Manufacturing Engineering* 2, 100047 (2021); doi: 10.1016/j.aime.2021.100047.

[140] H. Altenbach, *Technische Mechanik Festigkeitslehre: 104 Aufgaben, 133 Beispiele und zahlreiche Klausuraufgaben mit Lösungen*. Springer Vieweg, Wiesbaden; 2020.

[141] J. Mathar, Ermittlung von Eigenspannungen durch Messung von Bohrloch-Verformungen, *Archiv für das Eisenhüttenwesen* 6, 277–281 (1933); doi: 10.1002/srin.193300416.

[142] E28 Committee, Test Method for Determining Residual Stresses by the Hole-Drilling Strain-Gage Method.

[143] Deutsches Institut für Normung e.V., Zerstörungsfreie Prüfung: Röntgendiffraktometrisches Prüfverfahren zur Ermittlung der Eigenspannungen.

[144] Deutsches Institut für Normung e.V., Metallische Werkstoffe - Umwertung von Härtewerten.

[145] J. Frankel, A. Abbate, W. Scholz, The effect of residual stresses on hardness measurements, *Experimental Mechanics* 33, 164–168 (1993); doi: 10.1007/BF02322494.

[146] J. Meiss, Dynamical systems, *Scholarpedia* 2, 1629 (2007); doi: 10.4249/scholarpedia.1629.

[147] S. A. Billings, *Nonlinear system identification: NARMAX methods in the time, frequency, and spatio-temporal domains*. John Wiley & Sons, Chichester, West Sussex; 2013.

[148] F. Govaers, *Introduction and Implementations of the Kalman Filter*. IntechOpen, Erscheinungsort nicht ermittelbar; 2019.

[149] Deutsches Institut für Normung e.V., Metallische Werkstoffe - Härteprüfung nach Vickers: Teil 1: Prüfverfahren.

[150] J. M. Bland, D. G. Altman, Comparing methods of measurement: why plotting difference against standard method is misleading, *Lancet (London, England)* 346, 1085–1087 (1995); doi: 10.1016/S0140-6736(95)91748-9.

[151] J. Martin Bland, D. Altman, Statistical methods for assessing agreement between two methods of clinical measurement, *The Lancet* 327, 307–310 (1986); doi: 10.1016/S0140-6736(86)90837-8.

[152] L. Sachs, J. Hedderich, *Angewandte Statistik: Methodensammlung mit R ; mit 180 Tabellen*. Springer, Berlin, Heidelberg; 2006.

[153] J. D. Schnapp, V. Herold, J. Reuschel, Rauheitsanforderungen für die mobile Härteprüfung metallischer Werkstoffe, *Materials Testing* 60, 73–80 (2018); doi: 10.3139/120.111091.

[154] Deutsches Institut für Normung e.V., Grundlagen der Meßtechnik: Teil 1: Grundbegriffe.

[155] W. F. Hosford, *Mechanical behavior of materials*. Cambridge University Press, New York; 2005.

[156] V. Hauk, *Structural and Residual Stress Analysis by Nondestructive Methods*. Elsevier; 1997.

[157] A. Sipeky, A. Ivanyi, Magnetic hysteresis under applied stress, *Physica B: Condensed Matter* 372, 177–180 (2006); doi: 10.1016/j.physb.2005.10.042.

[158] J. A. Pérez-Benítez, J. H. Espina-Hernández, P. Martínez-Ortiz, A. F. Chávez-González, J. M. de La Rosa, Analysis of the influence of some magnetizing parameters on magnetic Barkhausen noise using a microscopic model, *Journal of Magnetism and Magnetic Materials* 347, 51–60 (2013); doi: 10.1016/j.jmmm.2013.07.034.

[159] M. Suliga, K. Chwastek, P. Pawlik, Hysteresis loop as the indicator of residual stress in drawn wires, *Nondestructive Testing and Evaluation* 29, 123–132 (2014); doi: 10.1080/10589759.2013.858717.

[160] X. Kleber, A. Vincent, On the role of residual internal stresses and dislocations on Barkhausen noise in plastically deformed steel, *NDT & E International* 37, 439–445 (2004); doi: 10.1016/j.ndteint.2003.11.008.

[161] R. Ranjan, D. C. Jiles, O. Buck, R. B. Thompson, Grain size measurement using magnetic and acoustic Barkhausen noise, *Journal of Applied Physics* 61, 3199–3201 (1987); doi: 10.1063/1.338900.

[162] S. Yamaura, Y. Furuya, T. Watanabe, The effect of grain boundary microstructure on Barkhausen noise in ferromagnetic materials, *Acta Materialia* 49, 3019–3027 (2001); doi: 10.1016/S1359-6454(01)00189-6.

[163] F. Pedregosa, G. Varoquaux, A. Gramfort, V. Michel, B. Thirion, O. Grisel, M. Blondel, P. Prettenhofer, R. Weiss, V. Dubourg, J. Vanderplas, A. Passos, D. Cournapeau, M. Brucher, M. Perrot, É. Duchesnay, Scikit-learn: Machine Learning in Python, *Journal of Machine Learning Research*, 2825–2830 (2011).